HIGH ANISOTROPY *hcp* CoPt MEDIA FOR PERPENDICULAR MAGNETIC RECORDING

PANDEY KOASHAL KISHOR MANI

(M. Tech. Indian Institute of Technology Kanpur, India)

A THESIS SUBMITTED

FOR THE DEGREE OF DOCTOR OF PHILOSPHY

DEPARTMENT OF MATERIALS SCIENCE

NATIONAL UNIVERSITY OF SINGAPORE

2008

Acknowledgements

First of all, I would like to express my sincere gratitude to my thesis advisors and mentor Prof. Gan-Moog Chow and Dr. Jingsheng Chen for their guidance, inspiration and encouragement throughout the course of my Ph. D. program. I learnt a lot in every domain of my academic life from their comments during the group discussions. However, the thing to which I am extremely grateful is a single sentence said by Prof. Gan-Moog Chow "Koashal- you are my Ph. D. student, not the technician, you must think about the problem critically yourself".

Over and above I would like to thank the academic and research staff of the department of Materials Science and Engineering for their valuable discussions and support. The experimental facilities provided by Data Storage Institute (DSI) Singapore and Advanced Photon Source at Argonne National Laboratory (USA) to complete this research works are greatly acknowledged.

I would like to express my heartfelt thanks to Dr. C. J. Sun (currently at Oak-Ridge Laboratory-USA), Y. Z. Zhou, B. C. Lim, C. Y. Tan, and J. B. Yi in the department of Materials Science and Engineering for fruitful discussions and providing friendly environment in Singapore. I am grateful to Mr. B. H. Liu (EM facility unit, Faculty of Science) and Dr. Liu Tao (Singapore Synchrotron Light Source) for their outstanding contribution in collecting the TEM images and EXAFS data analysis, respectively. I also thank J. F. Hu and Y. F. Ding for their help.

Last but not least, I would like to thank all my family members, especially my wife Shilpi, for their continuous love, inspiration and support. The acknowledgement will be incomplete without mentioning thanks to my daughter Ishita.

Table of Contents

Summary

The demand of increasing areal density in magnetic recording is based on scaling. Recording bits have to be shrunk to increase the areal density of magnetic recording media. In order to maintain the signal-to-noise ratio (*SNR*), which is proportional to the logarithm of grain numbers in each bit, the grain size has to be reduced, and must be able to overcome the superparamagnetic limit. Material with large magnetocrystalline anisotropy (K_u) is required for future ultra-high density magnetic recording media in order to delay the onset of superparamagnetic limit. Although, $L1_0$ CoPt and FePt have emerged as potential candidates for high density magnetic recording media due to their large K_u in the range of 5-7 x 10^7 erg/cc, many challenges such as grain size control and reduced deposition temperature remain for their practical applications. It is therefore still desirable to increase the K_u of currently used CoCrPt based recording media to further increase the areal density.

This thesis focused on increasing the K_u of CoCrPt based magnetic recording media. The presence of Cr in the CoCrPt media reduced the K_u. An alternative, such as CoPt media was therefore investigated to increase the K_u. A large K_u value to ~9 x 10^6 erg/cc was achieved in the $Co_{72}Pt_{28}$ film deposited at smooth Ta seedlayer surface. This K_u value allowed thermally stable grain size down to 4.5 nm diameter and to be able to support the areal density of 1 Tbits/in^2. Furthermore, to improve the *SNR* in the magnetic recording media, a layer engineering approach was adopted to control the microstructure of recording layer. Dual-layer Ru underlayer was effective in reducing the intergranular exchange interaction and grain size, and induced favorable environment for large *SNR*.

In order to study the origin of large K_u; the phase miscibility, growth induced structural anisotropy and strain at short-range order of CoPt thin films were

investigated using polarized extended x-ray absorption fine structure. A qualitative analysis of x-ray absorption near-edge spectroscopy indicated that *hcp* stacking was improved for $Co_{72}Pt_{28}$ film. No evidence of compositional heterogeneity between the in-plane and out-of-plane polarization geometries was detected for $Co_{72}Pt_{28}$ film. The number of Pt atoms around Co was approximately the same in the in-plane and out-of-plane polarization geometries, and equal to the Pt global composition. It revealed that Pt exhibited random miscibility in the Co lattice for $Co_{72}Pt_{28}$ film. However, a compositional heterogeneity was observed for $Co_{90}Pt_{10}$ and $Co_{57}Pt_{43}$ films, wherein Co atom was surrounded by more Pt in the film plane rather than the out-of-plane direction. The average interatomic distance in the in-plane polarization geometry was larger than that of the out-of-plane for $Co_{90}Pt_{10}$ and $Co_{57}Pt_{43}$ films. These results supported an in-plane tensile strain. However, the average interatomic distance in the in-plane and out-of-plane polarization geometries was approximately the same for $Co_{72}Pt_{28}$ film, indicating absence of tensile strain in the film plane. The absence of in-plane tensile strain in the $Co_{72}Pt_{28}$ favored the growth of (0002) texture, which could be responsible for increased K_u value in $Co_{72}Pt_{28}$ film.

List of Tables

List of Figures

List of abbreviation

1. AC: Alternating current
2. AFM: Atomic force microscopy
3. AGFM: Alternating gradient force magnetometer
4. APS: Advanced Photon Source
5. DC: Direct current
6. DCD: DC demagnetization
7. DSI: Data Storage Institute
8. DWM: Domain wall motion
9. ECC: Exchange coupled composite
10. EUV: Extreme ultraviolet
11. EXAFS: Extended x-ray absorption fine structure
12. *fcc*: Face centered cubic
13. FT: Fourier transform
14. FWHM: Full-width at half-maximum
15. *hcp*: Hexagonal close packed
16. HAMR: Heat assisted magnetic recording
17. HDD: Hard disk drive
18. HRTEM: High resolution transmission electron microscopy
19. IML: Intermediate layer
20. JCPDS: Joint Committee on Powdered Diffraction Standard
21. LRM: Longitudinal recording media
22. LRO: Long-range order
23. MFM: Magnetic force microscopy
24. PMR: Perpendicular magnetic recording

25. PNC-CAT: Pacific Northwest Consortium-Collaborative Access Team

26. RAMAC: Random access method of accounting and control

27. RBS: Rutherford backscattering spectroscopy

28. *SNR*: Signal-to-noise ratio

29. SOMA: Self-organized magnetic array

30. SRO: Short-range order

31. S-W: Stoner-Wohlfarth

32. TEM: Transmission electron microscopy

33. TSF: Thermal stability factor

34. VSM: Vibrating sample magnetometer

35. XANES: X-ray absorption near-edge spectroscopy

36. XRD: X-ray diffraction

List of Symbols

1. α: Shearing parameter at coercivity
2. χ(k): EXAFS fine structure factor
3. $\delta_j(k)$: Phase shift
4. λ: Wavelength
5. $\lambda(k)$: Mean free path of photoelectron
6. $\mu(k)$: Total absorption coefficient
7. $\mu_0(k)$: Absorption coefficient of an isolated atom
8. σ: Grain size distribution
9. σ^2: Relative mean square deviation
10. τ: Relaxation time
11. θ: Angle between film normal (easy axis) and applied field direction
12. d_{hkl}: Interplanar spacing of *(hkl)* plane
13. D: Average grain size
14. f_0: Relaxation frequency
15. $F_j(k)$: Backscattering amplitude
16. h: Plank's constant
17. H_c: Coercivity
18. $H_{c\theta}$: Coercivity at angle θ
19. $H_{c\perp}$: Coercivity at θ = 0
20. H_{cr}: Remanent coercivity
21. $H_{cr\theta}$: Remanent coercivity at angle θ
22. $H_{cr\perp}$: Remanent coercivity at θ = 0
23. $H_{cr}(t)$: Remanent coercivity after applying field for time t

24. H_k: Anisotropy field

25. k_B: Boltzmann's constant

26. K_u: Magnetocrystalline anisotropy constant

27. K_1: First order magnetocrystalline anisotropy constant

28. K_2: Second order magnetocrystalline anisotropy constant

29. L: Torque

30. M_s: Saturation Magnetization

31. N: Number of grain per bit

32. $N_{//}$: Demagnetization factor along the easy axis

33. $N_{\perp}$: Demagnetization factor perpendicular to the easy axis

34. N_j^*: Number of neighboring atoms of j shell

35. q: Momentum transfer

36. R_j: Neighboring atoms distance of j shell

37. T: Absolute temperature

38. T_C: Curie temperature

List of Publications

1. **K. K. Mani Pandey,** J. S. Chen and G. M. Chow, Compositional dependence of magnetic properties of Co-Pt thin films, J. Appl. Phys, **100**, 054909 (2006).
2. **K. K. M. Pandey,** J. S. Chen, B. C. Lim and G. M. Chow, Effects of Ru underlayer on structural and magnetic properties of CoPt films, J. Appl. Phys. **104**, 073904 (2008).
3. **K. K. M. Pandey,** J. S. Chen, J. F. Hu and G. M. Chow, Microstructural evolution and magnetization reversal behavior of CoPt films, J. Phys. D: Appl. Phys. **42**, 015009 (2009).
4. **K. K. M. Pandey,** J. S. Chen, G. M. Chow, J. F. Hu and B. C. Lim, Interlayer coupling and switching field of exchange coupled media, J. Appl. Phys. (*in-press*).
5. **K. K. M. Pandey,** J. S. Chen, B. C. Lim and G. M. Chow, Seedlayer interface induced enhanced magnetocrystalline anisotropy in CoPt films (submitted).
6. **K. K. M. Pandey,** J. S. Chen, C. J. Sun, T. Liu and G. M. Chow, Phase miscibility and strain analysis in CoPt thin films: A polarization dependent EXAFS study (to be submitted).

Chapter 1
Introduction

The idea of magnetic recording was first conceived and described by Oberlin Smith in 1878; but it was 1898, twenty years later, the device based on such idea was demonstrated by Valdemar Poulsen.[1] Since 1898 this technology has continued to expand. The onset of major revolution in magnetic recording took place in 1956 when IBM built the world's first ever random access method of accounting and control (RAMAC) hard disk drive of total storage capacity of 5 megabytes at a recording areal density of 2 Kbit/in^2.[2] Today, it enters into almost every facet of our daily working and leisure activities. Throughout the entire history of magnetic recording, research efforts have always been concentrated on achieving the high areal density in magnetic recording media. It is the result of continuous efforts in the last 50 years that the areal density reaches to the height of 200 Gbit/in^2, almost 10^8 times of the recording areal density of its inception value.[3] In fact, in late 2006, Seagate technology demonstrated the areal density of 421 Gbit/in^2. As a result, today storing data in the hard disk drives is cheaper than storing the same information on paper. However, to further increase the areal density to 1 Tbit/in^2 and beyond, the recording bits have to be scaled downward. At the same time, to maintain the signal-to-noise ratio (*SNR*), which is proportional to the logarithm of number of grains in each bit (typically few tens),[4] the grain size has to be reduced, and yet overcome superparamagnetic limit. Superparamagnetism is the phenomenon that the thermal energy causes spontaneous reversal of the magnetization directions of magnetic particles from one easy direction to another easy direction, even in the absence of applied magnetic field. The spontaneous reversal of magnetization leads to

undesirable loss of recorded data. This indicates that two competing properties, the high thermal stability and large *SNR* are essential to further increase the areal density.

1.1 Requirements of magnetic recording media for high areal density

Increasing areal density is a requirement of current hard disk drive technology. The enhancement in the magnetic recording areal density is governed by the characteristics of magnetic recording media. A suitable magnetic recording media is necessary to keep the data thermally stable for a sufficiently long time. The magnetic recording media must also be able to provide large *SNR* to reliably read-back stored data. In the following sections the requirements of magnetic recording media for high thermal stability and large *SNR* are discussed.

1.1.1 Thermal stability

Analogous to the Brownian motion, the thermal energy causes fluctuation of the magnetization directions of magnetic grains, and the magnetization directions reverse statistically with time for a given temperature. A magnetic grain with uniaxial magnetocrystalline anisotropy constant (K_u) and volume V exhibits magnetic anisotropy energy barrier $\Delta E = K_u V$, which must be overcome to reverse its magnetization direction. If the volume of a magnetic grains becomes too small, the thermal energy becomes comparable to the magnetic energy, causing unwanted magnetization reversal of the grains from one easy direction to the other easy direction in the absence of applied magnetic field.[5] To ensure that the magnetization remains along its easy axis, the magnetic energy must be high enough to withstand the effects of thermal agitation. The competition between the thermal energy and

anisotropy energy reflects the magnetization reversal probability and follows the Neel-Arhenius law given by

$$1/\tau = f_0 \exp(-K_u V / k_B T) \tag{1.1}$$

where τ is the relaxation time, $f_0 = 10^9 \text{ sec}^{-1}$ the relaxation frequency, k_B the Boltzmann's constant and T the absolute temperature. Based on the above equation, to store the data thermally stable for the period of 10 years, the thermal stability factor (TSF) is defined by K_uV/k_BT and its value ≥ 60.[6,7]

1.1.2 Signal-to-noise ratio

In high areal density magnetic recording media, writing and reading of the data are equally important. To achieve high areal density, it is necessary to have a large *SNR* to read the data reliably. In conventional recording media, the *SNR* is determined by the number of grains (N) per bit, since $SNR \sim 10LogN$. As a result, small grain size always favors the increase of *SNR*. In addition, the *SNR* not only depends on the average grain size (D) but also on the width of the grain size distribution (σ) as described by[8]

$$SNR \approx \frac{1}{\left[\langle D \rangle^3 \left\{1 + \left(\frac{\sigma}{D}\right)^2\right\}\right]} \tag{1.2}$$

It indicates that small grain size and narrow grain size distribution are ideal condition for large *SNR*. Furthermore, large intergranular exchange interaction increases the effective switching volume of magnetic cluster, which leads to increase the zigzag region between two recording bits, consequently increasing the transition

jitter noise. Thus, along with small grain size and narrow grain size distribution, small intergranular exchange interaction is also necessary to achieve a large *SNR*.

1.2 Magnetic recording media

1.2.1 Longitudinal magnetic recording media

Before 2006, recording industries were using longitudinal magnetic recording (LMR) to store information in the hard disk drives. This is a transition period as recording technology is changing from the longitudinal magnetic recording to the perpendicular magnetic recording. In the LMR, the magnetization directions of recording bits lie in the film plane. Typically, uniaxial anisotropic hexagonal close packed (*hcp*) Co-based alloys having magnetization directions in the film plane are used in LMR. The underlayer materials such as Cr and binary alloys of Cr are used to control the c-axis of Co-based alloys in the film plane.[9-11] For example, the $(11\bar{2}0)$ textured Co-based alloy magnetic layer exhibits c-axis in the film plane and grows very well on the Cr (200) texture underlayer. Similarly, the Co $(10\bar{1}1)$ grows hetero-epitaxially on Cr (110) and establishes the easy axis of Co-based alloy at 29° from the film surface.[12]

Conventionally, the demand of high areal density in a LMR is achieved by scaling, since the areal density and grain size have inverse relationship with each other. Further increase in areal density requires further reduction in the grain size of magnetic recording media to keep the number of grain per bit constant to maintain the desirable *SNR* level.[13] However, the reduction in the grain size inevitably causes a lower energy barrier that eventually leads to the thermal instability. An obvious solution to this problem is using a thicker media or selecting the material with high

K_u. In the LMR, the grain volume cannot be increased by increasing the thickness of media, because it degrades the recording resolution, since the recording resolution is proportional to the $M_r t$,[14] where M_r is the remanent magnetization and t the film thickness. The use of high K_u material is an alternative approach to compensate the reduction in the grain size yet to retain sufficient thermal stability. However, in the LMR, the writing of a bit is governed by the stray-field between the poles of writing head, which is insufficient to write the magnetic recording media of high K_u materials, because high K_u materials exhibit large coercivity (H_c) that is proportional to K_u, since $H_c \approx 2K_u / M_s$ where M_s is the saturation magnetization of magnetic recording media. Therefore, the physical limitation imposed by superparamagnetism does not allow LMR to further increase the areal density using high K_u materials.

1.2.2 Perpendicular magnetic recording media

Perpendicular magnetic recording (PMR) was proposed by Iwasaki in 1975 as a substitute to LMR to increase the areal density.[15] It has received increasing attention in the past 5-7 years because of the thermal stability limitation of LMR. In the PMR, the easy axis of magnetization direction of grains in magnetic recording media points along the film's normal direction unlike the LMR in which magnetization direction lies in the film plane direction. The main advantage of PMR is the inclusion of a soft underlayer, which assists in writing the information. The PMR enjoys following advantages over the LMR.

- In PMR with a soft underlayer, the single pole head is used for read/write purpose, which enables writing the magnetic recording media with coercivity as large as twice to the ring head used in LMR.[16] Large writing field of head

facilitates the use of the high K_u materials (by factor of 2 in comparison to LMR) in PMR. This in turn allows the magnetic recording media of smaller grain volume, and supports the increase of the areal density. An overview of high K_u materials for PMR media are given in Table 1.1.[17]

- The grains in PMR have strong uniaxial orientation (longitudinal media tend to have an orientation that is random in-plane), which leads to narrow switching field distribution and sharper written transition. The sharp transition increases the linear density and *SNR*. [16]

Because of promising potential of PMR, much related work has been pursued.[18-25] A hard disk drive based on PMR has been successfully achieved first by the Seagate Technology in the year 2006. The magnetic recording media in such drives are based on a CoCrPt alloy with some oxide materials that can increase the areal density to 600 Gbit/in^2.[26]

1.2.3 Challenges for current perpendicular magnetic recording media

Though, PMR enjoys various advantages over LMR, it is still unable to achieve recording density to 1 Tbit/in^2 and beyond, using current CoCrPt media due to competition between the *SNR* and thermal stability.[17] Co/Pt and Co/Pd multilayers of several bilayers have attracted much attention for PMR application because of their large K_u value.[27-30] They are considered as alternatives to further increase the areal density. However, Co/Pt and Co/Pd multilayers exhibit strong intraplanar magnetic interaction of magnetic grains, and reduce the *SNR*, which ultimately limits their industrial application. The magnetic materials such as $L1_0$ CoPt and FePt with high K_u (~5-7 x 10^7 erg/cc) cannot be used due to two reasons.

Table 1.1: Magnetic properties of various media candidates of high magnetic crystal anisotropy constant, K_u, (K_u refers to first order magnetic crystal anisotropy constant). (Courtesy of D. Weller and R. Skomski[17])

Alloy system	Material	K_u (10^7 erg/cc)	M_s (emu/cc)	H_K (kOe)	T_C (K)	D_p (nm)
Co-alloy	$CoCr_{20}Pt_{15}$	0.25	330	15.2		15.5
	Co_3Pt	2	1100	36.4	1200	6.4
	$(CoCr)_3Pt$	0.39	410	19		12.4
	$CoPt_3$	0.5	300	33.3	600	9.1
Co/Pt(Pd) multilayer	Co/Pt	1	360	55.6	500	6.1
	Co/Pd	0.6	360	33.3	500	8.1
$L1_0$ phase	FePd	1.7	1100	32.7	760	7.3
	FePt	7	1140	122.8	750	2.4
	CoPt	4.9	800	122.5	840	2.8
	MnAl	1.7	560	60.7	650	4.9
Rare-earth alloy	$Fe_{14}Nd_2B$	4.6	1270	72.4	585	3.4
	Sm_5Co	20	910	439.6	1000	1.3

where, M_s is the saturation magnetization of the materials, H_K the anisotropy field, T_C the Curie temperature, D_p the grain diameter estimated using maximum demagnetization $4\pi M_s$ and cylindrical size of constant height 10 nm.

Firstly, to achieve the desired $L1_0$ phase, undesirably high deposition temperature or post deposition annealing at high temperature is required.[31-33] Secondly, the writing field limitation of head. The writing field of the existing head is limited by the highest saturation magnetization of head materials. Among the all known magnetic materials, the $Fe_{65}Co_{35}$ exhibits maximum saturation magnetization of 24 kOe,[34] which is the maximum limit of writing head. However, room temperature coercivity of 70 kOe has

been reported in the $L1_0$ FePt thin film deposited at 780 ºC, which is too large to be written, using exiting single pole head.[35] Hence, an alternative beyond conventional PMR is currently needed to further increase the areal density, overcoming the challenges of *SNR,* thermal stability and writing field.

1.3 Magnetic recording media of next generation

It has been discussed in section 1.2.2 that current CoCrPt-oxide based PMR is unable to increase the areal density beyond 600 Gbit/in^2 due to the superparamagnetic limit of media, and writing field limitation of head. To further increase the areal density, several new types of recording media such as heat assisted magnetic recording media,[36,37] patterned media[38-42] and exchange coupled composite media,[43] have been proposed. In the following sub-sections a brief introduction about such types of media is discussed.

1.3.1 Heat assisted magnetic recording media

The writing field limitation of writing head is one of the major concerns in the attempt to achieve the areal density to 1 Tbit/in^2 and beyond. To overcome this problem, a new concept of heat assisted magnetic recording (HAMR) was proposed. The HAMR technology is based on the inverse dependence of a magnetic anisotropy and temperature.[44] In HAMR, the magnetic recording media is temporarily and locally heated during the writing process, close to the Curie temperature, which reduces the magnetic anisotropy and allows writing using the currently available writing field. After writing, the magnetic recording media is then quickly cooled to its ambient stage to store the data. This technology directly allows using the known

magnetic materials with large K_u as a magnetic recording media. This provides an opportunity to further reduce the grain size and increase the areal density. Based on the theoretical calculation it has been projected that the $L1_0$-FePt is capable of increasing the areal density up to 2 Tbit/in^2.[45] Despite the advantage of reducing the writing field requirement, the HAMR technology is facing following major challenges.

- It requires the writing head integrated with a laser to locally heat the material.
- It requires very fast cooling system so that the heating process does not render adjacent grains thermally unstable.
- During the writing process the magnetic recording media is heated close to the Curie temperature. The Curie temperatures of FePt and CoPt are 477 °C and 567 °C, respectively. However, there is no overcoat material that can withstand such a high temperature. Thus, a new type of polymeric material is needed as a protective overcoat.

Furthermore, HAMR is very suitable for using high anisotropy material such as $L1_0$ CoPt and FePt. However, the minimum deposition temperature needed for the transformation of disordered CoPt and FePt to desired $L1_0$ ordered phase of high K_u is above 534 °C[31] and 350 ºC[32,33] respectively. Hence it is difficult to prevent grain growth at such a high temperature.

1.3.2 Patterned media

Patterned media is a new approach to delay the onset of the superparamagnetism, wherein each single-domain magnetic grain represents one bit rather than a combination of few tens of grains like conventional recording media.[34,41]

In conventional recording media the *SNR* is directly proportional to the logarithm of number of grains in each bit. However, in patterned media, the *SNR* argument is different from the conventional media. In this case, the number of grains per bit is reduced to one, and there is no statistical averaging over many entities to reduce the noise. The bit boundary is also sharply defined and overcomes the transition jitter noise. Lambeth et al.[42] have projected that the uniaxial Co-based alloy with 8 nm diameter particle centered on 10 nm array spacing is able to achieve the areal density over 6 Tbit/in^2. This periodic array can be constructed by lithography. Sbiaa et al.[26] have evaluated that 12 x12 nm pattern size separated by 12 nm spacing is sufficient to achieve the areal density of 1 Tbit/in^2. Though pattern media is able to achieve the areal density beyond 1 Tbit/in^2, it is based on the feasibility of lithography for successful patterning of size down to ~10-12 nm at low cost and in a reasonably short time. Different lithography techniques such as a deep UV lithography, extreme UV lithography, x-ray lithography, electron beam lithography, nano-imprint lithography and lithography assisted self assembly have been attempted to pattern the size down to 10 nm. These techniques are suffering from following challenges.

- Deep UV lithography, today's most common lithography technique, is useful to make pattern slightly below 100 nm, which is far from the requirement of 10-12 nm features to achieve the areal density up to 1 Tbit/in^2.
- Extreme UV (EUV) lithography with 13.5 nm wavelength has been considered as a next generation lithography for patterning of 10-12 nm nanostructure, since periodic nanostructure down to 20 nm has already been reported using this technique. But this technique is useful for line, square and rectangular pattern. It is not suitable for recording media application where circular disk is used for storing information.

- Besides EUV, x-ray lithography using synchrotron radiation has also been considered as another alternative of conventional lithography. But it is very expensive and has limited accessibility.
- Electron beam lithography is able to pattern the system down to 10 nm but it is also expensive and time consuming.
- Nano-imprint lithography is investigated to successfully fabricate the pattern size down to 25 nm.[39] Further study indicates that the imprint lithography can potentially achieve 10 nm resolution over an area much greater that 1 square inch. However, the success of nano-imprint lithography depends on fabrication of defects free nano-scale pattern that is very difficult to achieve. Further research is on going to overcome this problem.
- An alternative promising route for patterning nano-scale device is using a template made from self-organized particles. The self-organized patterns can serve as etching mask for patterning a magnetic structure or it can be used as a template for deposition of magnetic structure. For example, anodized alumina can produce two dimensional array of hexagonal array of cylindrical pore, and diameter of pores may be changed from 4 nm to a few hundred nm depending on anodizing conditions. Similarly, self assembled cylindrical copolymer made of two different miscible monomers, and selective etching of one of them may work as a nano-scale etching mask. In addition, the self organization of the array of magnetic nanoparticle of FePt has been investigated for recording media application. The self-organized magnetic array (SOMA) of monodispersed FePt nanoparticle with very controlled size between 3-10 nm with a standard deviation of less than 5% was first reported in 2000 by reduction of platinum acetylacetonate and decomposition of iron

pentacorbonyle in the presence of oleic acid and oleyl amine.[46] This media can fulfill the requirements of high areal density as well as the high *SNR* due to its small size and a narrow size distribution. It is anticipated that recording densities up to 40-50 Tbit/in^2 can be achieved using SOMA. In spite of various advantage of SOMA, it is suffering from following drawbacks.

- To prepare uniformly monodispersed magnetic nanoparticle in long range order on disk with high packing density is very challenging.
- The arrangements of the particles are in the X-Y direction not in the circumferential geometry. In hard disk, it would be preferred to arrange the dots in the circular fashion since magnetic head moves on a spinning circular disk.
- While in self-assembly, the size distribution of less than 5% has been achieved in the as-deposited SOMA structures, annealing above 600 ºC is still required to transform the monodispersed FePt nanoparticle into a magnetically hard $L1_0$-ordered phase. The array order and size distribution may be destroyed during annealing resulting in the loss of SOMA structure.
- All FePt SOMA structures exhibit almost random easy axis orientation, which is not suitable for future high density media as it creates extra media noise and reduces the signal strength.

Hence, it may take several years to remove all the constraints in pattering before it is ready for industrial application. It has been predicted that even pattern media may be delayed or even not be realized if efforts made in HAMR becomes successful.[26]

1.3.3 Exchange coupled composite media

It has already been discussed in the above sections that reducing writing field is one of the key challenge before the realization of high K_u materials for industrial application. In recording media, coherent switching of magnetic grains is preferred to retain high thermal stability and to maintain high *SNR*. According to the Stoner-Wohlfarth (S-W) model of the coherent rotation, the lowest switching field is required when the applied field is inclined at 45^o with respect to the easy axis. Exploiting the results of the S-W model, it has been proposed to tilt the easy axis of media, or head field to reduce the switching field.[47] However, both approaches are difficult in practice. Victora et al.[43] theoretically predicted exchange coupled composite (ECC) media consisting of magnetically hard and soft regions within each grain to reduce the switching field, which was subsequently demonstrated by Wang et al.[48,49] ECC media recently draws the attention due to its easy fabrication process and its potential application in reducing the switching field. Initially Victora et al.[43] mentioned that the easy axis of magnetization in the hard layer in ECC media should be pointed along the film normal direction while that of the soft layer in the film plane. Application of reverse field initially causes the magnetization of the soft region to switch first and thus change the angle of effective field (sum of the applied field and the exchange field) to the hard region, thus reducing the switching field of the ECC media in comparison to that of the hard layer (without any soft layer). However, it was subsequently proposed that the easy axis of the soft layer could be either in-plane or out-of-plane.[50] The in-plane easy axis of soft layer may cause extra noise due to the increased intergranular exchange interaction. As a result, out-of-plane easy axis in the soft magnetic layer is preferred. The ECC media enjoys other advantages over PMR such as it switches faster than the PMR and is insensitive to wider range of easy axis

distribution than that of the PMR. Although, ECC media has advantage to reduce the writing field, it has following limitations in using high K_u materials such as $L1_0$ CoPt and FePt.

- The optimum performance of ECC media is only capable of reducing the switching field to half of its original value.
- The maximum limit of writing head is still 24 kOe, which is insufficient to write $L1_0$ CoPt and FePt that may exhibit coercivity above 100 kOe.
- In ECC media, there is a challenge to control the grain size of CoPt and FePt during heat treatment to achieve desired $L1_0$ ordered phase.

1.4 Review of current CoCrPt perpendicular magnetic recording media

The hard disk drives based on the perpendicular recording technology have been commercialized. CoCrPt-SiO_2 deposited on (0002) texture Ru underlayer is used in such drives as recording layer. Small grain size of 7 nm with well defined grain boundaries has been achieved by Oikawa et al.[51] In this media, Cr segregates with oxide materials at grain boundaries forming CrO, and reduces intergranular exchange interaction.[52,53] However, it is reported that Cr does not completely segregate at grain boundaries,[54] and partially remains inside the grain forming Co_3Cr[55]. The presence of Cr inside the grain reduces the K_u value.[25,56,57] The segregation of Cr varies proportionally with the grain size, resulting in an anisotropy distribution that leads to wider transitions and hence poorer *SNR*.[34] As a result, it is necessary to keep the grain-to-grain value of anisotropy field as uniform as possible.[23] To do this, the composition of grains must be uniform, which cannot be achieved in the presence of

Cr. Different materials are investigated as a substitute of Cr, but they further deteriorates the K_u value.[58] Addition of B into CoCrPt helps to increase the *SNR* due to grain segregation and grain size reduction, but it induces stacking fault density resulting in reduced K_u value.[59] The *hcp* CoPt appears to be promising media with increased K_u for large areal density. The *hcp* CoPt can be achieved at room temperature unlike the $L1_0$ phase FePt and CoPt, which require high deposition temperature.

In addition to large K_u, large *SNR* is vital to achieve large areal density. As discussed in section 1.1.2 that small grain size, narrow grain size distribution and reduced intergranular exchange interaction is necessary in recording layer for large *SNR*. The traditional method of controlling grain size and intergranular exchange interaction in CoCrPt-SiO_2 recording media is based on manipulating the SiO_2 composition and/or adding the oxygen with Ar during the deposition of recording layer. Higher percentage of SiO_2 reduces both the grain size (5-6 nm) and K_u value.[60,61] The reduced value of K_u have adverse impact on increasing areal density. Zheng et al.[62] have investigated the effects of oxygen incorporation and reported that addition of oxygen improves the *SNR*. However, entrapped oxygen ions inside the grain deteriorate magnetic properties. Dual-layer structure of Ru, in which bottom layer of Ru is deposited at low Ar pressure and top layer Ru deposited at high Ar pressure, is used to reduce the intergranular exchange interaction.[63,64] Piramanayagam el al.[65] has successfully achieved the grain size down to 5.5 nm using synthetic nucleation layer between the top and bottom Ru layer. The search of nucleation layer has been largely based on a trial-and-error approach. Other approaches of controlling the grain size and intergranular exchange interaction have been based on the Thornton diagram, wherein the growth of thin film favors columnar grains with voided region

between them.[66] Such microstructures may be achieved by controlling the deposition parameters in such a way that adsorbates do not have sufficient kinetic energy to jump more than few atomic spacing. High Ar pressure and low temperature are suitable conditions. However, detailed understanding of Ar pressure on texture growth needs further study. Based on the pros and cons of different methods to achieve large *SNR*, it is necessary to understand the roles of various parameters to control the grain size, grain size distribution and intergranular exchange interaction in order to optimize the parameters for a large *SNR*.

1.5 Studies of phase miscibility, growth induced structural anisotropy and strain in CoCrPt thin films

The recording technology is gradually switching from the LMR to PMR. In section 1.2.2, it has been mentioned that PMR requires perpendicular magnetic anisotropy (PMA). The PMA in CoCrPt granular magnetic recording media strongly depends on the relative compositions of constituent elements,[56] and their distribution inside each grain.[54] Hence, it is of scientific and technological importance to investigate the alloying and phase separation of multi-element recording media to understand the origin of PMA. The conventional x-ray diffraction (XRD) technique, common for structural characterization of materials with long-range order (LRO) does not necessarily provide correct information on the phase miscibility[67,68] as a result origin of magnetocrystalline anisotropy cannot be understood. In addition, the growth induced structural anisotropy, in which the surrounding compositional environment of element of interest in the multi-element system is different in the film plane and along the film normal direction, cannot be detected from XRD.

Extended x-ray absorption fine structure (EXAFS), a synchrotron x-ray radiation based technique is a powerful tool to provide short-range order information such as the number and type of nearest neighbors, interatomic distance and local geometry of particular element in each phase of a complex system.[69-73] This provides information such as the number and types of elements surrounding the element of interest in the multi-element multiphase system. The x-ray generated by synchrotron is linearly polarized that allows for identification of the type of nearest neighbors in the film plane and along the film normal direction, leading to information of structural anisotropy in the parallel and perpendicular directions of the film.[74-77] The special characteristics of polarized EXAFS to separately measure the nearest neighbors distance in the film plane and along the film normal direction reveal the compressive/tensile strain in two different directions[78] at short-range order, which cannot be identified from conventional techniques like XRD and transmission electron microscopy (TEM). Polarized EXAFS is a very powerful technique to investigate the phase miscibility, growth induced structural anisotropy and strain analysis in the short-range order.

1.6 Research objective

The current main objective of hard disk drive is to increase the areal density to 1 Tbit/in^2 and beyond. In order to accomplish this goal, the media should have large thermal stability and SNR, and must be writable. The review done in the previous sections indicates that the potential recording technologies such as HAMR and patterned media involving high K_u materials such as $L1_0$ FePt, require many more years of research before these can be realized in commercial application. The upper limit of current CoCrPt media is anticipated as 600 Gbit/in^2. To further increase the

recording density, it is necessary to increase the K_u of current media, which can be written using existing read-write system. The presence of Cr reduces the K_u of CoCrPt thin films. Therefore, in this thesis, the *hcp* CoPt thin films were studied to increase the K_u value. The main objective was to find the optimum compositions of Co and Pt with the best magnetic properties in terms of high K_u, large coercivity and large thermal stability. In order to study the physical mechanisms responsible for improved magnetic properties, the phase miscibility, growth induced structural anisotropy and strains were investigated in CoPt films by polarized EXAFS. The microstructures of magnetic layer influence the magnetic properties and recording performance of recording media. As a result, texture and microstructure are controlled by layer engineering approach. It is well known that seedlayer (first layer deposited on the substrate) and underlayer (layer deposited prior to the magnetic layer) greatly influence the microstructure and magnetic properties of the magnetic layer. In this thesis, the effects of microstructure of Ta seedlayer and Ru underlayer on magnetic properties of CoPt were investigated. Ru is used as an underlayer material because both Ru and Co are *hcp* structure. The lattice parameter *a* of Ru is 8.0% larger than that of Co and therefore favors the hetero-epitaxial growth of the *hcp* CoPt (0002) texture on the Ru (0002). The effects of process parameters of Ru to attain (0002) texture, and other desired microstructures to achieve large *SNR* were investigated.

1.7 Thesis outline

This thesis is organized into 8 Chapters. Chapter 1, is an introduction to the magnetic recording media. Future recording media such as HAMR, patterned media and ECC media for high density magnetic recording are reviewed. In Chapter 2, a brief introduction to experimental techniques used for the fabrication and

characterization of samples is made. In Chapter 3, the effects of Pt compositions on structure and magnetic properties of $Co_{100-x}Pt_x$ thin film media were studied. In Chapter 4, the phase miscibility, growth induced structural anisotropy and strain in the CoPt films were studied using polarized EXAFS. In Chapter 5, the effects of CoPt thickness on microstructural evolution and magnetization reversal mechanism were addressed. In Chapter 6, the effects of interface roughness of Ta seedlayer on magnetic properties were studied. In Chapter 7, the effects of microstructure of Ru underlayer on microstructures and magnetic properties of CoPt films were investigated. The effects of thickness, deposition pressure and dual-layer structure of Ru were studied. In chapter 8, conclusion of the thesis was compiled and future works related to the *hcp* CoPt media were addressed.

Chapter 2
Experimental techniques

This chapter was mainly focused on the samples fabrication and characterizations techniques, which were used during the course of study. Fabrication of samples was carried out using magnetron sputtering, and compositions of different elements in the films were analyzed by Rutherford backscattering spectroscopy. The magnetic characterizations were carried out by vibrating sample magnetometer (VSM), alternating gradient force magnetometer (AGFM), torque magnetometer and magnetic force microscopy (MFM). Structural and microstructural characterizations were made by XRD, TEM, atomic force microscopy and polarized EXAFS.

2.1 Samples fabrication by sputtering

In this work, all films were deposited by magnetron sputtering. This technique is well accepted in the magnetic recording industries to fabricate magnetic media, because it provides high deposition rate, excellent film uniformity over large area, and applicable to wide range of metallic as well as non-metallic materials. Independent control over many parameters like deposition rate, deposition power, working gas pressure and temperature, which influence the structure and related properties, makes it very versatile.

The ejection of atoms from the surface of materials (the target) by bombardment with high energetic particles is called sputtering. More in-depth knowledge about the sputtering process and physics can be found in many textbooks.[79-81] In this study all films were deposited by high vacuum dc magnetron sputter system assembled in the laboratory at Data Storage Institute, Singapore. The

system has four confocal cathodes, and the substrate holder is situated in the center above the cathodes. The substrate holder was rotated at 40 revolutions per minute (rpm) in order to ensure the film uniformity during deposition. The sputtering rate was adjusted by sputtering power and working gas pressure. The film thickness was controlled by the sputtering time, which was calibrated using TEM cross-section image. Before sputter deposition, the sputtering chamber was pumped down to ~10^{-8} Torr to reduce any contamination of the film from the ambient gases. The chamber was then back filled with sputtering gas to a pressure of a few mTorr. In this work, 99.999 % pure Ar gas was used as the sputtering gas.

2.2 Composition analysis by Rutherford backscattering spectroscopy

Rutherford backscattering spectroscopy (RBS) is a quantitative, depth profiling, non-destructive technique available for measurement of elemental compositions of films. Its detection limit ranges from a few part per million (ppm) for heavy elements to a few percent for light elements. In order to quantify the compositions of constituent elements of sample, the sample is bombarded with a mono-energetic beam of high energy particles, typically helium ions with energy of a few MeV. A fraction of the incident ions are scattered backwards from the target atoms at the near surface region. The backscattered ions are detected by solid state detector placed at certain angle, which measured their energy.[82,83]

The energy of the backscattered particle is related to the depth and mass of the target atom, given by

$$E = K(E_0 - E_{in-loss}) - E_{out-loss} \tag{2.1}$$

where E_0 is the energy of incident particle, $E_{in\text{-}loss}$ the energy loss of the incident particle in traversing the depth, *d,* before scattering, $E_{out\text{-}loss}$ the energy loss of the scattered particle in traversing the depth, *d,* after scattering and *K* the kinematical factor, which is given by

$$K = \left(\frac{\left[1-(M_1/M_2)^2 \sin^2\theta\right]^{1/2} + (M_1/M_2)\cos\theta}{1+(M_1/M_2)} \right)^2 \tag{2.2}$$

where M_1 and M_2 are the masses of the incident ion and the target atom, respectively, and θ the angle between the trajectory of incident ion before and after the scattering. As a result, the energy of incident ions backscattered from the heaver target atom is larger than that backscattered from the lighter atoms. The relative number of backscattered ions into a given solid angle for a given number of incident ions is proportional to the concentration of target atom and given by differential scattering cross-section

$$\frac{d\sigma}{d\Omega} = \left[\frac{Z_1 Z_2 e^2}{4E}\right]^2 \left[\frac{4}{\sin^4\theta}\right] \frac{\left[\sqrt{1-\left(\frac{M_1\sin\theta}{M_2}\right)^2} + \cos\theta\right]^2}{\sqrt{1-\left(\frac{M_1\sin\theta}{M_2}\right)^2}} \tag{2.3}$$

where, Z_1 and Z_2 are the atomic numbers of the incident ion and the target atom, respectively, *E* the energy of incident ion and *e* the electronic charge. Comparing the numbers of backscattered ions with different energy (corresponding to the different target atoms) provide the relative composition of different target atoms. In this study a mono-energetic particles of 2 MeV He^+ was used and PIPS detector of diameter 50 mm was kept at a distance of 15 mm from the sample surface at an angle

of 150º. The data was analyzed using a standard XRump software. The schematic of the RBS is shown in Fig. 2.1.

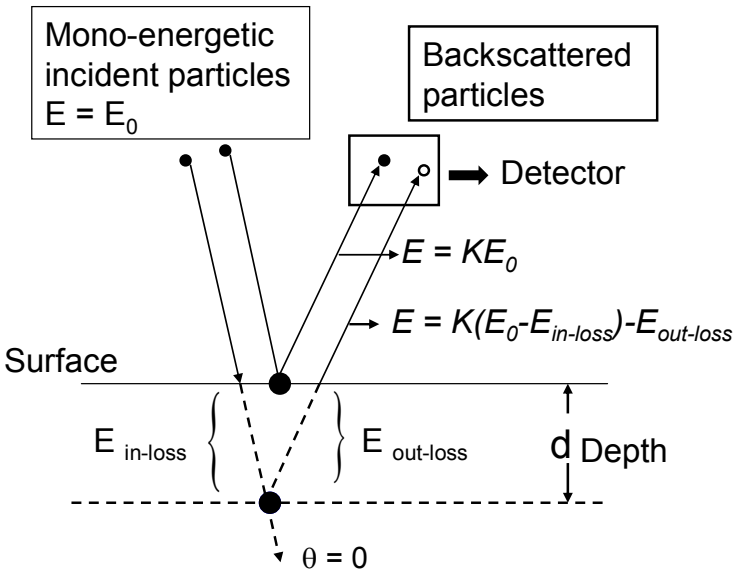

Figure 2.1: Schematic diagram showing various energy loss processes in Rutherford backscattering spectroscopy. Energy is lost by momentum transfer between the probe particles and the target particles, and as the probing particles traversed the sample material both before and after scattering.

2.3 Magnetic characterization

2.3.1. Vibrating sample magnetometer

Vibrating sample magnetometer (VSM) is a very common instrument used for characterization of magnetic materials because it offers the best combination of performance and capabilities for different kinds of magnetic measurements such as hysteresis loop, DC demagnetization (DCD) curve and angular dependence of hysteresis loops. In this study, we used VSM 880 made by Digital Measurement Systems Inc. and VSM 10 supplied by ADE. Both VSMs are capable to measure the sample at different angle with respect to the field direction, yielding information on coercivity (the negative magnetic field at which magnetization reaches zero after

saturating the sample in the positive field) and remanent coercivity (the negative magnetic field requires to bring the magnetization to zero once it is removed after saturating the sample in the positive field) at different angle. More detail about the working principle of VSM can be found elsewhere.[84]

2.3.1.1 Measurement of hysteresis loop

For hysteresis loop measurement, a DC field (H_{sat}) strong enough to saturate the sample along the applied field direction is applied. Thereafter, the field decreases in user defined steps. The magnetization at each step is measured. The process is continued when magnetic field reaches to $-H_{sat}$. Thereafter, to measure the full loop, the magnetic field increases to H_{sat}. A plot of applied magnetic field versus magnetization reveals the hysteresis loop. A typical hysteresis loop is shown in figure 2.2. Here, M_s is the saturation magnetization, M_r the remanent magnetization and H_c the coercivity. The ratio M_r/M_s is defined as magnetization squareness (S).

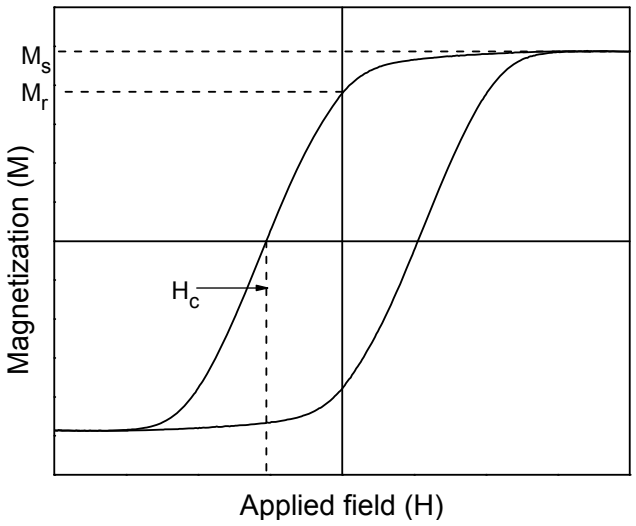

Figure 2.2: Typical hysteresis loop.

2.3.1.2 Measurement of DC demagnetization curve

In the measurement of DC demagnetization (DCD) curve, the sample is first saturated in the positive field (H_{sat}). After saturation, field is removed to bring the sample back at $H = 0$. Thereafter, a small negative field is applied and removed to bring the sample again at $H = 0$. The magnetization (without any applied field) is measured and plotted against the previously applied negative field. Subsequently a slightly larger negative field is applied and removed. The resulting magnetization is measured corresponding to the next point. This procedure is repeated until the resulting remanent magnetization become constant. The DCD curve gives information about the residual magnetization in material after removal of writing field, and reflects the irreversible component of magnetization. This is the magnetization that can be read back with the read head. DCD curve is shown in Fig. 2.3 along with the hysteresis loop. The field at intersection point of the DCD curve and the zero magnetization line is defined as a remanent coercivity (H_{cr}).

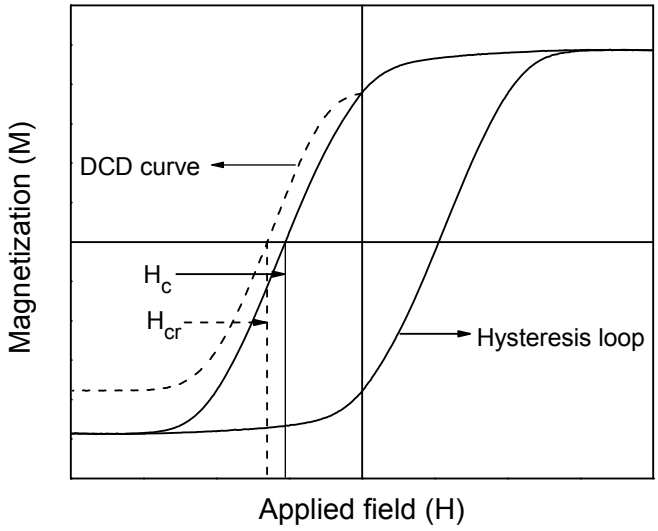

Figure 2.3: DC demagnetization curve and hysteresis loop.

2.3.1.3 Measurement of angular dependence of coercivity and remanent coercivity

The measurement of angular dependence of coercivity (H_c) and remanent coercivity (H_{cr}) are similar to that discussed in section 2.3.1.1 and section 2.3.1.2, respectively, at different angles with respect to the film normal. Conventionally it is measured in the range of 90º. It determines the magnetization reversal mechanism of magnetic thin films. The angular dependence coercivity measurement can also be used to obtain the qualitative information about the grains isolation by comparing the experimental results with the Stoner-Wohlfarth (S-W) theory and the domain wall motion theory. The non-interacting magnetically isolated grains follow the S-W model. According to the S-W theory, coercivity is defined by [84,85]

$$\frac{H_c(\theta)}{H_c(0)} = \left[\cos^{2/3}\theta + \sin^{2/3}\theta\right]^{-3/2}, 0^\circ \le \theta \le 45° \tag{2.4}$$

$$\frac{H_c(\theta)}{H_c(0)} = \sin\theta\cos\theta, 45^\circ < \theta \le 90° \tag{2.5}$$

and, according to the domain wall motion theory, coercivity is given by

$$\frac{H_c(\theta)}{H_c(0)} = \frac{1}{\cos\theta} \tag{2.6}$$

where, $H_c(\theta)$ is the coercivity at an angle θ, θ the angle between the applied field and the easy axis direction, $H_c(0)$ the coercivity when applied field is aligned along the easy axis i.e. $\theta = 0°$. In this thesis, CoPt alloy with the easy axis along the film normal was studied. Therefore, θ was defined with respect to the film normal. According to the S-W model, the angular dependence of remanent coercivity (H_{cr}) in the measured range of 90º is given by

$$\frac{H_{cr}(\theta)}{H_{cr}(0)} = \left[\cos^{2/3}\theta + \sin^{2/3}\theta\right]^{-3/2}, 0^\circ \le \theta \le 90^o \tag{2.7}$$

where, $H_{cr}(\theta)$ and $H_{cr}(0)$ is the remanent coercivity at angle θ and $\theta = 0°$, respectively.

2.3.2 Alternating gradient force magnetometer

The alternating gradient force magnetometer (AGFM) is a highly sensitive magnetic instrument with sensitivity of 10^{-8} emu compared to that of 10^{-6} emu for the VSM. The AGFM used in this project was Model 2900 MicroMag^{TM} System (Princeton Measurement). This instrument was mainly used to measure the time dependent remanent coercivity to obtain information on the thermal stability factor of the recording media. Such measurement would have taken a very long time if using a VSM.

2.3.2.1 Measurement of thermal stability factor and switching volume

In order to measure the thermal stability factor, remanent coercivity is measured for applied field of a different time duration *t*. The results are fitted to the Sharrock's formula for perpendicular recording media given by[86]

$$H_{cr}(t) = H_0\left[1-\left\{\frac{k_B T}{K_u V^*}\ln\left(\frac{f_0 t}{\ln 2}\right)\right\}^{1/2}\right] \tag{2.8}$$

where, $H_0 \approx 2K_u / M_s$ is the intrinsic switching field defined as the field at which the energy barrier for magnetization reversal is zero in the absence of thermal agitation, V^* the magnetic switching volume (a volume of recording media, which switches magnetization direction collectively), f_0 an attempt frequency, which is usually taken to be ~10^9 s^{-1}. The Sharrock's formula can be simplified to

$$H_{cr}(t) = H_0 - H_0\left\{\frac{k_B T}{K_u V^*}\right\}^{1/2}\{\ln(f_0 t)\}^{1/2} \tag{2.9}$$

A plot between H_{cr} and $\{\ln(f_0 t)\}^{1/2}$ shows a straight line with H_0 as the intercept and $-H_0\{k_B T/K_u V^*\}^{1/2}$ as slope. The value of thermal stability factor, $K_u V^*/k_B T$, is calculated from parameters deduced for intercept and slope by linear data fitting. The equation (2.8) can be further simplified to a different form, which can be expressed as

$$H_{cr}(t) = k - \eta\frac{k_B T}{M_s V^*}\ln t \tag{2.10}$$

where k and η are the constants and defined by following equations

$$k = \frac{1}{2}H_0\left\{1 + \frac{K_B T}{K_u V^*}[(\ln f_o - \ln(\ln\ 2))]\right\}\Bigg/\left\{1 - \frac{1}{2}(\frac{H_C}{H_0})\right\} \tag{2.11}$$

$$\eta = \frac{1}{\left\{1 - \frac{1}{2}(\frac{H_C}{H_0})\right\}} \tag{2.12}$$

By fitting the remanent coercivity measured for different applied field duration in equation (2.10), the value of V^* can be obtained. In the S-W model, V^* is identical to the physical particle volume. However, if the situation deviates from the S-W model, the value of V^* could differ from the physical particle volume. If V^* is smaller than the physical particle volume, it means magnetic reversal takes place coherently at small switching unit, but over all magnetic reversal is incoherent. Conversely, if V^* is larger than the physical particle volume, then magnetic interaction between particles is large. Note that physical particle may consist of many grains (as determined by x-ray grain size or TEM dark field imaging) in its volume.

2.3.3 Measurement of magnetocrystalline anisotropy constant

In magnetic recording media, K_u is an important parameter to determine the thermal stability factor. Hence it is essential to measure the K_u value. In this study, the K_u value is determined using torque magnetometer, and the area enclosed between the in-plane and out-of-plane hysteresis loops.

2.3.3.1 Measurement of K_u by torque magnetometer

The torque magnetometer is used to determine the K_u of magnetic samples. The derivation of K_u is based on a principle that when the anisotropic sample is placed in the magnetic field at a certain angle, the field tries to force the magnetization of the sample to align along its direction, whereas the anisotropy energy of the sample attempts to keep the magnetization in the easy axis direction. As a result, the field exerts a torque on the sample. The torque is equal to the negative of the first derivative of anisotropy energy, E_a, with respect to the angle θ between magnetization direction and easy axis.

$$L = -\partial E_a / \partial \theta \tag{2.13}$$

In the torque measurement, the sample is rotated in the plane containing the easy axis and magnetic field. The torque, which is function of θ, can be expressed by Fourier series

$$L(\theta) = \sum_n [A_n \sin(2n\theta) + B_n \cos(2n\theta)] \tag{2.14}$$

where n = 0, 1, 2, 3…is a natural number. In practice, the angle θ is defined in such a way that at $\theta = 0$, $L = 0$, therefore $B_n = 0$. In the case of uniaxial anisotropy, as for the samples investigated in this thesis, the term of higher order anisotropy greater than two are ignored. Therefore equation (2.14) is simplified to

$$L(\theta) = A_0 + A_1 \sin(2\theta) + A_2 \sin(4\theta) \tag{2.15}$$

where, the first term does not have any contribution to anisotropy. Generally during the measurement, the anisotropy energy (E_a) of thin film sample has two components, the magnetocrystalline anisotropy energy (E_c) and the demagnetization energy (E_d) due to the shape anisotropy. The magnetocrystalline anisotropy energy and the demagnetization energy can be respectively written as

$$E_c = K_1 \sin^2\theta + K_2 \sin^4\theta \tag{2.16}$$

$$E_d = \frac{1}{2}\left[M_s^2 N_{//} \cos^2\theta + M_s^2 N_{\perp} \sin^2\theta\right] \tag{2.17}$$

where, $N_{//}$ and $N_{\perp}$ denote the demagnetization factor along and perpendicular to the easy axis, respectively, and M_s is the saturation magnetization. Therefore, the magnetic anisotropy energy is given by

$$E_a = K_1 \sin^2\theta + K_2 \sin^4\theta + \frac{1}{2}\left[M_s^2 N_{//} \cos^2\theta + M_s^2 N_{\perp} \sin^2\theta\right] \tag{2.18}$$

$$L(\theta) = -\partial E_a / \partial\theta = -(K_1 + K_2 - K_d)\sin 2\theta + (K_2/2)\sin 4\theta$$

$$L(\theta) = -K_{u(eff)} \sin 2\theta + (K_2/2)\sin 4\theta \tag{2.19}$$

where $K_{u(eff)} = K_u - K_d$ is the effective anisotropy, $K_u = K_1 + K_2$ and $K_d = \frac{1}{2}M_s^2(N_{//} - N_{\perp})$ the demagnetization energy. Equation (2.19) indicates that at point $\theta = 0^o$ and $\theta = 180^o$, where magnetization direction points along the easy axis direction, the slope of the torque curve should be negative for a positive value of $K_{u(eff)}$. A Comparison between equation (2.15) and (2.19) indicates that the effective anisotropy, $\left|K_{u(eff)}\right| = \left|A_1\right|$. This method of determination of K_u is applicable if applied field is significantly larger than the anisotropy field so that an angle between the easy axis and applied field (φ) remains equal to angle between easy axis and magnetization

direction (θ). In this experiment, the maximum applied field is 12 kOe, which is less than the anisotropy field. This field is not high enough to force the magnetization to lie exactly in the field direction. As a result, in this study, torque curve correction method is used to determine the K_u value. Using this method the K_u value can be precisely determined for applied field one fifth of anisotropy field.[87] In this method, the experimental result of torque versus φ is converted to torque versus θ. The angles φ and θ is defined in Fig. 2.4. The torque exerted by the magnetic field (B) is given by

$$L = M_s B \sin(\varphi - \theta) \tag{2.20}$$

$$\varphi - \theta = \sin^{-1}(L / M_s B) \tag{2.21}$$

Using equation (2.21), the torque can be obtained as function of θ for known value of saturation magnetization, which is determined from hysteresis loop. Thereafter, each point of the experimental torque curve is re-plotted as a function of θ. The torque versus θ curve was then Fourier transformed to obtain the $K_{u(eff)}$. Thereafter, the value of K_u can be calculated according to formula $K_u = K_{u(eff)} + 2\pi M_s^2$.[88]

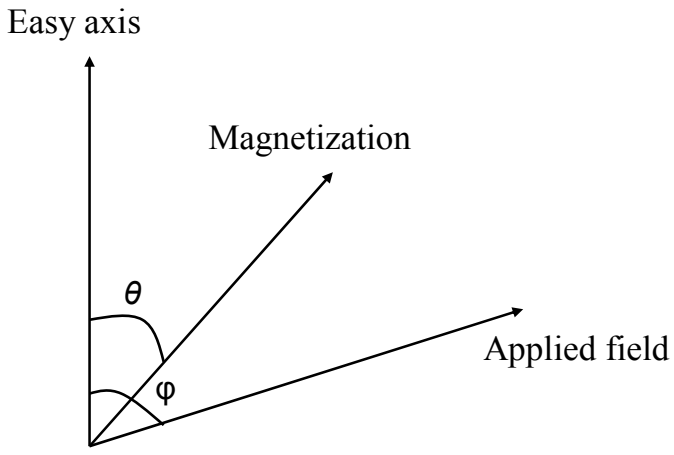

Figure 2.4: Orientation of easy axis, magnetization and applied field directions.

2.3.3.2 Measurement of K_u by area enclosed between the in-plane and out-of-plane hysteresis loops

This method of determining K_u from magnetization curve is based directly on the definition of anisotropy energy, namely, the energy stored in the crystal when it is magnetized to saturation along the hard direction. The value of K_u in this method is evaluated by taking the area $[\int_0^{M_s} H(M)dM\ ]$ enclosed between magnetization curves of the in-plane and the out-of-plane direction in the first quadrant of *M-H* loop, subject to the condition that the films are saturated in both directions. Since, the in-plane hysteresis loops of samples studied in this thesis were not fully saturated under the maximum applied field, therefore saturation field of the in-plane magnetization direction was obtained by extrapolating the in-plane and the out-of-plane hysteresis loops corresponding to the anisotropy field H_k.

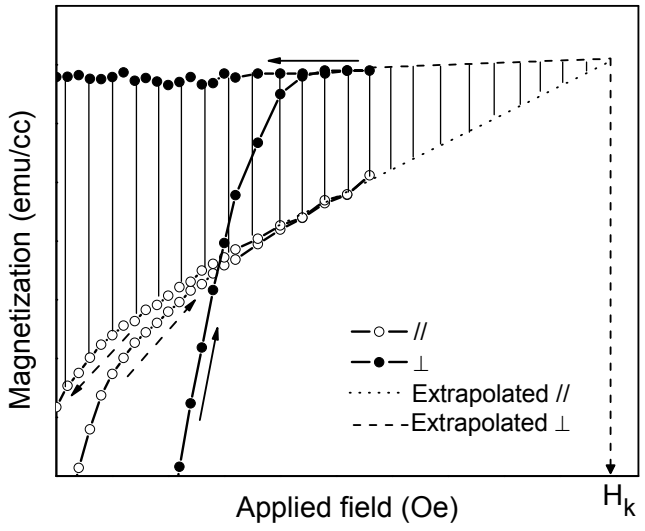

Figure 2.5: Schematic diagram for calculation of K_u, using difference in area between the in-plane and out-of-plane hysteresis loops.

In Fig. 2.5 the shaded area shows the K_u value. The K_u value determined by this method is lower than that determined by torque method as discussed in previous

section, because this method does not take into account the effect of the demagnetization energy.

2.3.4 Magnetic force microscopy

Magnetic force microscopy (MFM) belongs to the scanning probe microscopy (SPM) group. It is used to map the magnetic field strength across the sample surface using a magnetized tip [89]. The MFM relies on the interaction of two magnetic bodies, the probe and the sample. In MFM, a tapping cantilever equipped with a special tip is first scanned over the sample surface to obtain topographic information. Using the Lift Mode, the tip is then raised just above the sample surface. Lift-mode allows the imaging of relatively weak but long-range magnetic interactions while minimizing the influence of topography. The surface topography is scanned while being monitored for the influence of magnetic forces, which are measured using the principle of force gradient detection. In the absence of magnetic forces, the cantilever has a resonant frequency f_0. This frequency shifts by an amount Δf proportional to vertical gradients in the magnetic forces on the tip and form the domain pattern. More detailed information about MFM can be found elsewhere.[90]

2.4 Structure and microstructure characterization

2.4.1 X-ray diffraction

The x-ray diffraction (XRD) is a technique for phase analysis and mosaic distribution of crystalline solid with size larger than that of the x-ray coherence length. The basic principle of x-ray diffraction is governed by the Bragg's law, which is given by equation

$$2 d_{hkl} \sin \theta = n \lambda \tag{2.22}$$

where, d_{hkl} is the inter-planer spacing of {hkl} plane, θ the angle between x-ray beam and diffracting plane, n a positive integer that defines the order of diffraction and λ the wavelength of x-ray. More detailed information about XRD can be obtained in the text book of B. D. Cullity[91] and B. E. Warren.[92] In this thesis, x-ray powder scans and rocking curves of all samples were measured from X'Pert Philips diffractometer using Cu K_α radiation in a continuous scanning mode.

2.4.1.1 X-ray powder scans or θ-2θ measurements

In x-ray powder scans, both the source and the detector are free to move in such a way that incident beam at an angle θ with respect to the film surface makes an angle 2θ with respect to the diffracted beam. The intensity of diffracted beam is detected at each 2θ value in the scanned range in the user defined steps, and intensity versus 2θ is plotted. In this study the abscissa of measured pattern was represented in terms of momentum transfer, $q = \frac{2\pi}{d_{hkl}} = \frac{4\pi}{\lambda}\sin\theta$. The d_{hkl}-spacing of planes parallel to the film surface can be obtained. The diffraction peaks were indexed and phases were determined by comparing the experimental peak position with standard data base from the Joint Committee on Powdered Diffraction Standard (JCPDS).

2.4.1.2 Rocking curve measurement

To investigate the quality of film texture (mosaic distribution), the rocking curves (ω scans) are measured. This method is applicable to analyze the dispersion of particular plane around the film normal direction. To measure the rocking curve of

texture peak at an angle $2\theta_i$, the detector is first fixed at an angle $2\theta_i$ with respect to incident beam. Then angle θ between incident beam and the normal direction of film plane is scanned around the value θ_i. The full-width at half-maximum ($\Delta\theta_{50}$) determined from the rocking curve is measured to study the quality of texture. Small value of the $\Delta\theta_{50}$ indicates a better quality of texture.

2.4.2 Transmission electron microscopy

Transmission electron microscopy (TEM) is a mainstay for materials characterization. The main strength of TEM is its high lateral resolution (better than 0.2 nm "point-to-point" on some instrument) and its capability to provide both image and diffraction information from a single sample.[82] In TEM, a parallel beam of electrons passes through the sample, where some of the beam is scattered by atoms to different directions. The diffracted electron beam is brought into focus in the back focal plane of objective lens, forming a two dimensional array of spots corresponding to a particular set of plane for a single crystal. For polycrystalline samples, ring patterns are observed. From diffraction pattern, the interplaner spacing can be derive using the relation

$$d_{hkl}R = \lambda L \tag{2.23}$$

where, d_{hkl} is the interplaner spacing for particular set of reflecting planes {hkl}, R the radius of particular diffraction ring, λ the wavelength of electron beam and L the distance between sample and back focal plane. The product 'λL' is known as camera constant. The transmitted electron beam and the diffracted electron beam, respectively, form bright field image and dark field image. More detail information on TEM imaging and techniques can be found elsewhere.[93]

In this study, plane-view and cross-section bright field TEM images were used to observe the microstructure of thin film media in terms of grain size, grain isolation and columnar growth. In this study JEOL 3010 and JEOL 2010 model of TEM with respective accelerating voltage of 300 keV and 200 keV were used for samples characterization.

2.4.3 Atomic force microscopy

The atomic force microscopy (AFM) is another form of SPM. It is a very powerful tool to measure the surface topography of samples at sub-nanometer scale resolution. During measurement, a fine tip is brought into close contact with sample surface without actually touching the surface. This is done by sensing the repulsive force between the probe tip and the sample surface. The tip is moved back and forth over the area of interest on sample surface to display the surface morphology. In this study AFM is used to measure the surface roughness of sample in the tapping mode. The surface roughness is quantitatively extracted from the commercial software available with the instrument. The root mean square of surface roughness (R_{rms}), defined as the standard deviation of the z value within a given area, is measured, and expressed by the relation

$$R_{rms} = \sqrt{\frac{\sum_{i=1}^{1=n} \left(Z_i - Z_{avg}\right)^2}{N}} \tag{2.24}$$

where Z_{avg} is the average Z value within given area, Z_i the current Z value and N the number of points within the given area. Detailed information about AFM can be found elsewhere.[94]

2.4.4 X-ray absorption spectroscopy

The x-ray absorption spectroscopy using synchrotron radiation is a well established technique providing information on the electronic, structural and magnetic properties of the matter. In x-ray absorption, a photon having energy greater than or equal to the energy of a core level electron is absorbed by an atom, giving rise to the transition of electron from core state to an empty state above the Fermi level.[69] The energy of absorption edges of core states is the characteristic of a particular element, which makes x-ray absorption an element selective technique. The x-ray absorption spectroscopy comprised two regions; the x-ray absorption near-edge spectroscopy (XANES) and extended x-ray absorption fine structure (EXAFS).[70] The XANES extends up to ~50 eV above the absorption edge and gives information about the electronic properties of the absorbing atom, while the EXAFS extends from ~50 eV to 1000 eV and yields information about the local atomic environment around the absorbing atom. Crystallinity (long-range order) of the sample is not required for EXAFS measurement, making it useful for noncrystalline and highly disordered materials including solutions.

2.4.4.1 Basic theory of EXAFS

The basic principle of EXAFS is governed by the photoelectric effect. When an x-ray photon of energy (E) higher than the binding energy (E_0) of core level electron is absorbed by an atom, it leads to the ejection of photoelectron. The photoelectron behaves as a outgoing spherical wave of wavelength, $\lambda = 2\pi / k$, where $k = \sqrt{(2\pi / \hbar^2)(E - E_0)}$, where $\hbar = h / 2\pi$ and h is Plank's constant. The outgoing waves scatter with neighboring atoms and generate the backscattered waves. The

constructive and destructive interference between outgoing and backscattered waves generate the oscillatory EXAFS signal because constructive interference increases the amplitude of overall wavefunction, whereas destructive interference decreases the amplitude of overall wavefunction. The schematic diagram of propagation of outgoing wave, generation of backscattered wave and interference between outgoing wave and backscattered wave is shown in Fig. 2.6. The backscattered amplitude and phase depend on the type of atom participating in the backscattering process and its distance from the center atom. As a result, one can get accurate information about local atomic environments including the average coordination number (N) of different surrounding atoms, their distance (R) to the absorber as well as the relative mean square deviation (σ^2) of distance R. The σ^2 is associated with thermal and static displacements of atoms about their equilibrium position. The atoms thermally vibrate about their equilibrium position. Defects or any other kind of disorder may generate additional static displacement from equilibrium position. These displacements reduce the EXAFS amplitude. If the atoms in the coordination shell j are distributed according to the Gaussian with standard deviation σ_j around the average distance R_j, then the EXAFS amplitude is damped by Debye-Waller factor $e^{-2\sigma_j^2 k^2}$.[74] Note that the term σ^2 that enters into EXAFS Debye-Waller factor is different than that enters into the Debye-Waller factor of conventional XRD. In EXAFS, σ^2 is the relative mean square deviation between the absorbing and backscattering atoms, while for XRD, mean square displacement of the atoms in the directions normal to the diffracting planes. Furthermore, using the polarization dependent EXAFS measurements, structural information of the in-plane and out-of-plane directions with respect to the sample surface can be separately extracted, allowing the use of EXAFS to investigate anisotropic structure.[74-77]

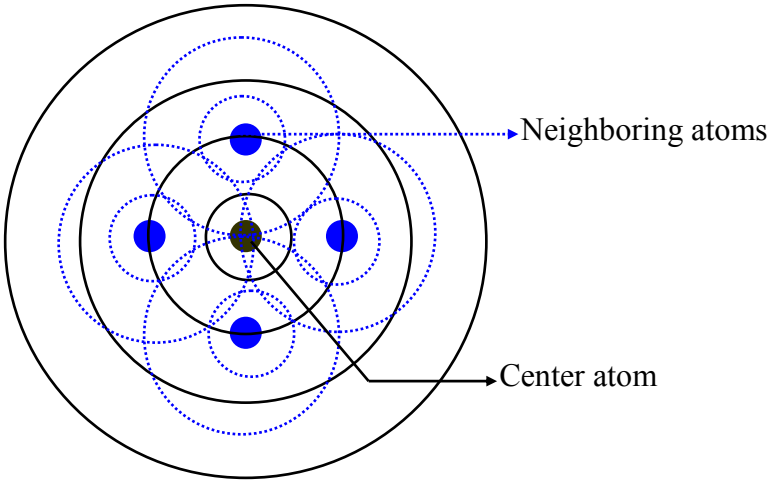

Figure 2.6: Schematic diagram of radial portion of the photoelectron waves. The solid lines indicate the outgoing waves, and dotted lines indicate the scattered waves from surrounding atoms.

The EXAFS fine-structure function signal χ(k) obtained after interference of the outgoing wave and backscattered wave is the relative oscillation of the total absorption coefficient $\mu(k)$ with respect to the absorption coefficient of an isolated atom $\mu_0(k)$. The function χ(k) for a single electron scattering is more generally written as

$$\chi(k) = S_0^2 \sum_j \frac{N_j^* F_j(k) e^{-2k^2\sigma_j^2} e^{-2R_j/\lambda(k)}}{kR_j^2} \sin[2kR_j + \delta_j(k)] \qquad (2.25)$$

where, S_0^2 is the amplitude reduction factor accounted for an overlap of initial and final wave function of passive electron, N_j^* the number of neighboring atoms, $F_j(k)$ the backscattering amplitude from each shell, $e^{-2\sigma_j^2 k^2}$ the Debye-Waller factor, R_j the distance of neighboring atoms, $\lambda(k)$ the mean free path of photoelectron and $\delta_j(k)$ the phase shift associated with the emergence of photoelectron from photo-absorber and from the scattering of the atoms in the path.

The factor $e^{-2R_j/\lambda(k)}$ takes into account the signal attenuation due to the photoelectron mean free path and core-hole life time. More details about the EXAFS may be found elsewhere.[71-73]

2.4.4.2 Polarization dependence of EXAFS

The electron in the synchrotron orbits and accelerates in the horizontal plane. As a result the x-ray produced from synchrotron is linearly polarized in the horizontal plane. The polarization dependence of x-ray is used to probe the anisotropic system. The effective co-ordination number N_j^* depends on angle between the **E** vector and the radius vector connecting the absorber to a neighboring atoms, and given by expression[76,77]

$$N_j^* = 3\sum_{i=1}^{N_j}\cos^2\theta_{ij} \qquad \text{for } K \text{ edge} \tag{2.26}$$

$$N_j^* = 0.7N_j + 0.9\sum_{i=1}^{N_j}\cos^2\theta_{ij} \qquad \text{for } L_3 \text{ edge} \tag{2.27}$$

where, θ_{ij} is the angle between the electric field vector **E** of the incoming beam and the radius vector connecting the absorber to j^{th} neighbors atom in the i^{th} coordinating shell. This indicates that in the in-plane measurement (**E** vector oriented in the plane of the sample), all atoms (including intraplanar and interplanar) except those atoms whose radial vectors are at 90º with respect to **E** vector contribute to the EXAFS signal. In the out-of-plane measurement (**E** vector oriented perpendicular to the film surface), the intraplanar atoms do not contribute in the EXAFS signal, since their radial vectors are at 90º with respect to the **E** vector.

Figure 2.7 shows a schematic diagram of hexagonal structure with **E** vector in the film plane, in which center atom (circle) is surrounded by 6 intraplanar atoms

(black) and 6 interplanar (3 above and 3 below to center atom) atoms (gray). When **E** vector lies in film plane, all 12 neighbors atoms contribute to EXAFS signal, while only 6 interplanar atoms contribute to EXAFS signal when **E** vector lies along the film normal. The weight of each atom depends on θ_{ij}. This reveals that using polarized EXAFS one can extract the information about the intraplanar and interplanar neighboring atoms around the element of interest, which is being probed by x-ray. Furthermore, polarized EXAFS provides the information about the intraplanar and interplanar radial distance of neighboring atoms. Different intraplanar and interplanar radial distance of neighboring atoms facilitate to investigate the tensile/compressive strain induced in the film at short-range order.[78]

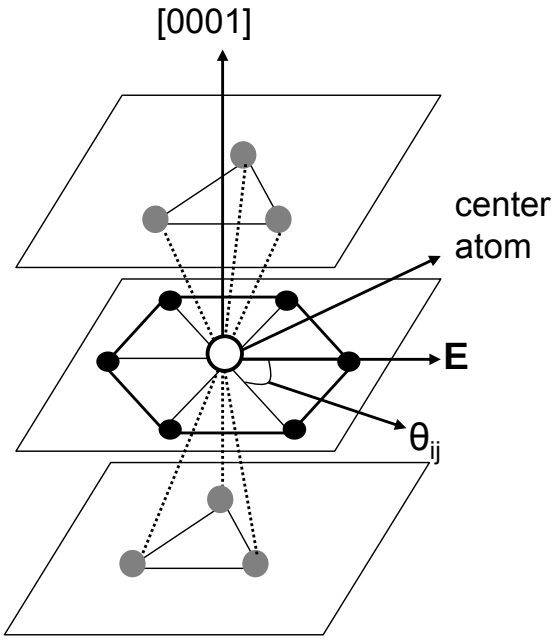

Figure 2.7: Schematic diagram of interplanar atoms (black) and intraplanar atoms (gray) around the center atom (circle) in the *hcp* structure with [0001] direction along film normal. E vector is in the film plane.

2.4.4.3 EXAFS data collection

All data were collected at Pacific Northwest Consortium-Collaborative Access Team (PNC-CAT) 20 BM beam line of Advanced Photon Source located at Argonne National Laboratory, IL-USA. The EXAFS data were collected at room temperature in fluorescence mode using 13 element solid state Ge detector which was placed at right angle to the incident beam direction. Rh coated Si mirror was used to reject the higher order harmonics. The Si (111) double crystal monochromatore was used for energy tuning. For each sample 4 and 8 scans were taken in the in-plane and out-of-plane polarization geometries, respectively, at the Co-*K* edge (7.7089 keV) and the Pt-L_{III} edge (11.5637 keV), and then all scans were averaged. However, during the out-of-plane measurement of the Pt-L_3 edge, an unwanted peak corresponding to the As-*K* edge from glass substrate at 11.8667 keV appeared which made the EXAFS data range too short to analyze after removal of EXAFS signal above the As-*K* edge. During the in-plane measurement the electric vector **E** was nearly parallel to the film surface (at 5° from film surface), while in the out-of-plane measurement the **E** vector was at 15° with the film normal.

2.4.4.4 EXAFS data reduction

The information extracted from EXAFS depends on the reduction of the experimental data. Therefore, it is necessary to follow the standard procedure in data analyses. A typical EXAFS spectrum of the raw data of Co foil is shown in Fig. 2.8(a). It is a plot of the absorption versus incident photon energy. Before data fitting, all background is removed from the signal and the signal is normalized on a per atom basis. The normalized Co EXAFS signal is shown in Fig 2.8(b). Thereafter, the *chi*

data is extracted using a suitable number of spline and k-weighting in a particular k-range. Figure 2.8(c) shows the *chi* data for number of spline 7 and k-weight 2 in the k-range $3 \leq k \leq 15$. To extract the information about the coordination number and radial distance, the *chi* data is Fourier transformed. The Fourier transform (FT) of the Co foil data is given in Fig. 2.8(d). The FT data is fitted with particular model of the sample, which leads to deliver coordination number, radial distance and Debye-Waller factor.

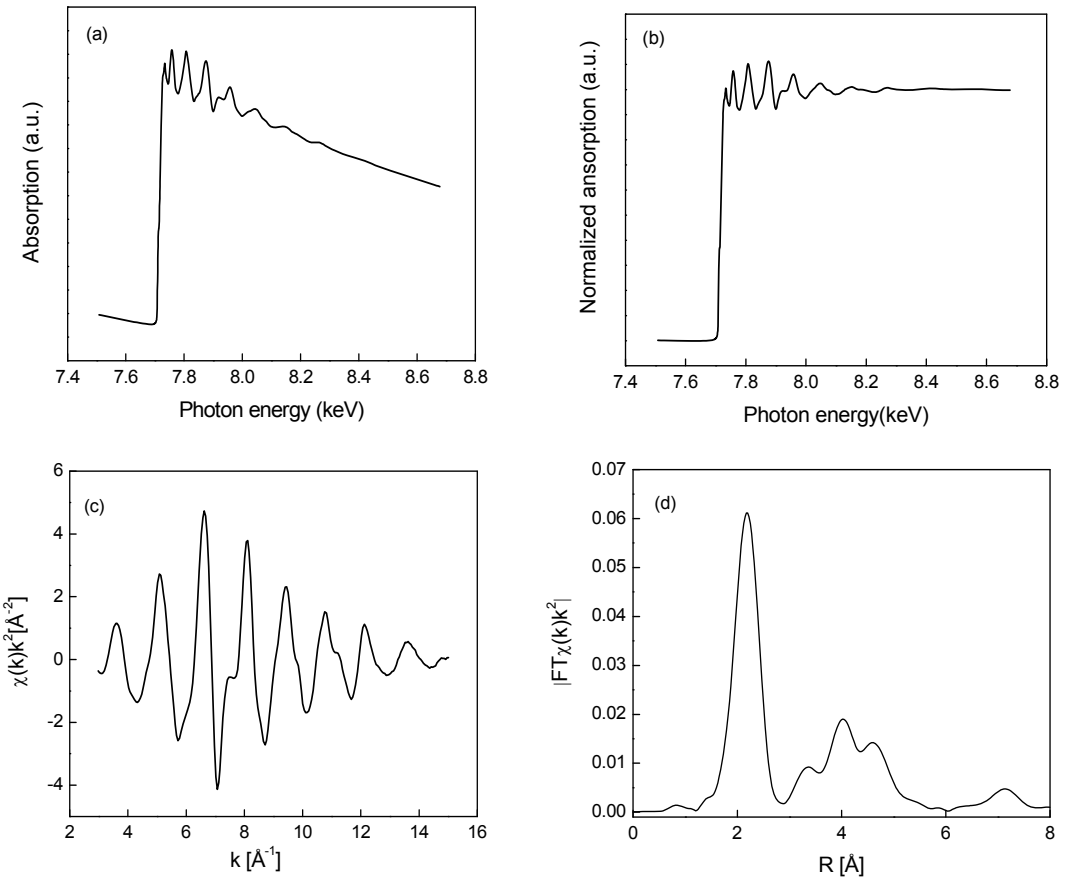

Figure 2.8: (a) Experimental EXAFS spectrum of Co foil at Co-*K* edge (Data was collected from PNC-CAT at APS). (b) Normalized EXAFS spectrum of Co foil. (c) *Chi* data of EXAFS spectrum of Co foil in the fit range of $3 \leq k \leq 15$ Å^{-1}. (d) Fourier transform of EXAFS spectrum of Co foil.

Chapter 3
Effects of Pt compositions in CoPt thin films

As discussed in Chapter one that high K_u material is essential for high areal density magnetic recording media. Granular CoCrPt-oxide thin film media is used for perpendicular magnetic recording. In this media, Cr partially segregates to grain boundaries and reduces intergranular exchange interaction, and partially remain inside the grains.[52-55] The presence of Cr inside the grains reduces the K_u value,[25,56,57] consequently limiting the areal density. In addition, the segregation of Cr varies proportionally with grain size, resulting in grain-to-grain anisotropy distribution that leads to wider transitions and hence poorer *SNR*.[33] Different elements are used to substitute Cr, which however further deteriorate magnetic anisotropy.[58] As a result, in this work CoPt media was studied to increase the K_u value.

$Co_{100-x}Pt_x$ bulk phase diagram is shown in Fig. 3.1. It shows that Co_{100} is *hcp* phase, which changes to face centered cubic (*fcc*) for x ~ 50 and becomes non-magnetic for x > 90. It indicates that magnetic properties of CoPt media depend on their relative compositions. Increasing Pt compositions in Co increase the K_u value[95] at the risk of increased stacking fault at higher Pt compositions.[56] The existence of stacking faults cause a lower K_u and high dispersion in K_u values,[96] resulting in reduced thermal stability and *SNR*. Hence, first and foremost objective of this chapter was to find out the optimum compositions of Co and Pt to achieve the best magnetic properties such as high K_u, large coercivity and large thermal stability factor.

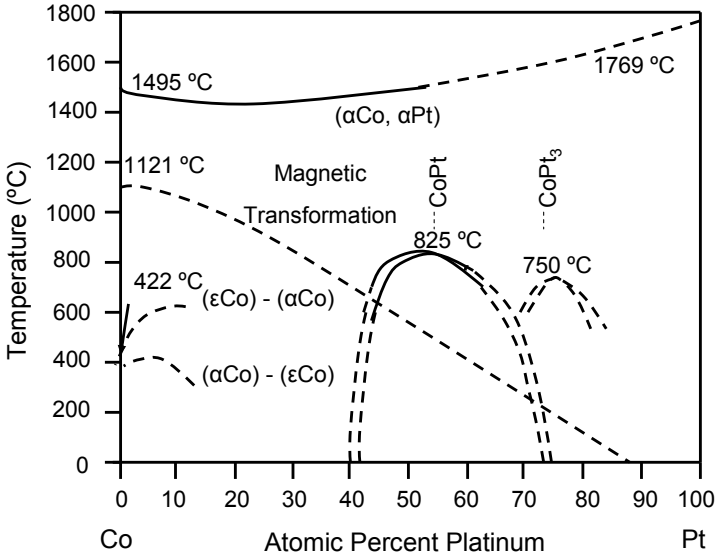

Figure 3.1: Co-Pt binary alloy phase diagram.[94]

3.1 Experimental methods

Figure 3.2 shows the schematic diagram of layers structure. To investigate the effects of Pt compositions on structure and magnetic properties of $Co_{100-x}Pt_x$, thin films of Pt(2 nm)/$Co_{100-x}Pt_x$($0 \leq x$ at. % ≤ 43)(20 nm)/Ru(30 nm)/Pt(2 nm)/Ta(5 nm)/glass were deposited. The top most layer of 2 nm Pt was deposited as a protective layer to $Co_{100-x}Pt_x$ film. Ru/Pt underlayers were deposited to induce (0002) texture in $Co_{100-x}Pt_x$ films to attain perpendicular magnetic anisotropy. Ta seedlayer was used to provide clean and smooth surface to underlayer. No substrate heating was carried out during the deposition process. The thickness of all layers was nominal, which was calibrated by deposition rate and time, and further confirmed using cross-section TEM images within the uncertainty of 5%. The alloy compositions of deposited films were confirmed by Rutherford backscattering (RBS). The base pressure was lower than $5x10^{-8}$ Torr. The $Co_{100-x}Pt_x$ magnetic layer, Ru underlayer, Pt intermediate layer and

capping layer, and Ta seedlayer were deposited at 10 mTorr, 0.5 mTorr, 3 mTorr and 2 mTorr Ar, respectively.

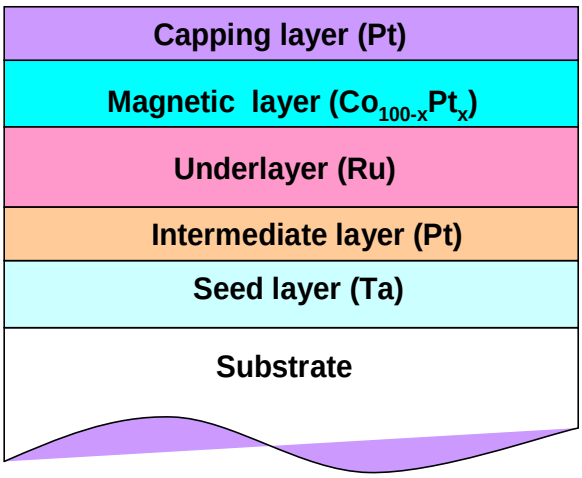

Figure 3.2: Schematic diagram of layers structure.

3.2 Results and discussion

3.2.1 Crystallographic structure of $Co_{100-x}Pt_x$ films

Figure 3.3 shows the x-ray powder scans of $Co_{100-x}Pt_x$ films for $0 \leq x \leq 43$. All samples exhibited peaks corresponding to the magnetic layer and underlayer only. No other peaks corresponding to the Pt intermediate layer/capping layer and Ta seedlayer were detected. It revealed that these layers were either amorphous or their crystal size were less than the x-ray coherence length and could not be detected during the measurement. Co_{100} film showed only one peak of magnetic layer corresponding to the momentum transfer (q) of 3.089 $Å^{-1}$ (d-spacing of 2.0403 Å). This peak position corresponded to either the *fcc* Co (111) or *hcp* Co (0002), which could not be resolved by XRD. This peak continuously shifted towards a lower q values with increasing the Pt compositions, partially overlapping with the Ru (0002) peak. This was attributed to

the expansion of CoPt lattice with increasing Pt compositions, as Pt (atomic size 2.78 Å) was larger than that of Co (atomic size 2.50 Å).

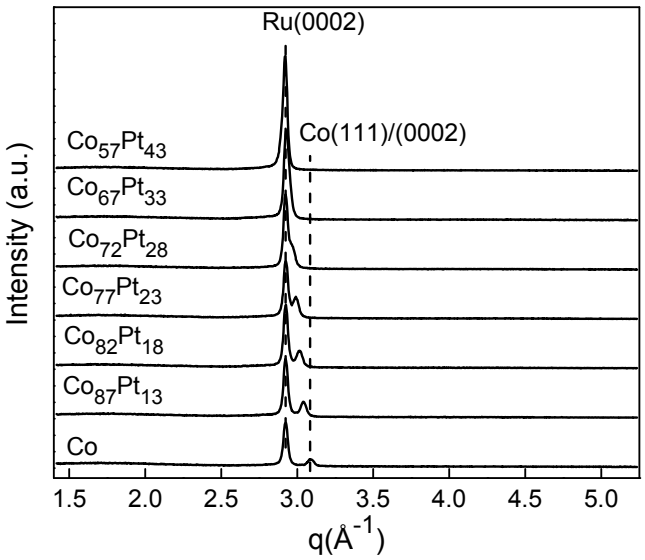

Figure 3.3: X-ray powder scans of Pt(2 nm)/$Co_{100-x}Pt_x$ (20 nm)/Ru(30 nm)/Pt(2 nm)/Ta(5 nm)/glass, for x = 0, 13, 18, 23, 28, 33 and 43 at.%. Momentum transfer, $q = 2\pi / d_{hkl}$

3.2.2 Microstructure of $Co_{100-x}Pt_x$ films

Figures 3.4(a) and 3.4(b) show the columnar growth, observed from bright field cross-section TEM images of Co_{100} and $Co_{72}Pt_{28}$ films, respectively. Figures 3.4(c) and 3.4(d) show the corresponding planar images. It indicated that Pt alloying resulted in a smaller columnar width and increased grain isolation compared to the Co_{100} film. The average column width of $Co_{72}Pt_{28}$, estimated by the arithmetic mean of their minimum and maximum dimensions from about 200 grains was 9.0 ± 1.7 nm. However, with further increasing the Pt composition to 43 at.%, the grain diameter increased while grain isolation decreased (Fig. 3.4(e)).

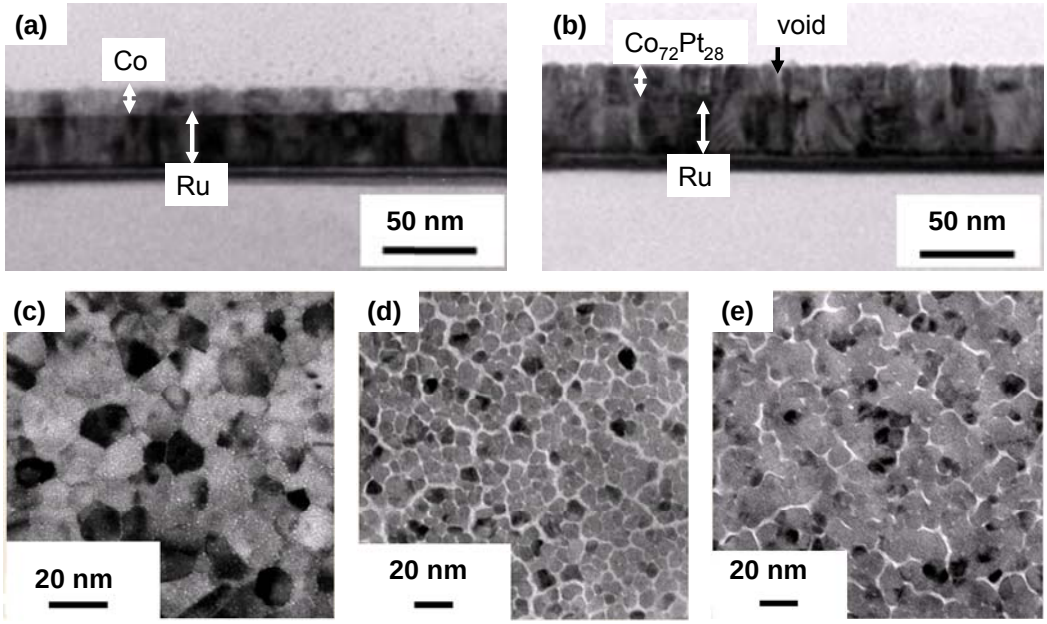

Figure 3.4: Bright field cross-section TEM images of (a) Co_{100}(20 nm) and (b) $Co_{72}Pt_{28}$(20 nm). Bright field plane-view TEM images of (c) Co_{100}(20 nm), (d) $Co_{72}Pt_{28}$(20 nm) and (e) $Co_{57}Pt_{43}$(20 nm) films deposited on Ru(30 nm)/Pt(2 nm)/Ta(5 nm)/glass.

3.2.3 Magnetic properties of $Co_{100-x}Pt_x$ films

3.2.3.1 Squareness

In order to investigate the effects of Pt compositions on magnetic properties of $Co_{100-x}Pt_x$ films, the in-plane and out-of-plane hysteresis loops of all samples were measured. Figures 3.5(a)-3.5(d) show the hysteresis loops of selected samples for different Pt compositions. The in-plane squareness, $(S_{//} = M_{r//} / M_s)$, and out-of-plane squareness, $(S_{\perp} = M_r / M_s)$, were evaluated from hysteresis loops (here $M_{r//}$ and $M_{r\perp}$ are the remanent magnetization in the in-plane and out-of-plane directions, respectively, and M_s the saturation magnetization). Figure 3.6 shows the variation of $S_{//}$ and $S_{\perp}$ with the Pt compositions. It showed that for Co_{100}, $S_{//}$ was 0.90 and $S_{\perp}$ was 0.01 indicating that Co_{100} had the in-plane easy axis of magnetization.

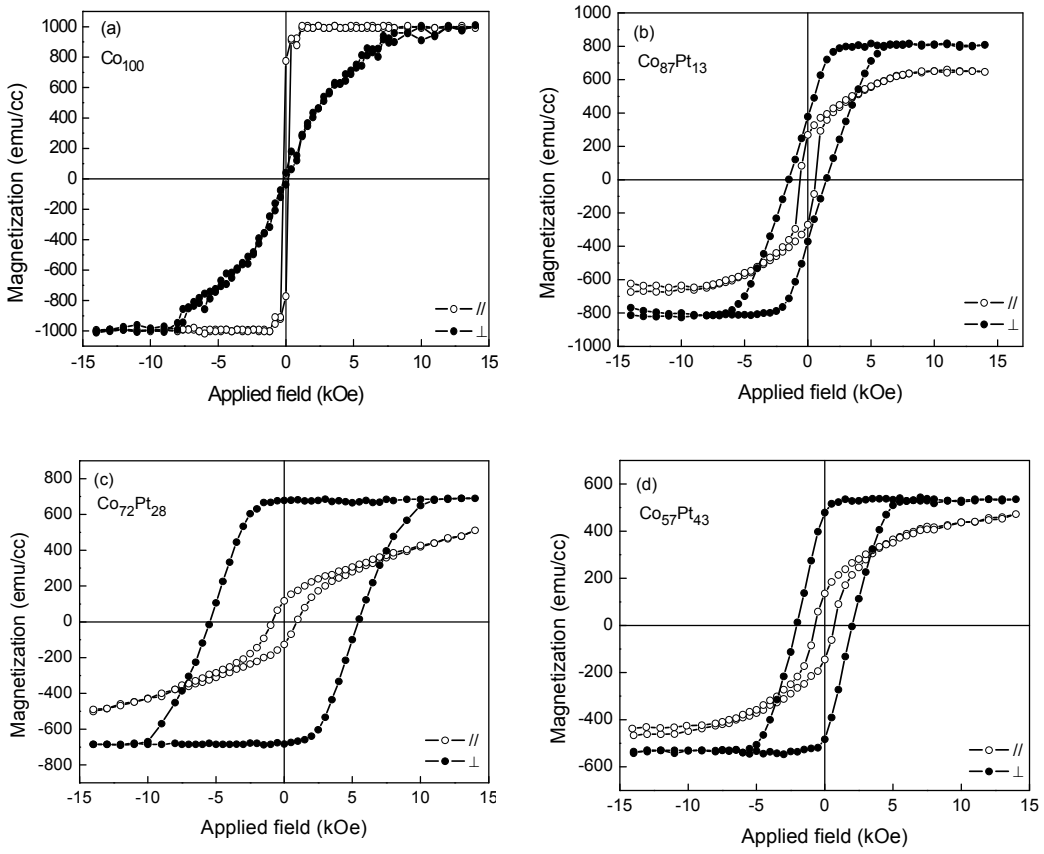

Figure 3.5: In-plane and out-of plane hysteresis loops of 20 nm thin film of (a) Co_{100}, (b) $Co_{87}Pt_{13}$, (c) $Co_{72}Pt_{28}$ and (d) $Co_{57}Pt_{43}$ deposited on Ru(30 nm)/Pt(2 nm)/Ta(5 nm)/glass.

With increasing the Pt compositions $S_{//}$ decreased drastically and reached a minimum at 28 at.% Pt and increased slightly with further increasing the Pt composition to 43 at%. The $S_{\perp}$ increased rapidly to unity at 23 at.% Pt and decreased slightly at 43 at.% Pt. The $S_{\perp}$ was always larger than that of the $S_{//}$ in the experimental range of 13-43 at.% Pt compositions. It indicated that the addition of Pt changed the easy axis of magnetization of Co from the in-plane to out-of-plane direction, as shown by the hysteresis loops in Fig. 3.5.

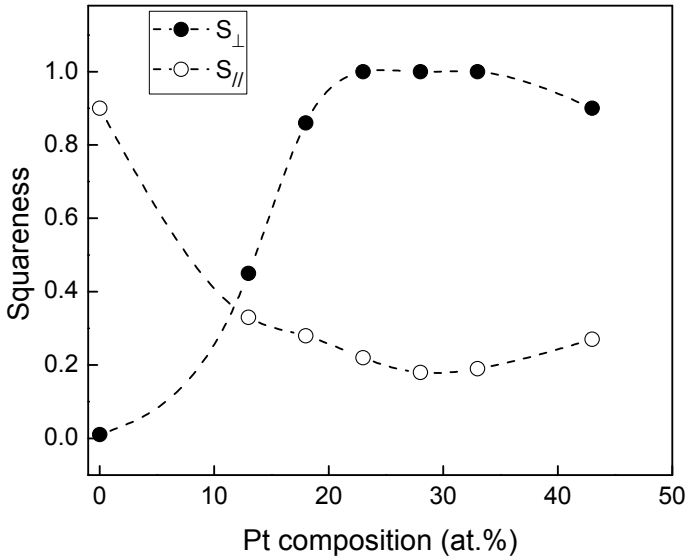

Figure 3.6 Variation of in-plane squareness, $S_{//}$, and out-of-plane squareness, $S_{\perp}$, with Pt compositions in $Co_{100-x}Pt_x$ films deposited on Ru(30 nm)/Pt(2 nm)/Ta(5 nm)/glass.

3.2.3.2 Magnetic anisotropy

In this section, the K_u value of all films is evaluated by taking the area $(\int_0^{M_s} H(M)dM)$ enclosed between magnetization curves of the in-plane and out-of-plane directions as described in section 2.3.3.2. Figure 3.7 shows the variation of K_u with different Pt compositions in $Co_{100-x}Pt_x$ films. The K_u value increased monotonically with increasing the Pt compositions and reached a maximum of 5.5 x 10^6 erg/cc at 28 at.% Pt. This could be explained by the favored growth of the *hcp* CoPt. Since Co (111) and Co (0002) had approximately the same lattice mismatch with Ru underlayer, therefore, the growth of either phase was equally probable, as free energy difference between the *fcc* and *hcp* stacking in nanostructure Co is very small.[96] It is therefore assumed that nanotructured *hcp* and *fcc* CoPt alloys follow the similar trend. The lattice parameter *a* of Ru was 8 % larger than that of Co, which

could induce in-plane tensile strain. This resulted in compressive strain perpendicular to the film plane, and could hinder the growth of Co (0002).[95] Addition of Pt resulted in the lattice expansion of CoPt as observed from the XRD data that Pt addition shifted the Co peak towards a lower momentum transfer. The increased lattice expansion of Co reduced the lattice mismatch with Ru underlayer, promoting the growth of CoPt (0002). However, further increasing the Pt compositions above 28 at.% decreased the K_u value despite reduced lattice mismatch. This warrants further investigation, which is discussed in detail in the next chapter.

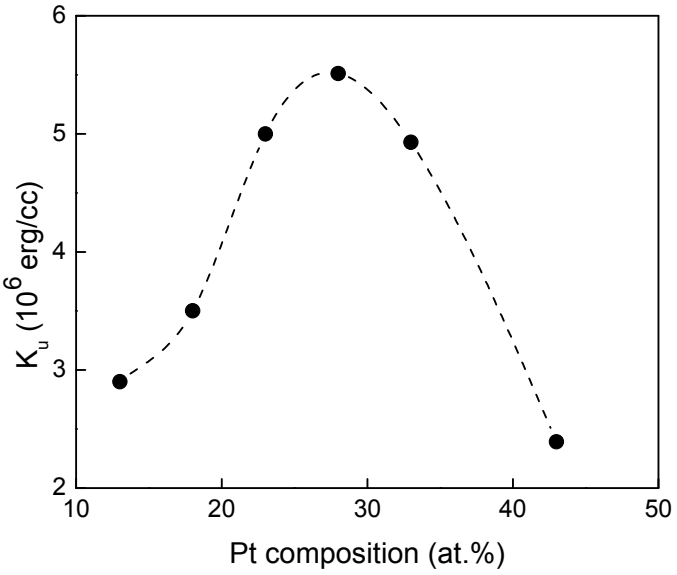

Figure 3.7: Variation of perpendicular magnetic anisotropy constant, K_u, with Pt compositions in $Co_{100-x}Pt_x$ thin films deposited on Ru(30 nm)/Pt(2 nm)/Ta(5 nm)/glass.

3.2.3.3 Coercivity

Figure 3.8 shows the variation of in-plane coercivity, $H_{c//}$, and out-of-plane coercivity, $H_{c\perp}$, with Pt compositions for $Co_{100-x}Pt_x$ films. It showed that $H_{c//}$ and $H_{c\perp}$ of Co_{100} film were the same and equal to 0.1 kOe, indicating its magnetic

softness. With increasing the Pt compositions, no significant change was observed in $H_{c//}$. However, $H_{c\perp}$ continuously increased and reached a maximum of 5.5 kOe for 28 at.% Pt, and decreased thereafter with further increasing the Pt compositions. The variation of $H_{c\perp}$ and K_u showed a similar trend with increasing the Pt compositions. It indicated that the increased values of $H_{c\perp}$ was associated with increased K_u value. In addition to large K_u, the enhancement of $H_{c\perp}$ in the sample with 28 at.% Pt was attributed to a reduced intergranular exchange interaction, which could be observed from the plane-view TEM images as discussed in section 3.2.2.

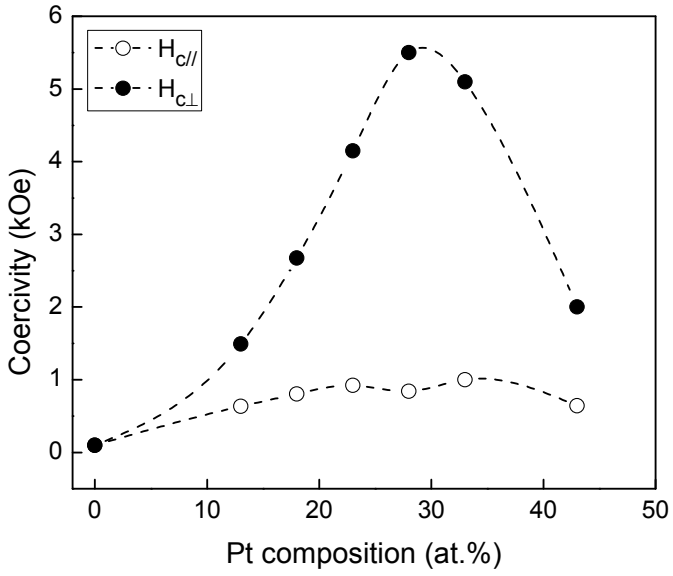

Figure 3.8: Variation of in-plane coercivity, $H_c(//)$, and out-of-plane coercivity, $H_c(\perp)$, with Pt compositions in $Co_{100-x}Pt_x$ thin films deposited on Ru(30 nm)/Pt(2 nm)/Ta(5 nm)/glass.

3.2.3.4 Thermal stability

The ultimate goal of recording industry to use the high K_u materials is to have the thermally stable media so that stored data could be retained for a sufficiently long time. As a result, thermal stability is one of the major concerns in the recording

industry. Therefore, effects of Pt compositions on thermal stability were studied for $Co_{100-x}Pt_x$ films. To measure the thermal stability factor (TSF), the remanent coercivity was measured for applied field duration of 1, 5, 20, 40 and 100 seconds. The data was fitted to the Sharrock's formula given in equation (2.9) for a perpendicular recording media. Figure 3.9(a) illustrates a plot between H_{cr} and $\{\ln(f_0 t)\}^{1/2}$ showing straight line with H_0 as the intercept and $-H_0\{k_BT/K_uV\}^{1/2}$ as slope. All data points in Fig. 3.9(a) lied on the straight lines indicating that Sharrock's formula was a good approximation to measure the TSF**.** The value of TSF was calculated from the y intercept and slope. The values of TSF for different compositions are shown in Fig. 3.9(b). It indicated that TSF increased with Pt compositions and reached a maximum of 805 at 28 at.% Pt. This value was higher by an order of magnitude that required for storing the data for a period of 10 years. The TSF then decreased with further increasing the Pt compositions above 28 at.%. The TSF and K_u showed a similar trend with the Pt compositions indicating a correspondence between TSF and K_u. However, a large TSF could be attributed to a large K_u or/and large magnetic switching volume. In order to investigate the actual cause of high TSF, the magnetic switching volume was also evaluated from remanence coercivity measurement data for different Pt compositions according to equation (2.10) assuming η was unity. The data is plotted in Fig. 3.9(b) along with TSF. It illustrated that magnetic switching volume showed a reverse trend when compared with TSF for different Pt compositions. Hence, it was concluded that the large TSF was not attributed to the large magnetic switching volume; instead it was associated with the large K_u value.

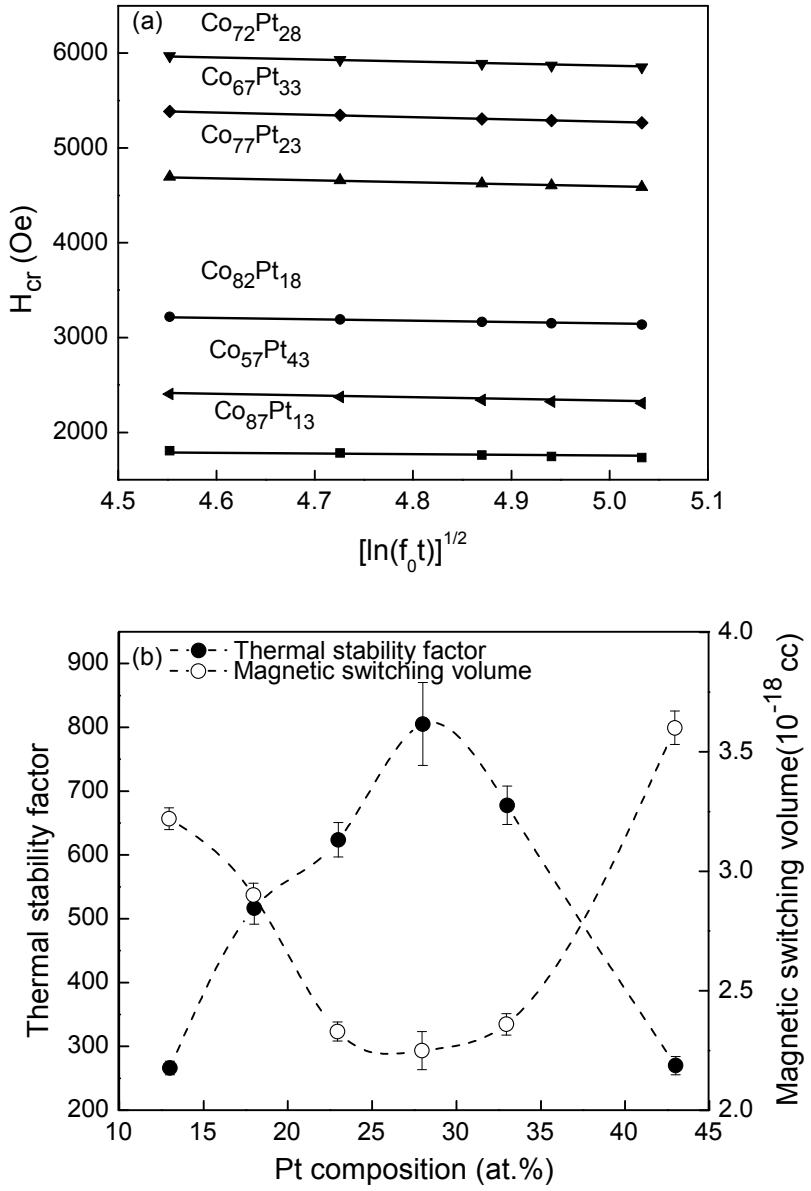

Figure 3.9: (a) A plot of remanent coercivity versus $[\ln(f_0 t)]^{1/2}$. Solid lines are linear fitting of data. (b) Plot of thermal stability factor, $K_u V / k_B T$, and magnetic switching volume for different Pt compositions in $Co_{100-x}Pt_x$ deposited on Ru(30 nm)/Pt(2 nm)/Ta(5 nm)/glass.

3.3 Summary

The effects of Pt compositions on structural and magnetic properties of CoPt were investigated. Alloying Pt with Co reduced the lattice mismatch between the Ru underlayer and Co magnetic layer, and favored the growth of CoPt (0002) on the Ru

(0002) underlayer. The $Co_{72}Pt_{28}$ film was observed to be the optimized alloy composition with large perpendicular magnetic anisotropy, large $H_{c\perp}$, large thermal stability factor and unity out-of-plane squareness.

Chapter 4
Growth induced structural anisotropy and strain analysis in CoPt films

CoPt alloy films have attracted much interest in the magnetic and magneto-optic recording due to their strong perpendicular magnetocrystalline anisotropy (PMA). Conventionally, the materials with large out-of-plane coercivity and squareness compared to that of the in-plane direction are said to have a PMA. Different views were proposed to explain the enhanced PMA in the CoPt films such as growth induced structural anisotropy, [75-77,98,99] reduced c/a value due to lattice deformation,[100] increased c/a value[34] and reduced lattice mismatch between substrate/underlayer and magnetic layer. Some arguments were counterintuitive to each other. However, all arguments depended on the relative compositions of the Co and Pt, and their miscibility with each other. Conventional phase diagram for bulk materials may not necessarily predict the miscibility in nanostructured materials, since it does not consider the surface and interface effects. The conventional phase diagram of $Co_{100-x}Pt_x$ illustrates a complete miscibility at room temperature (Fig. 3.1). However, in nanostructured thin films growth induced structural anisotropy (two dimensional clustering) of Co was reported at temperature larger than 690 K[77]. In growth induced structural anisotropy, the number of Pt atoms surrounding the Co atom was different in the film plane and along the film normal direction (growth direction). In Chapter 3, it was observed that PMA initially increased with increasing the Pt compositions, and decreased with further increasing the Pt compositions above 28 at.%. As a result, it is necessary to understand the origin of PMA in the CoPt thin films. To investigate the origin of PMA, this Chapter emphasized to study three basic issues using polarized EXAFS. First, whether the Co and Pt showed complete

miscibility or formed separate phases. Second, whether Co and Pt were randomly distributed in the lattice or they had any preferential heterogeneity in the growth plane and the growth direction. Third, the strain induced in the CoPt films.

4.1 Experimental methods

The $Co_{100-x}Pt_x$ (50 nm)/Ru (30 nm)/Ta (5 nm)/glass (where x = 0, 10, 28, and 43) films were deposited using magnetron sputtering. All samples were capped with 2 nm Ta to prevent from oxidation. In this set of samples, the Pt intermediate layer was removed and Ta used as a capping layer instead of Pt, as used in Chapter 3. However, these changes did not affect the trend of magnetic properties observed in Chapter 3. Such changes were made to avoid any contribution of the Pt intermediate layer and capping layer in CoPt EXAFS data at the Pt-L_3 edge. Since EXAFS provides the average information of whole sample.

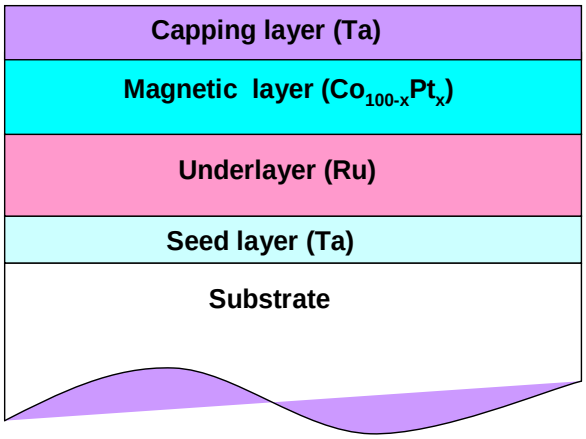

Figure 4.1: Schematic diagram of layers structure.

The schematic diagram of the layers structure is shown in Fig. 4.1. The deposition parameters of different layers were kept the same as described in section

3.1. To study the phase miscibility, growth induced structural anisotropy and strain in the CoPt films, all samples were analyzed using polarized EXAFS at the Co-*K* edge and Pt-L_3 edge. The EXAFS data were collected at Pacific Northwest Consortium-Collaborative Access Team (PNC-CAT) 20 BM beam line of Advanced Photon Source located at Argonne National Laboratory, IL-USA. The details of data collection method have already been discussed in section 2.4.4.3.

4.2 Results and discussion

4.2.1. Magnetic Properties

Figures 4.2(a)-4.2(d) show the in-plane and out-of-plane hysteresis loops of magnetic thin films of $Co_{100-x}Pt_x$. The easy axis of magnetization of Co_{100} lied in the film plane direction, and changed to the out-of-plane direction with increasing the Pt compositions. At 28 at.% Pt, the $S_{//}$ and $S_{\perp}$ were 0.44 and 0.85, respectively, and the $H_{c//}$ and $H_{c\perp}$ were 2.9 kOe and 4.5 kOe, respectively. It showed that the PMA prevailed for 28 at.% Pt composition. With further increasing the Pt compositions, the $S_{\perp}$ and $H_{c\perp}$ decreased significantly indicating deterioration in the PMA.

The in-plane easy axis of magnetization in Co_{100} film could be attributed to the two possible reasons. First, Co_{100} film exhibited *hcp* structure with easy axis (c-axis) along the film normal direction, but shape anisotropy, larger than the magnetocrystalline anisotropy forced the magnetization direction to lie in the film plane. Second, the nanostructure Co_{100} film might acquire the *fcc* structure during the growth process due to small free energy difference between the *hcp* and the *fcc* stacking, though *hcp* Co was stable phase in the bulk. In this study, M_s of the Co_{100}

film was ~ 1000 emu/cc, and associated shape anisotropy, $2\pi M_s^2$, was ~ 6.28 x 10^6 erg/cc, which was larger than the first order magnetocrystalline anisotropy of Co (~ 4.5 x 10^6 erg/cc). Hence, both reasons were equally probable. In order to understand the actual reason of in-plane easy axis of the Co_{100} film and out-of-plane easy axis of the $Co_{100-x}Pt_x$ films, all samples were investigated using XRD and polarized EXAFS.

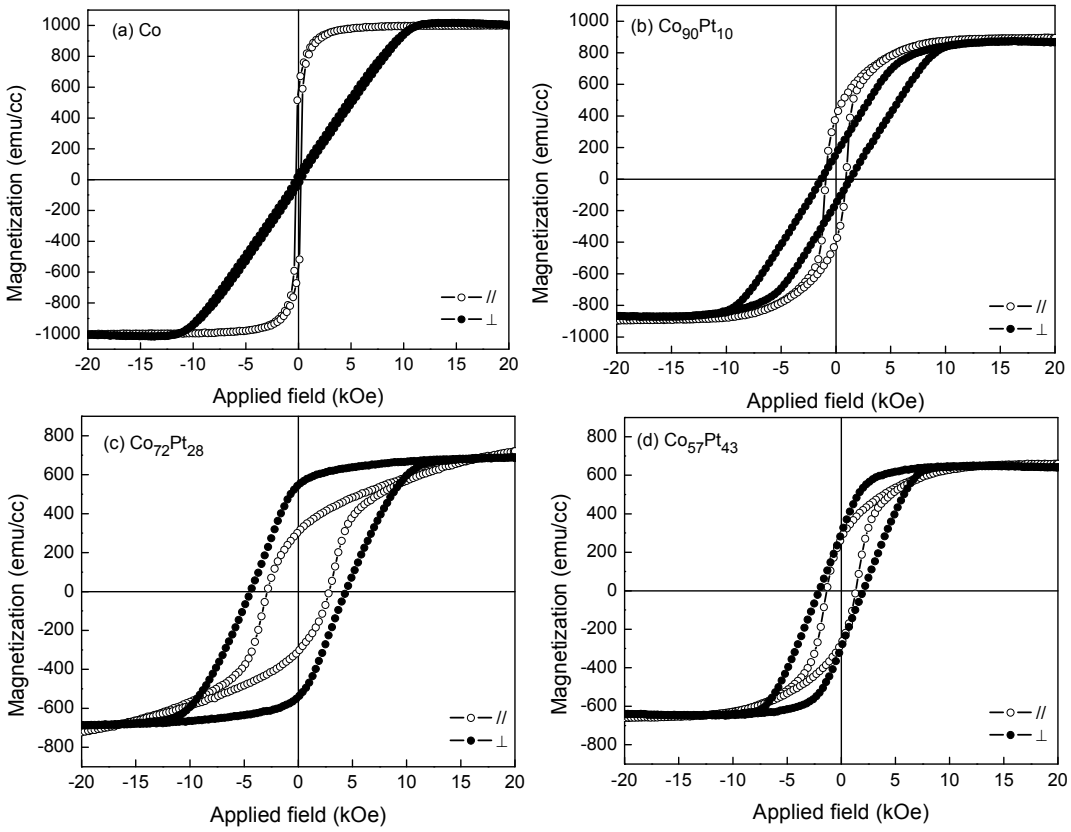

Figure 4.2: In-plane and out-of-plane hysteresis loops of 50 nm thick (a) Co_{100}, (b) $Co_{90}Pt_{10}$, (c) $Co_{72}Pt_{28}$ and (d) $Co_{57}Pt_{43}$ film deposited on Ru(30 nm)/Ta(5 nm)/glass.

4.2.2 Crystallographic structure

Figure 4.3 shows the x-ray powder scans of $Co_{100-x}Pt_x$ films. Similar to the section 3.2.1, the Co_{100} film showed only one peak of magnetic layer corresponding to the momentum transfer (q) of 3.089 $Å^{-1}$. This peak position corresponded to either the

fcc Co (111) or the *hcp* Co (0002), which could not be resolved by XRD. This peak continuously shifted towards a lower q values with increasing the Pt compositions due to the lattice expansion of CoPt. This indicated that the analysis of the XRD data was inconclusive to explain the in-plane easy axis of Co_{100} and the out-of-plane easy axis of $Co_{100-x}Pt_x$. It was observed that increasing film thickness of the $Co_{100-x}Pt_x$ to 50 nm had the advantage over earlier studied samples of 20 nm thickness in Chapter 3, as a thicker magnetic layer showed a larger XRD signal for more accurate analysis. Inset of Fig. 4.3 shows the plot between *d*-spacing of $Co_{100-x}Pt_x$ versus Pt compositions. It showed a linear relationship indicating that the Pt was miscible with Co, and followed the Vegard's law. Assuming the *hcp* symmetry of $Co_{100-x}Pt_x$, the lattice parameter '*c*' of the CoPt was calculated from the (0002) peak. Thereafter, the lattice parameter '*a'* was extracted from the known value of '*c*' assuming the known relation of c/a = 1.633 for bulk. These '*a*' and '*c*' parameters were used to generate the atom input file for the FEFF path calculation in the EXAFS data fitting.

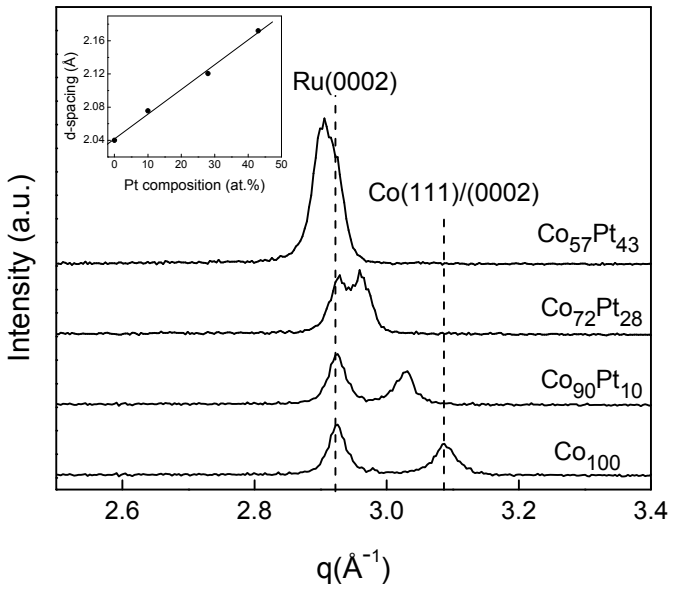

Figure 4.3: X-ray powder scans of Ta(2 nm)/$Co_{100-x}Pt_x$ (50 nm)/Ru(30 nm)/Ta(5 nm)/glass, where x = 0, 10, 28 and 43. Inset shows the plot of interplaner spacing (*d*-spacing) versus Pt compositions for $Co_{100-x}Pt_x$ (0002) peak.

4.2.3 Microstructure

Figures 4.4(a)-4.4(c) show the bright field plane-view TEM images of the $Co_{100-x}Pt_x$ films for different Pt compositions. All films clearly showed the granular structure with grains separated by grain boundaries. The average grain sizes in all samples were approximately 15 nm. However, not all of grains were well isolated from each others and agglomerates of grain were observed. The agglomerates were more isolated from each other in the $Co_{72}Pt_{28}$ compared to the $Co_{90}Pt_{10}$ and $Co_{57}Pt_{43}$.

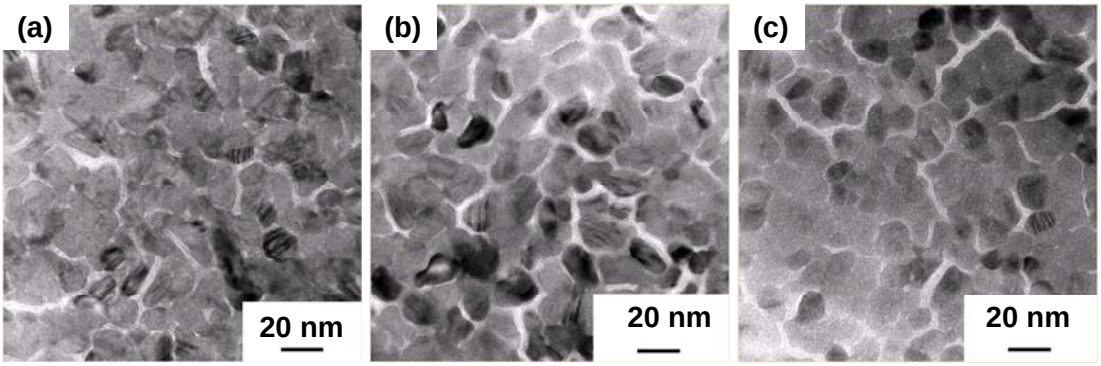

Figure 4.4: Bright field plane-view TEM images of (a) $Co_{90}Pt_{10}$, (b) $Co_{72}Pt_{28}$ and (c) $Co_{57}Pt_{43}$ films deposited on Ru(30 nm)/Ta(2 nm)/glass.

4.2.4 Phase miscibility, growth induced structural anisotropy and strain analysis by polarized EXAFS

4.2.4.1 EXAFS data analysis

All data were analyzed using WinXAS 2.3 code following the standard procedure,[101,102] which determined the structural parameters by fitting the theoretical EXAFS signal to the experimental data. The data analyses were performed in the following order. First, the averaged data was normalized using the two polynomial fit with polynomial order one in the pre-edge region and two in the post edge region. A

smooth atomic background function, $\mu_0(E)$, was removed from the raw absorption coefficient, $\mu(E)$, and normalized EXAFS signal $\chi(k) = (\mu(k) - \mu_0(k))/\Delta\mu_0(0)$ was obtained. The $\Delta\mu_0(0)$ is an absorption edge jump. The reference energy E_0 was taken at the middle of the edge jump[103] and the cubic spline fit was used to remove the non-oscillatory background. Thereafter, χ(k) data was extracted using the spline number 7 and k-weight 2. The extracted data was Fourier transformed in the k-range $2.8 \leq k \leq 13$ for the Co-*K* edge and $3 \leq k \leq 12$ for the Pt-L_3 edge using a Bessel window function. To extract the information about the coordination number, radial distance and Debye-Waller factor, the first peak of Fourier transform (FT) was fitted in a real space (r-space) with theoretically generated FEFF input data. The FEFF 8 code was used to calculate the backscattering amplitude $F_j(k)$ and phase shift $\delta_j(k)$ for each path to the nearest shell of each absorbing atom, namely, the Co-Co and Co-Pt path for the Co central atom and Pt-Pt and Pt-Co path for the Pt central atom. The lattice parameter '*a*' and '*c*' extracted from the XRD data, and P63/mmc space group were used to generate the atom input file for FEFF path calculation. The atom input file for FEFF calculation assumed that the Pt replaced Co in the Co lattice in the first co-ordination shell. The S_0^2 was fixed to 0.7786 and 0.88 during the fitting of Co-*K* edge and Pt-L_3 edge, respectively. These values of S_0^2 were determined by fitting the respective reference foil data measured in the transmission mode under the same experimental conditions as samples were measured. The parameters N, R, σ^2 and ΔE_0 (difference with reference energy E_0) were kept free during fitting the Co-*K* edge. However, during fitting the in-plane data at Pt-L_3 edge, the $R_{Pt\text{-}Co}$ distance was fixed to $R_{Co\text{-}Pt}$ in a respective sample, since relative distance between two atoms always

remained the same with respect to each other. R_{Co-Pt} was extracted by first fitting the in-plane Co-*K* edge data.

4.2.4.2 Polarization dependence XANES analysis of Co film

To confirm the structure of Co_{100}, the Co_{100} film was probed by polarized XANES in the in-plane and out-of-plane polarization geometries at the Co-*K* edge. The experimental in-plane and out-of-plane XANES spectra were compared with respective theoretical spectra generated using FEFF 8 code for the *fcc* and *hcp* Co. Theoretical in-plane and out-of-plane XANES spectra for the *fcc* Co (111) and *hcp* Co (0002) texture film are shown in Fig. 4.5(a). It showed that XANES spectra from the *fcc* structure were independent of polarized x-rays due to isotropic electric-dipole absorption cross-section in the cubic symmetry. In contrast, in the *hcp* structure, absorption spectra exhibited anisotropy due to dichroic dependence of electric-dipole of Co-*K* edge.[104] The XANES spectra from the *hcp* Co show one hump in the out-of-plane polarization geometry and two humps in the in-plane polarization geometry. The position of the hump in the out-of-plane polarization geometry was in between the two humps of the in-plane polarization geometry. Comparing the experimental results for the in-plane and the out-of-plane measurements for Co_{100} film (Fig. 4.5(b)) with that of the theoretical spectra, the film data showed close resemblance with the *fcc* cobalt. This indicated that for Co_{100} film, the *fcc* phase was dominant. This was consistent with reported results[100] that the fraction of *fcc* phase increased with decreasing Pt composition in CoPt film deposited on Ru underlayer. However, the authors in reference 100 did not conduct the test for Co_{100} film.

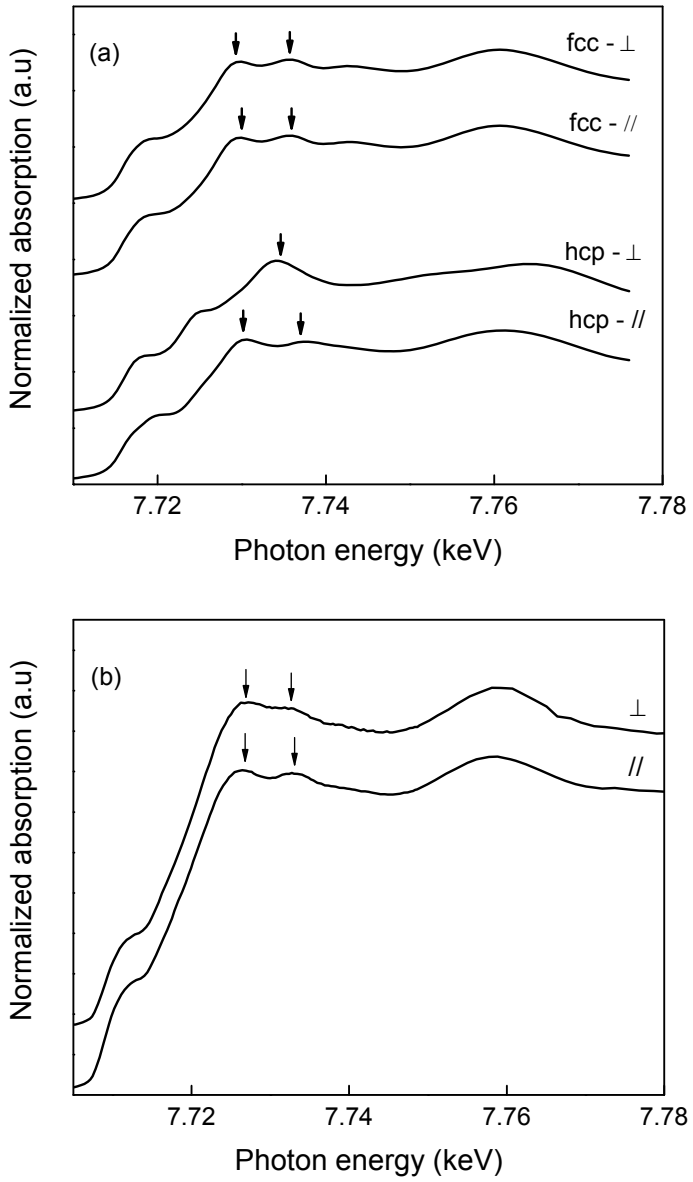

Figure 4.5: (a) Theoretical XANES spectra of *fcc* (111) and *hcp* (0002) textured cobalt films generated by FEFF 8 in the in-plane and out-of-plane polarization geometries. (b) Experimental XANES spectra of Co(50 nm)/Ru(30 nm)/Pt(2 nm)/Ta(5 nm)/Glass, measured at Co-*K* edge in the in-plane and out-of-plane polarization geometries.

4.2.4.3 Polarization dependence EXAFS analysis of Co film

In order to understand the reason behind the *fcc* stacking of the Co_{100} film, the EXAFS data in the in-plane and out-of-plane polarization geometries were Fourier transformed according to the procedure established in section 4.2.4.1. Figure 4.6

shows the FT of the in-plane and out-of-plane polarization geometries. It showed that the maximum of first intense peak of the in-plane polarization geometry was relatively at larger radial distance than that of the out-of-plane polarization geometry. This revealed that film was tensile strained in the in-plane but compressed along the film normal direction.

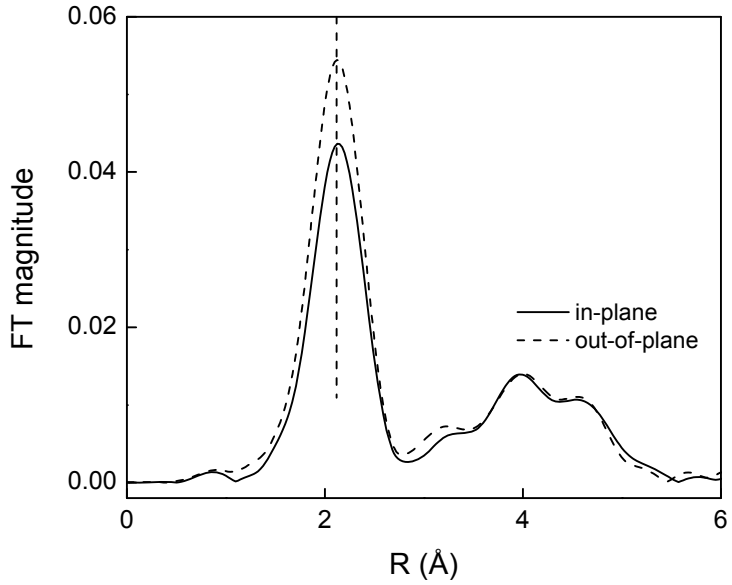

Figure 4.6: Fourier transforms (FT) of the EXAFS spectra of Co_{100} film recorded at Co-*K* edge in the in-plane and out of plane polarization geometries (Phase shift was not corrected). Solid line and dotted line show the in-plane and out-of-plane data, respectively.

Table 4.1: Fitted results (with phase shift correction) of first peak of Fourier transforms at Co-*K* edge in the in-plane and out-of-plane polarization geometries of Co_{100} film. During fitting, the coordination number N was fixed to 12, and S_0^2 was fixed to 0.7786, which was calculated from Co foil data measured in transmission mode. R is the radial distance of first nearest neighbors.

Polarization direction	N	R (Å)
In-plane	12	2.501±0.001
Out-of-plane	12	2.489±0.001

The large in-plane Co-Co distance was attributed to the large lattice parameter '*a*' of Ru underlayer than that of the Co, which induced the in-plane tensile strain in the Co_{100} film. As a result, a compressive strain developed along the film normal direction and reduced the Co-Co bond length in the out-of-plane direction. The first and more intense peak of FT in the r-range of 1.1-2.8 Å was fitted in the r-space. During the fitting of the in-plane and out-of-plane data, the coordination number was fixed to 12. Table 4.1 shows the extracted data. It indicated that the Co-Co distance in the in-plane (2.501 Å) was larger than that of out-of-plane direction (2.489 Å). The large in-plane Co-Co distance induced tensile strain in the film plane. The in-plane tensile strain could hinder the growth of *hcp* Co (0002) and favor the growth of *fcc* Co (111). This suggested that tensile strain induced in the film plane due to Ru underlayer was responsible for the growth of the *fcc* dominating phase in the Co film.

4.2.4.4 Polarization dependence XANES analysis of $Co_{100-x}Pt_x$ films

Figures 4.7(a) and Fig. 4.7(b) show the XANES spectra of the Co-*K* edge measured in the in-plane and out-of-plane polarization geometries, respectively, for $Co_{100-x}Pt_x$. The XANES spectrum of Co reference taken in the transmission mode was plotted with the in-plane and out-of-plane data for comparison. The results showed that all in-plane and out-of-plane spectra measured at Co-*K* edge in the $Co_{100-x}Pt_x$ differed from the Co reference sample indicating that the Co did not segregate as a separate phase. Similarly, Figures 4.8(a) and Fig. 4.8(b) show the XANES spectra of the Pt-L_3 edge measured in the in-plane and out-of-plane polarization geometries, respectively, for $Co_{100-x}Pt_x$ with Pt reference data collected in the transmission mode.

All spectra recorded at Pt-L_3 edge were also different from the Pt reference sample. It revealed that the Pt did not segregate as a separate phase.

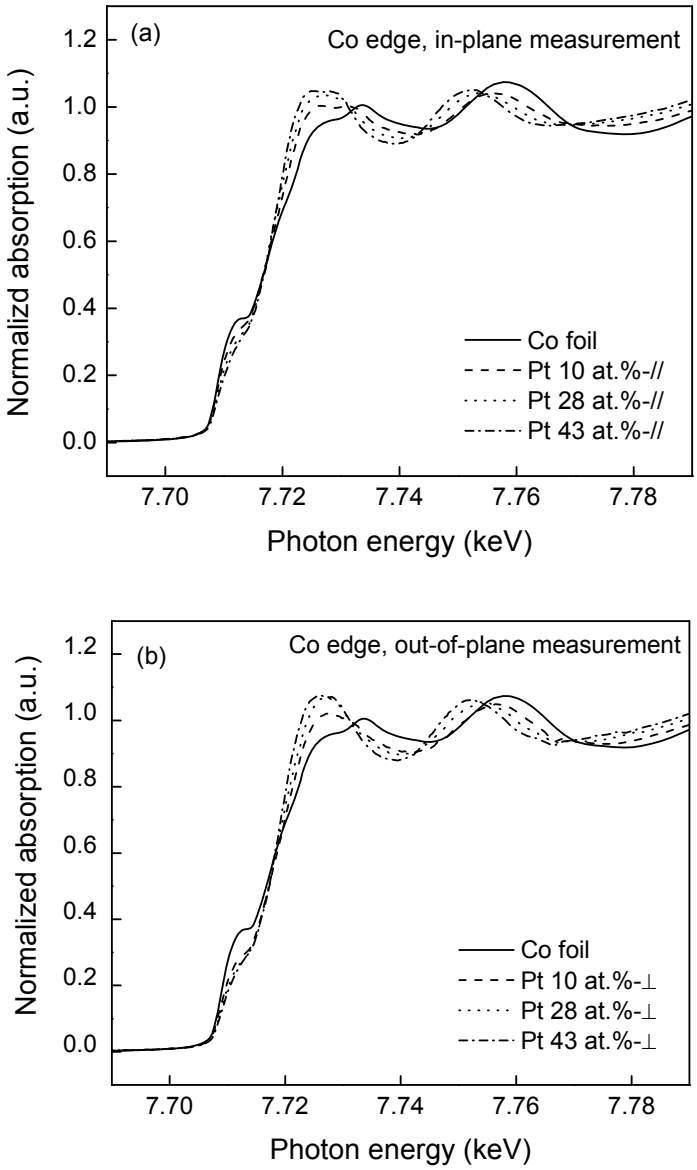

Figure 4.7: XANES spectra of Co-*K* edge for $Co_{100-x}Pt_x$ films measured in the (a) in-plane and (b) out-of-plane polarization geometries, respectively for x = 10, 28 and 43 at.%. The Co foil XANES spectrum measured in the transmission mode was also plotted for comparison.

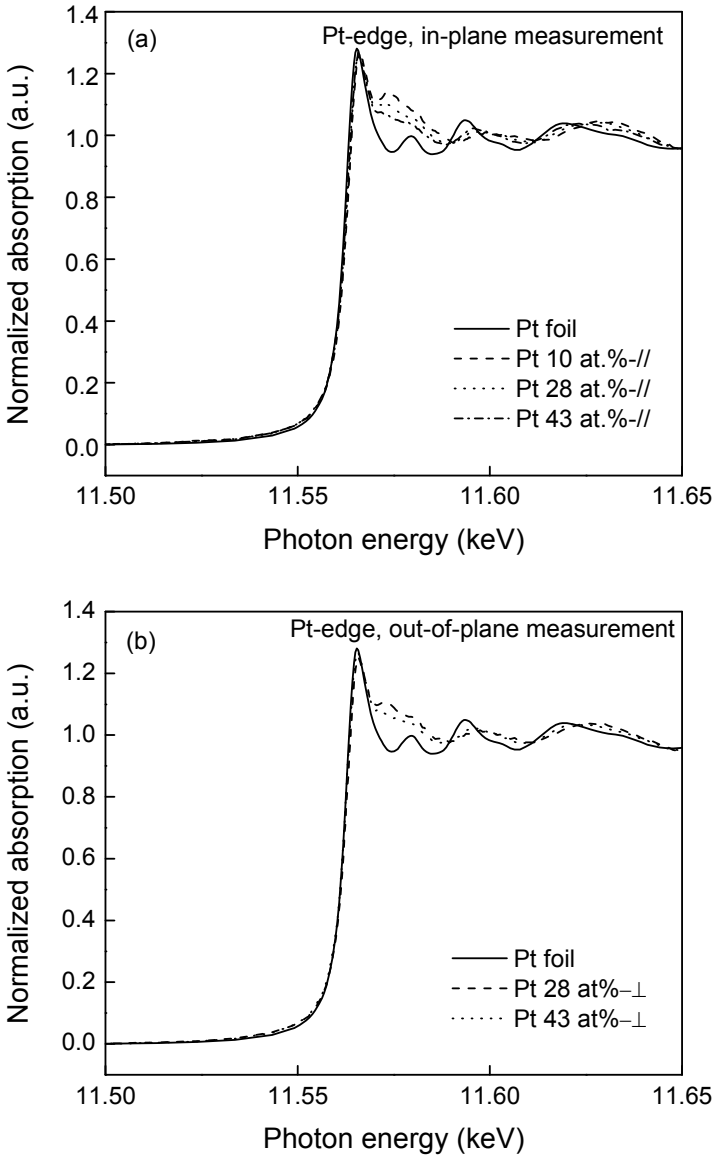

Figure 4.8: XANES spectra of Pt-L_3 edge for $Co_{100-x}Pt_x$ films measured in the (a) in-plane polarization geometry for x = 10, 28 and 43 at.%, and (b) out-of-plane polarization geometry for x = 28 and 43 at.%. The Pt foil XANES spectrum measured in the transmission mode was also plotted for comparison.

In order to study the effects of Pt compositions on phase formation, the in-plane and out-of-plane spectra measured at Co-K edge for different Pt compositions were compared. Figure 4.9(a) - 4.9(c) show the XANES spectra of the Co-*K* edge measured in the in-plane and out-of-plane polarization geometries for 10, 28 and 43 at.% Pt compositions, respectively. It indicated that with increase of Pt compositions,

the difference between the in-plane and out-of-plane spectra increased, showed a maximum for 28 at.% Pt composition and decreased thereafter. These experimental results were compared with the in-plane and out-of-plane spectra generated using FEFF 8 code for the *fcc* phase and *hcp* phase in Fig 4.5(a). It indicated that $Co_{100-x}Pt_x$ film was dominated by *hcp* phase corresponding to 28 at.% Pt compared to 10 and 43 at.% Pt.

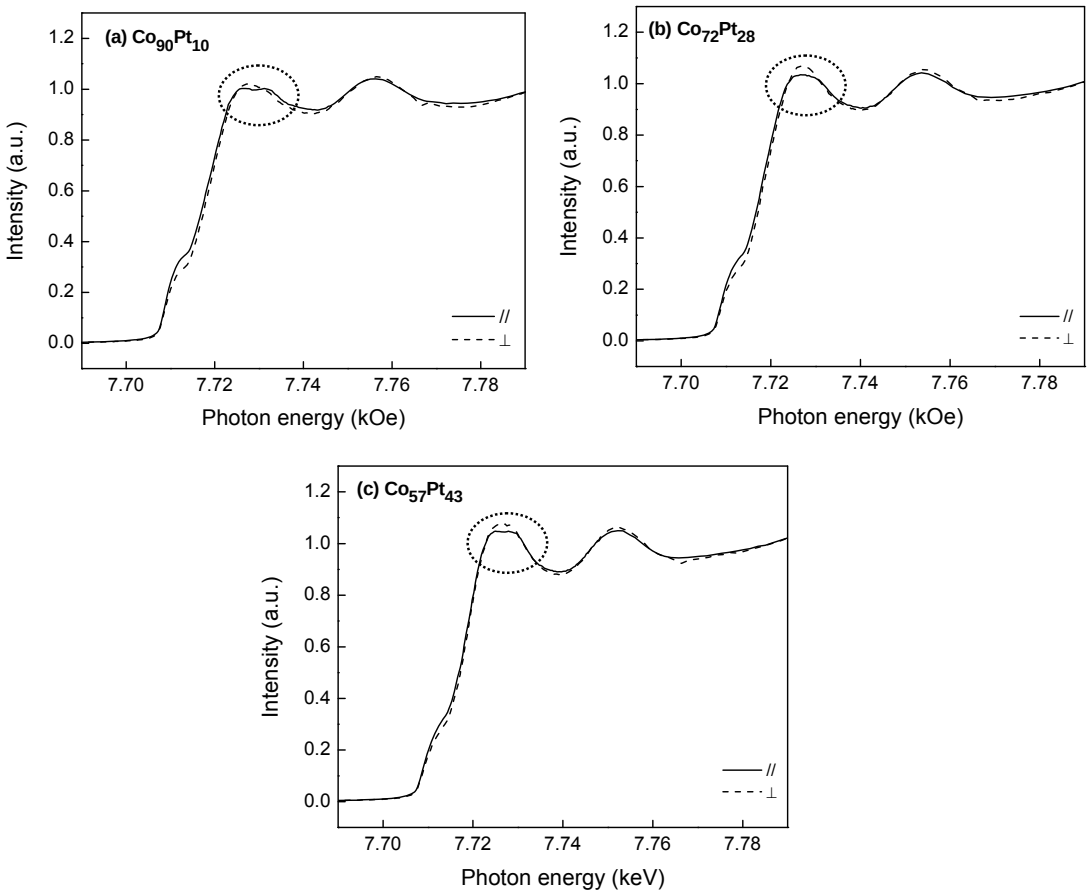

Figure 4.9: XANES spectra of Co-*K* edge for $Co_{100-x}Pt_x$ films measured in the in-plane and out-of-plane polarization geometries for (a) 10, (b) 28 and (c) 43 at.% Pt compositions.

4.2.4.5 Polarization dependence EXAFS analysis of $Co_{100-x}Pt_x$ films

In order to get the information about the phase miscibility and growth induced structural anisotropy, the χ(k) data was extracted from the measured EXAFS signal

and then Fourier transformed according to the procedure established in section 4.2.4.1. Figures 4.10(a)-4.10(c) show the graph of experimental $\chi^2(k)$ data versus photoelectron wavevector measured in the in-plane and out-of-plane polarization geometries at Co-*K* edge for $Co_{90}Pt_{10}$, $Co_{72}Pt_{28}$ and $Co_{57}Pt_{43}$, respectively. The in-plane and out-of-plane spectra of each sample were similar with larger amplitude in the out-of-plane polarization geometry. First and intense peak of FT was fitted in the r-space with model calculation made by FEFF 8 as described in section 4.2.4.1.

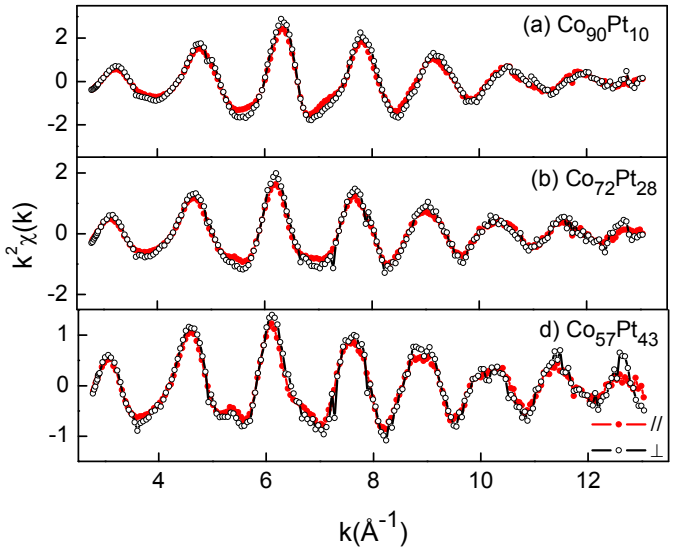

Figure 4.10: The χ^2(k) data collected at Co-*K* edge in the in-plane and the out-of-plane direction for (a) $Co_{90}Pt_{10}$, (b) $Co_{72}Pt_{28}$ and (c) $Co_{57}Pt_{43}$.

4.2.4.5.1 Analysis of phase miscibility in $Co_{100-x}Pt_x$ films

Figures 4.11(a)-4.11(f) show the FT of Co-*K* edge data of the in-plane and out-of-plane polarization geometries for different Pt compositions with best fit of first main peak of the radial distribution function (RDF). In order to check the accuracy of the proposed model, the first intense peak of RDF was back Fourier transformed and fitted with theoretical FEFF data.

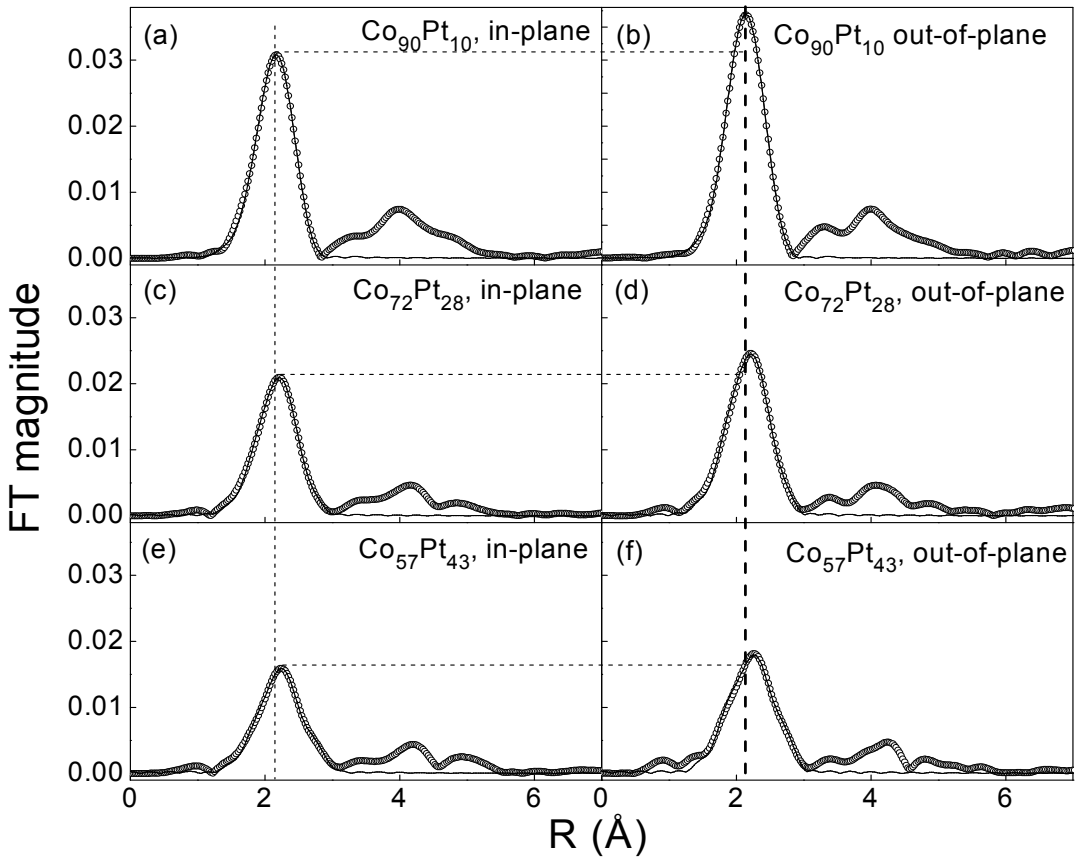

Figure 4.11: Fourier transforms (FT) of experimental data at Co-*K* edge (open symbol) and best fit of first peak of FT (line) for $Co_{100-x}Pt_x$ (50 nm), where x = 10, 28 and 43, in the in-plane and out-of-plane polarization geometries. Phase shift was not corrected.

Figure 4.12(a)-4.12(f) show the back FT data of first peak of Co-*K* edge and computer generated best fit of different samples in the in-plane and out-of-plane polarization geometries. A good fit was observed in all samples in both polarizations geometries, indicating the accuracy of proposed model and fitted results. Two qualitative observations were noteworthy in Fig. 4.11. First, with increasing the Pt compositions, the first peak position shifted towards a higher radial distance for the in-plane and out-of-plane polarization geometries indicating that Pt occupied Co position in the Co lattice, which led to lattice expansion and increased the nearest neighbor distance of Co. These results were consistent with the XRD results, which indicated that

increasing Pt compositions shifted the CoPt peak towards a lower momentum transfer indicating lattice expansion. Second, the magnitude of the FT decreased with increasing the Pt compositions. This was attributed to the increased Co lattice distortion with increasing the Pt compositions, which was associated with larger atomic size of Pt compared to Co.

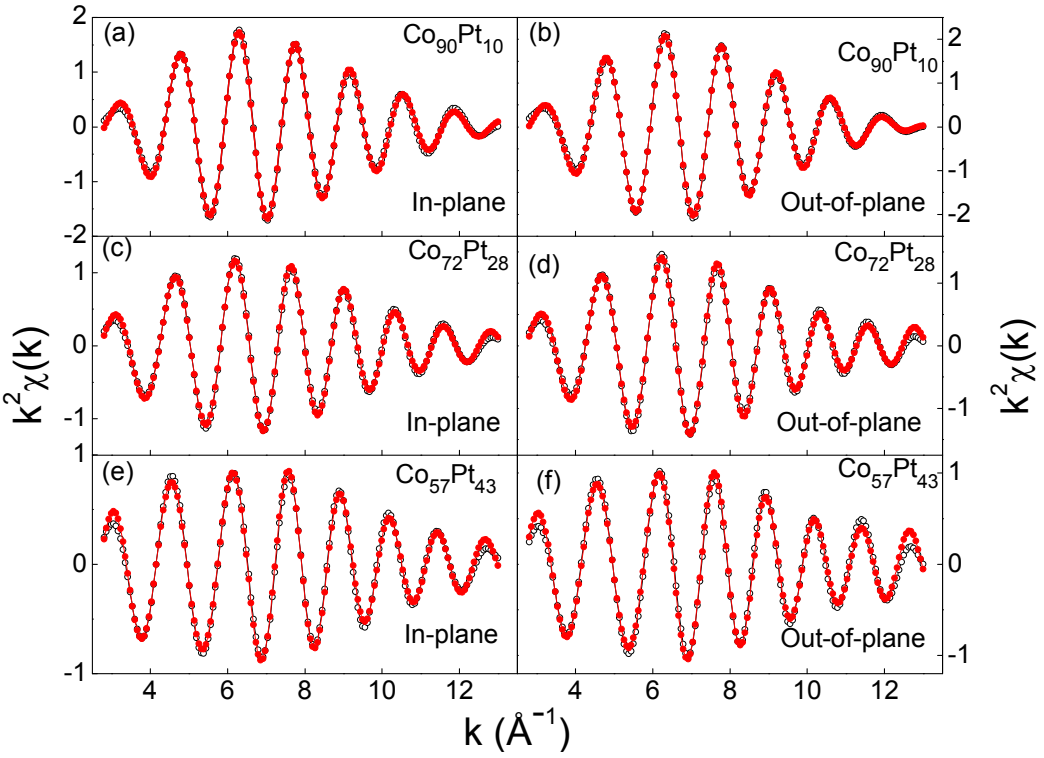

Figure 4.12: Back Fourier transforms (FT) of first peak (open symbol) of FT of experimental data at Co-*K* edge and best fit (solid symbol) for $Co_{100-x}Pt_x$ (50 nm), where x = 10, 28 and 43, in the in-plane and out-of-plane polarization geometries.

The fitting results of the first main peak of Co-*K* edge in the r-space are summarized in Table 4.2. It indicated that with increasing the Pt compositions, the Debye-Waller factor increased in both polarization geometries. This change in Debye-Waller factor indicated that the static displacement of atoms from a mean value increased with increasing the Pt compositions. This result qualitatively agreed with reduced amplitude of first main peak of Co-*K* edge, which was associated with

increased lattice distortion with Pt addition. In order to investigate the intraplanar and interplanar chemical environment of Co in the lattice, the fraction of Co-Co and Co-Pt coordination number in the in-plane and out-of-plane polarization geometries were compared. For example, fraction of Co-Pt coordination number was calculated according to the relation $N_{Co\text{-}Pt}/(N_{Co\text{-}Co}+N_{Co\text{-}Pt})$, where $N_{Co\text{-}Co}$ and $N_{Co\text{-}Pt}$ are number of Co and Pt neighbor atoms around the Co center atom, respectively, and extracted from Table 4.2. The fraction of Co-Co and Co-Pt coordination numbers are summarized in Table 4.3.

Table 4.2: Fitted results (with phase shift correction) of the first peak of Fourier transforms of Co-*K* edge in the in-plane and out-of-plane polarization geometries for $Co_{100-x}Pt_x$. The value of S_0^2 was fixed to 0.7786, which was calculated from Co foil data measured in transmission mode. N, R, and σ^2 represent the coordination number, radial distance of first nearest neighbors and relative mean square deviation, respectively.

Sample	Types of bond	In-plane polarization		Out-of-plane polarization	
$Co_{90}Pt_{10}$	Co-Co	N	9.08±0.01	N	10.30±0.01
		R (Å)	2.523±0.001	R (Å)	2.508±0.001
		σ^2 (Å^2)	0.0088±0.0001	σ^2 (Å^2)	0.0080±0.0001
	Co-Pt	N	0.99±0.01	N	0.71±0.01
		R (Å)	2.590±0.001	R (Å)	2.579±0.001
		σ^2 (Å^2)	0.0023±0.0001	σ^2 (Å^2)	0.0007±0.0001
$Co_{72}Pt_{28}$	Co-Co	N	6.82±0.01	N	8.39±0.01
		R (Å)	2.556±0.001	R (Å)	2.547±0.001
		σ^2(Å^2)	0.0109±0.0001	σ^2 (Å^2)	0.0115±0.0001
	Co-Pt	N	2.62±0.01	N	3.11±0.01
		R (Å)	2.604±0.001	R (Å)	2.607±0.001
		σ^2 (Å^2)	0.0047±0.0001	σ^2 (Å^2)	0.0040±0.0001
$Co_{57}Pt_{43}$	Co-Co	N	4.87±0.01	N	6.91±0.01
		R (Å)	2.598±0.001	R (Å)	2.581±0.001
		σ^2 (Å^2)	0.0123±0.0001	σ^2 (Å^2)	0.0156±0.0001
	Co-Pt	N	4.77±0.01	N	4.71±0.01
		R (Å)	2.631±0.001	R (Å)	2.631±0.001
		σ^2 (Å^2)	0.0069±0.0001	σ^2 (Å^2)	0.0051±0.0001

Table 4.3: Summary of fraction of Co-Co and Co-Pt nearest neighbors around the Co center atom in the two different polarization geometries for $Co_{100-x}Pt_x$ (based on Table 4.2).

Sample	Types of bond	In-plane polarization		Out-of-plane polarization	
		No. of neighbors	% of total neighbors	No. of neighbors	% of total neighbors
$Co_{90}Pt_{10}$	Co-Co	9.08	90.2 %	10.30	93.6 %
	Co-Pt	0.99	9.8 %	0.71	6.4 %
	Total	**10.07**	100 %	**11.01**	100 %
$Co_{72}Pt_{28}$	Co-Co	6.82	72.2 %	8.39	73.0 %
	Co-Pt	2.62	27.8 %	3.11	27.0 %
	Total	**9.44**	100 %	**11.5**	100 %
$Co_{57}Pt_{43}$	Co-Co	4.87	50.5 %	6.91	59.5 %
	Co-Pt	4.77	49.5 %	4.71	40.5 %
	Total	**9.64**	100 %	**11.62**	100 %

Table 4.3 indicated that the fraction of Co-Pt coordination number for the in-plane and out-of-plane polarization geometries were the same, and equal to the global Pt composition for $Co_{72}Pt_{28}$ film within the limit of experimental uncertainties. It suggested that the Pt was completely miscible in the Co. Similar chemical environments of Co in the in-plane and out-of-plane polarization geometries indicated that Pt was randomly distributed in the Co lattice suggesting the absence of growth induced structural anisotropy for $Co_{72}Pt_{28}$. However, for the $Co_{90}Pt_{10}$ and $Co_{57}Pt_{43,}$ the fraction of Co-Pt coordination number in the in-plane and out-of-plane polarization geometries were significantly different. For $Co_{90}Pt_{10,}$ the fraction of Co-Pt coordination number in the in-plane and the out-of-plane polarization geometries were 9.8% and 6.4%, respectively, whereas for $Co_{57}Pt_{43}$, the Co-Pt coordination number in the in-plane and the out-of-plane polarization geometries were 49.5% and 40.5%, respectively. This suggested that the Co was surrounded by more Pt in the film plane

than that of the out-of-plane direction for $Co_{90}Pt_{10}$ and $Co_{57}Pt_{43.}$ It indicated growth induced structural anisotropy for $Co_{90}Pt_{10}$ and $Co_{57}Pt_{43.}$

The comparison between total coordination number ($N_{Co-Co}+N_{Co-Pt}$) in the in-plane and the out-of-plane polarization geometries indicated that the total coordination number in the out-of-plane polarization geometry was larger than that of the in-plane polarization geometry. Furthermore, FT amplitude was larger in the out-of-plane polarization geometry compared to the in-plane polarization geometry. Since, in the hexagonal structure with (0002) preferred orientation, 75% of coordination number were determined by the in-plane neighbors for in-plane polarization geometry. Hence, presence of grain boundaries significantly reduced the coordination number for the in-plane polarization geometry. The EXAFS provides average atomic information of grain and grain boundaries, and it is widely accepted that coordination numbers of atoms in the grain boundaries are significantly smaller than that of grains. This suggested that reduced average coordination number for the in-plane polarization geometry could be attributed to the presence of grain boundaries, which also reduced the FT magnitude. It could be observed from the TEM images shown in Fig. 4.4 that all samples exhibited significant amount of grain boundaries. In the out-of-plane direction the presence of grain boundaries could not affect the coordination number because it is only determined by the atoms situated along the growth direction rather than the growth plane. This indicated that presence of grain boundaries were responsible for the reduced co-ordination number and FT magnitude in the in-plane polarization geometry compared to the out-of-plane polarization geometry. These results suggested that the growth in the film normal direction was quite well structured, as expected from columnar growth.

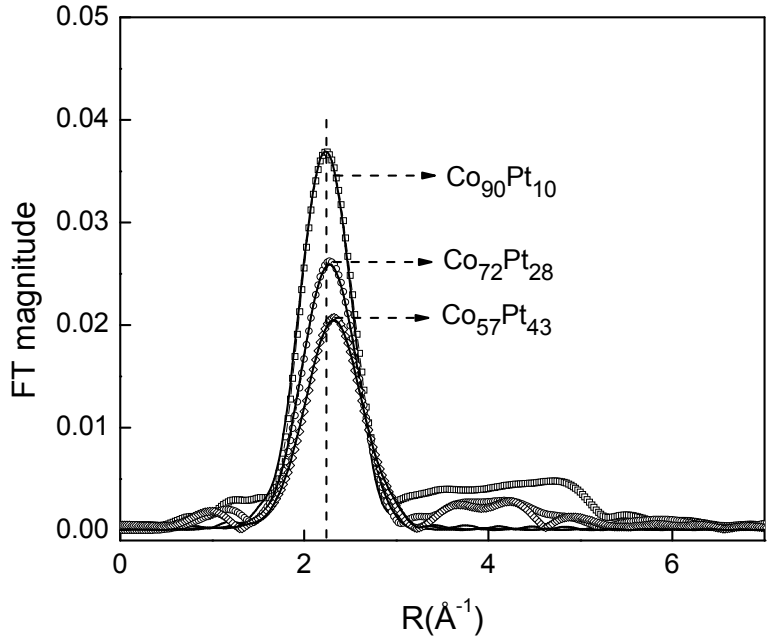

Figure 4.13: Fourier transforms (FT) of experimental data at Pt-L_3 edge (open symbol) and best fit of first peak of FT (line) for $Co_{100-x}Pt_x$ (50 nm), where x = 10, 28 and 43, in the in-plane polarization geometry. Phase shift was not corrected.

Figure 4.13 shows the FT of data collected at Pt-L_3 edge for $Co_{100-x}Pt_x$ in the in-plane polarization geometry for different Pt compositions. The fitting results of the in-plane data taken at the Pt-L_3 for different samples are tabulated in Table 4.4. The possibility of Pt-Pt bonds in the $Co_{90}Pt_{10}$ was not observed. These results were also consistent with the results extracted at Co-*K* edge, where fraction of Co-Pt bond was detected to ~9.4 % indicating that Pt was completely surrounded by Co. The fraction of Pt-Pt bond in the $Co_{72}Pt_{28}$ was in proportion to its global composition. However, the fraction of Pt-Pt bonds in $Co_{57}Pt_{43}$ was larger than that of its global composition. Due to the lack of out-of-plane data at the Pt-L_3 edge, a direct comparison was not possible at the Pt-L_3 edge. However, comparison of the in-plane and the out-of-plane data at Co-*K* edge and the in-plane data at Pt-L_3 edge suggested that growth induced structural anisotropy was detected in the $Co_{90}Pt_{10}$ and $Co_{57}Pt_{43}$ films, but absent in the $Co_{72}Pt_{28}$.

Table 4.4: Fitted results (with phase shift correction) of the first peak of Fourier transforms at Pt-L_3 edge in the in-plane polarization geometry for $Co_{100-x}Pt_x$. The value of S_0^2 was fixed to 0.88, which was calculated from Pt foil data measured in transmission mode. N, R, and σ^2 represent the coordination number, radial distance of first nearest neighbors and relative mean square deviation, respectively.

Sample	Pt-L_3 - edge	In plane polarization	
$Co_{90}Pt_{10}$	Pt-Pt	N	-
		R (Å)	-
		σ^2(Å^2)	-
	Co-Pt	N	10.20±0.01
		R (Å)	2.580
		σ^2(Å^2)	0.0054±0.0001
$Co_{72}Pt_{28}$	Pt-Pt	N	2.33±0.01
		R (Å)	2.700±0.001
		σ^2(Å^2)	0.0030±0.0001
	Co-Pt	N	7.14±0.01
		R (Å)	2.600
		σ^2(Å^2)	0.0063±0.0001
$Co_{57}Pt_{43}$	Pt-Pt	N	4.54±0.01
		R (Å)	2.712±0.0001
		σ^2(Å^2)	0.0046±0.0001
	Co-Pt	N	4.66±0.01
		R (Å)	2.631
		σ^2(Å^2)	0.0063±0.0001

4.2.4.5.2 Strain analysis in $Co_{100-x}Pt_x$ films

In order to investigate the strain induced in CoPt film, Co nearest neighbor distance in the in-plane and out-of-plane polarization geometries were analyzed. Table 4.2 illustrated that the Co-Co and Co-Pt neighbors distance were approximately the same for the in-plane and out-of-plane polarization geometries for $Co_{72}Pt_{28}$. It ruled out the existence of strain in the $Co_{72}Pt_{28}$ film. However, the Co-Co and Co-Pt nearest neighbor distance in the in-plane were significantly larger than that of the out-of-plane for $Co_{90}Pt_{10}$, indicating that film was tensile strained in the film plane and

compressed along the film normal direction. Large Co-Pt distance in the film plane compared to the out-of-plane direction was attributed to the tensile strain induced by the Ru underlayer, while the large Co-Co distance could be associated to the combined effects of strain induced by Ru and lattice distortion induced due to more Pt in the film plane. In $Co_{57}Pt_{43}$, the Co-Pt distance was the same in both polarization geometries indicating that large lattice parameter '*a*' of Ru did not significantly contribute to the tensile strain in the film plane. Assume the *hcp* structure of $Co_{57}Pt_{43}$, the lattice parameter '*a*' was calculated to 2.62 Å, according to Vegard's law. As a result, the lattice mismatch between the Ru underlayer and $Co_{57}Pt_{43}$ reduced to +3%, which could be relaxed over the film thickness as the film could be considered as an elastic continuum. The lattice mismatch, ε, was calculated according to the relation $\varepsilon = (a_{Ru} - a_{CoPt}) / a_{CoPt}$. If $Co_{57}Pt_{43}$ was an *fcc*, the same lattice mismatch would occur between the Ru (0002) texture plane and CoPt (111) texture plane in the film plane. Since EXAFS provides average information of sample, therefore it is obvious that the effects of such a small lattice mismatch cannot be observed. However, the Co-Co neighbor distance in the in-plane geometry was larger than that of the out-of-plane geometry by 0.017 Å. The large Co-Co distance was associated with larger Pt in the film plane. The average interatomic distance for different Pt compositions were calculated according to the method established in Appendix A. The average interatomic distance in the in-plane polarization geometry was 2.530, 2.569 and 2.614 Å and that of out-of-plane polarization geometry was 2.513, 2.563 and 2.601 Å, respectively, for 10, 28 and 43 at.% Pt compositions. Thus in-plane tensile strain was observed for $Co_{90}Pt_{10}$ and $Co_{57}Pt_{43}$. The in-plane tensile strain could hinder the growth of *hcp* (0002) stacking and favored the growth of *fcc* (111) along the growth direction. As a result, the $Co_{90}Pt_{10}$ and $Co_{57}Pt_{43}$ may have a mixture of the

fcc and *hcp* phases. However, the film corresponding to 28 at.% Pt was relaxed and dominated by the *hcp* phase with c/a ratio 1.627 (detail calculation is shown in Appendix A). The favored growth of *hcp* phase assisted to achieve large PMA in the $Co_{72}Pt_{28}$. It was consistent with the XANES and magnetic data.

4.3 Summary

The Co_{100} film deposited on Ru (0002) underlayer exhibited the *fcc* dominant phase with Co (111) preferred orientation and showed the in-plane easy axis of magnetization. This was attributed to the in-plane tensile strain induced in the Co_{100} film due to larger lattice parameter *a* of Ru than that of the Co. Addition of Pt in Co reduced the lattice mismatch with Ru underlayer and improved the magnetic properties. The easy axis of magnetization changed from in-plane to the out-of-plane for $Co_{72}Pt_{28.}$ It was observed that the Co and Pt showed complete miscibility in the range of studied compositions. However, it exhibited growth induced structural anisotropy in $Co_{90}Pt_{10}$ and $Co_{57}Pt_{43}$, and indicated that Co was surrounded by more Pt in the film plane direction compared to the out-of-plane direction. The average interatomic distance in the in-plane polarization geometry was larger than that of the out-of-plane polarization geometry for the $Co_{90}Pt_{10}$ and $Co_{57}Pt_{43}$ films. These results supported the in-plane tensile strain. However, in $Co_{72}Pt_{28}$ film, Pt randomly distributed in the Co lattice and average interatomic distance in the in-plane and the out-of-plane polarization geometries were approximately the same indicating absence of tensile strain in the film plane. The absence of in-plane tensile strain in the $Co_{72}Pt_{28}$ favored the growth of (0002) texture. The increased K_u value in the $Co_{72}Pt_{28}$ film could be attributed to improved *hcp* stacking.

Chapter 5
Effects of CoPt film thickness on microstructural evolution and magnetization reversal mechanism

High thermal stability and large *SNR* are the critical issues for Co-based alloy perpendicular recording media. As discussed in section 1.1.1 that high thermal stability is determined by large K_u and/or large magnetic switching volume. Magnetization reversal of recording media plays a very significant role in determining the *SNR* and hence the media performance. To achieve large SNR in recording media, the grains are supposed to reverse their magnetization coherently. In this case the magnetic switching volume is the same as the physical particle volume observed from TEM, even the particle may consists of many grains in its volume. Increasing film thickness increased the thermal stability factor due to increased magnetic switching volume. However, the magnetization reversal mechanism deviated from coherent to incoherent behavior and deteriorated the SNR value.

Magnetization reversal mechanisms of particles depend on their size[105] and lateral magnetic interaction between them.[106] Particle above a critical size exhibits incoherent magnetization reversal. Large lateral magnetic interaction increases the effective particle volume and favors the incoherent magnetization reversal. Wu et al.[107] reported a transition from coherent to incoherent magnetization reversal in CoPt-oxide media for film thicker than 21 nm. However, Jung et al.[106] observed that magnetization reversal showed incoherent magnetization reversal caused by domain wall motion for thickness less than 6 nm, which deviated toward coherent switching and followed the S-W model when thickness increased above 6 nm in CoCrPt-SiO_2 media. The incoherent switching at small thickness was associated with highly exchange-coupled initial layer. Despite the study of magnetization reversal

mechanism for different thickness, the underlying physical mechanisms are yet to be completely understood. Therefore, in this chapter detailed microstructural investigation of CoPt film with different film thickness was carried out. Attempts were made to correlate the change in magnetization reversal mechanism with microstructure of the films. In chapter 3, it was observed that $Co_{72}Pt_{28}$ film exhibited large K_u, as a result, in this chapter $Co_{72}Pt_{28}$ film was chosen to investigate the thickness effects.

5.1 Experimental methods

The schematic diagram of layer structure was kept the same as described in Fig. 3.2. Pt(2 nm)/$Co_{72}Pt_{28}$(x nm)/Ru(30 nm)/Pt(2 nm)/Ta(5 nm)/glass (x = 5, 10, 20, 40 and 80 nm) films were deposited by magnetron sputtering. All the deposition parameters were also kept the same as described in section 3.1.

5.2 Results and discussion

5.2.1 Crystallographic structure

Figure 5.1 shows the x-ray powder scans of samples with different $Co_{72}Pt_{28}$ film thickness. For small thickness of $Co_{72}Pt_{28}$, the $Co_{72}Pt_{28}$ (0002) peak could not be identified as a separate peak from the Ru (0002). The Ru (0002) peak became more asymmetrical towards a higher momentum transfer with increasing $Co_{72}Pt_{28}$ thickness. At the $Co_{72}Pt_{28}$ thickness of 40 nm and above the $Co_{72}Pt_{28}$ (0002) peak existed as a separate peak corresponding to the momentum transfer of 2.961 $Å^{-1}$.

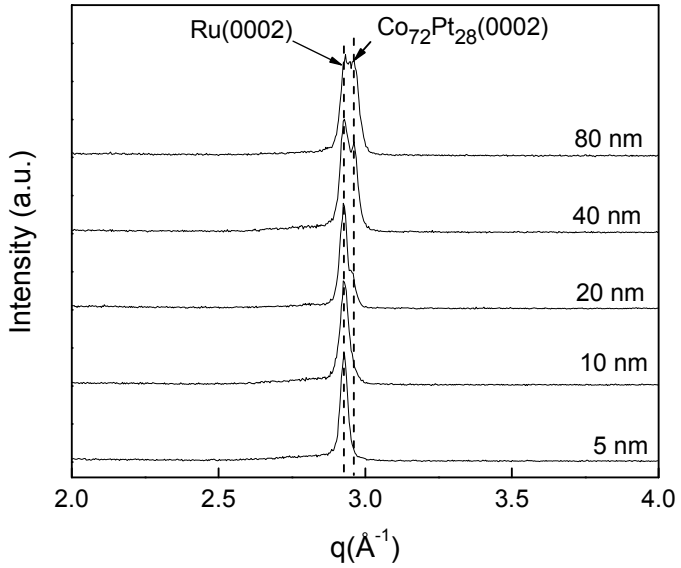

Figure 5.1: X-ray powder scans of different $Co_{72}Pt_{28}$ films thickness deposited on Ru(30 nm)/Pt(2 nm)/Ta(5 nm)/glass.

5.2.2 Microstructure

Figures 5.2(a)-5.2(c) show the bright field plane-view TEM images of films with thickness of 10 nm, 20 nm and 80 nm, respectively. It was observed that the grains in 10 nm film were strongly connected with each other with average grain diameter of 12.0±2.0 nm. The grains in 20 nm film showed more grain isolation compared to 10 nm (as observed from the bright contrast of voided boundaries) with average grains diameter of 9.0±1.7 nm. With further increase of $Co_{72}Pt_{28}$ thickness to 80 nm, the grain diameter further increased. It was observed that ~3-4 small grains were agglomerated and formed particle. Figures 5.3(a) and 5.3(b) show the cross-section images for 20 nm and 80 nm $Co_{72}Pt_{28}$ films, respectively. Figure 5.3(a) showed that in the initial stage of growth the film was rather continuous, whereas in the later stage more pronounced isolated dome-shaped columnar structure was observed. It indicated increased grain isolation in the 20 nm film. In Fig. 5.3(b) it was observed that after certain thickness, the grains started to grow in the inverted frustum

shape (i.e grains diameter started to increase with thickness). Such type of microstructural evolution may be understood on the basis of minimization of surface energy. The growth of surface with smallest surface energy is always favored compared to the other possible crystallographic facet. In *hcp* CoPt alloy, (0002) face has minimum surface energy. In this experiment, it was observed from the x-ray powder scans that all films showed (0002) texture with c-axis along the film normal. It indicated that $Co_{72}Pt_{28}$ (0002) plane lied in the film plane. As a result, to minimize the surface energy, the column width increased when thickness exceeded a certain critical value and reduced the grain isolation.

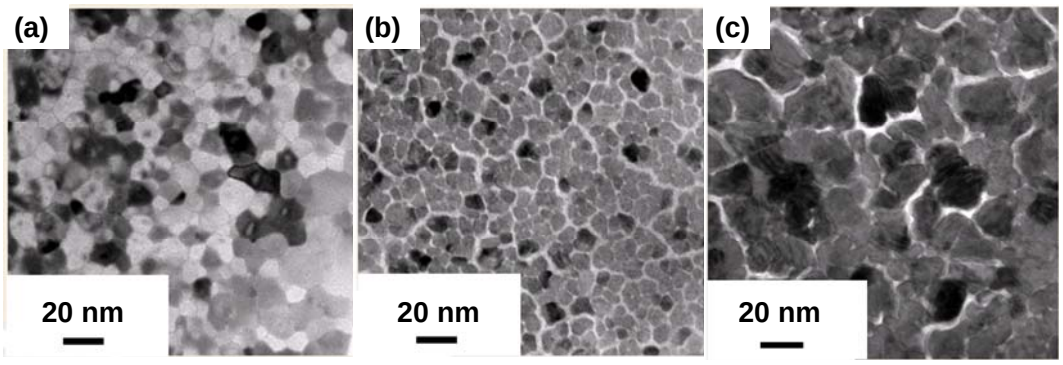

Figure 5.2: Plane-view bright field TEM images of (a) 10 nm, (b) 20 nm and (c) 80 nm $Co_{72}Pt_{28}$ films deposited on Ru(30 nm)/Pt(2 nm)/Ta(5 nm)/glass.

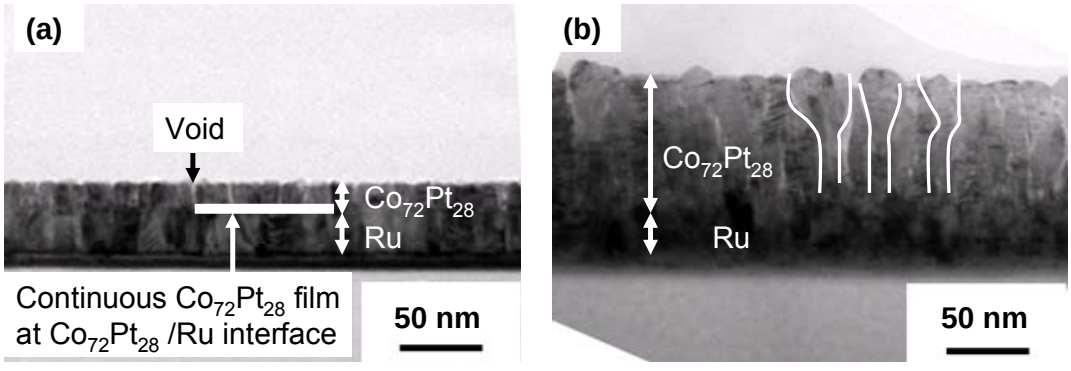

Figure 5.3: Cross-section bright field TEM images of (a) 20 nm and (b) 80 nm $Co_{72}Pt_{28}$ thin films deposited on Ru(30 nm)/Pt(2 nm)/Ta(5 nm)/glass.

5.2.3 Magnetic properties

5.2.3.1 Hysteresis loops

Figures 5.4(a)-5.4(d) show the in-plane and out-of-plane hysteresis loops of selected samples of different $Co_{72}Pt_{28}$ film thickness. A sudden drop at zero applied field was observed in the out-of-plane hysteresis loop for 10 nm $Co_{72}Pt_{28}$ film in Fig. 4(a) indicating a two phase system of different magnetic anisotropy. This could be attributed to a low anisotropy of $Co_{72}Pt_{28}$ film in initial layer, since low anisotropy in Co-based alloy has been reported in initial layer.[108]

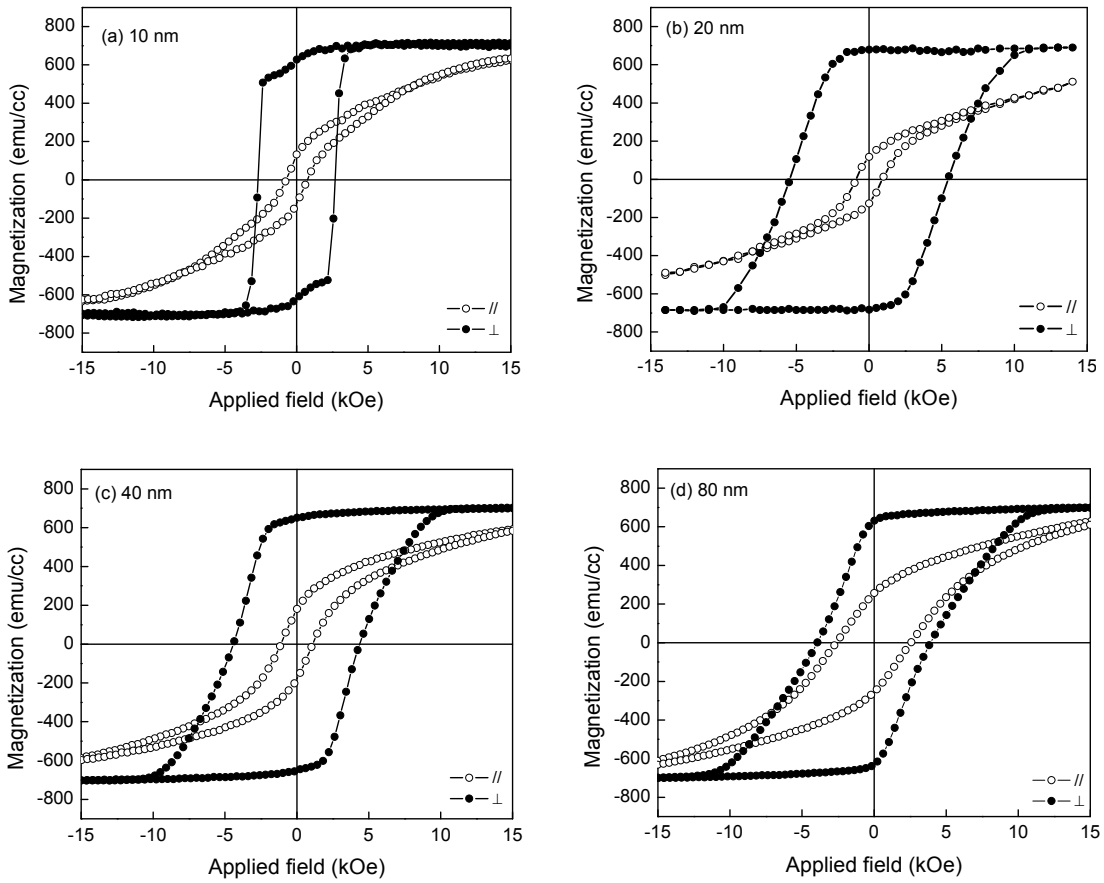

Figure 5.4: In-plane and out-of-plane hysteresis loops of $Co_{72}Pt_{28}$ of different thickness; (a) 10 nm, (b) 20 nm, (c) 40 nm and (d) 80 nm deposited on Ru(30 nm)/Pt(2 nm)/Ta(5 nm)/glass.

The coercivity and squareness were extracted from the hysteresis loops. Figure 5.5(a) and Fig. 5.5(b) show the variation of coercivity and squareness with increasing $Co_{72}Pt_{28}$ films thickness, respectively. The $H_{c\perp}$ monotonically increased from 0.8 kOe to 5.5 kOe with increasing the $Co_{72}Pt_{28}$ film thickness from 5 nm to 20 nm, and decreased thereafter to 4.0 kOe when the film thickness increased to 80 nm (Fig. 5.5(a)). The $H_{c//}$ did not change significantly with increasing film thickness. The thickness dependence of in-plane and out-of-plane squareness (Fig. 5.5(b)) showed similar trend with corresponding coercivity. The out-of-plane coercivity and squareness were larger than that of corresponding value in the in-plane, indicating that perpendicular magnetic anisotropy prevailed in all samples. It is consistent with the XRD results shown in Fig. 5.1, where all film exhibited the (0002) texture.

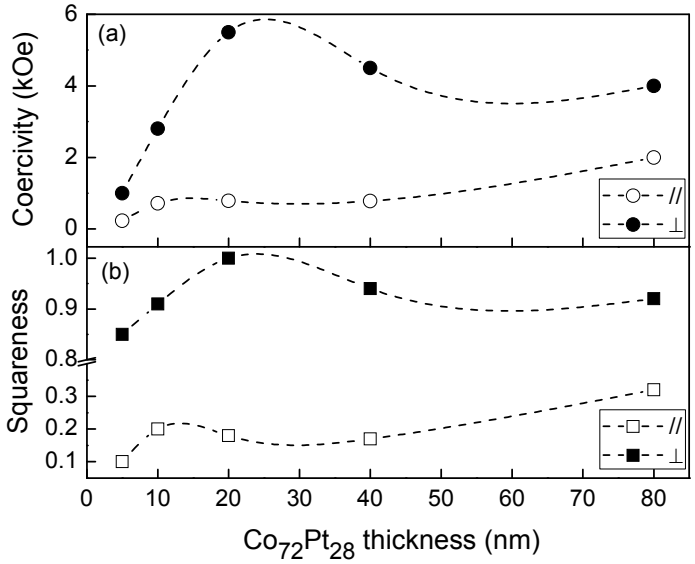

Figure 5.5: In-plane (//) and out-of-plane (⊥) (a) coercivity and (b) squareness of $Co_{72}Pt_{28}$ films of different thickness deposited on Ru(30 nm)/Pt(2 nm)/Ta(5 nm)/glass.

5.2.3.2 Magnetization reversal mechanism

The angular dependence of coercivity and remanent coercivity can be used to qualitatively analyze the magnetization reversal mechanism. Therefore, in order to investigate the magnetization reversal mechanism, the angular dependence coercivity and remanent coercivity of all samples of different $Co_{72}Pt_{28}$ film thickness were measured and normalized to the respective coercivity and remanent coercivity at $\theta = 0^o$, where θ is the angle between the film normal (easy axis) and the applied field direction. Figure 5.6(a) shows the normalized coercivity as a function of θ. The theoretical curves for the S-W model of a single domain particle defined by equation (2.4) and (2.5), and domain wall motion defined by equation (2.6), were also plotted for comparison. It was observed that the normalized coercivity of film of 5 nm thickness gradually increased with increasing θ to 70°, and suddenly decreased when the θ approached 80°. This indicated that magnetization reversal mechanism of this film neither followed the S-W model nor the domain wall motion due to the obvious lack of agreement between the experimental and the theoretical curves. However, a qualitative comparison suggested a closer resemblance to the domain wall motion when compared with the S-W model. With increasing the thickness to 20 nm, the magnetization reversal of film approached the S-W model, since the normalized coercivity reduced significantly with increasing field angle (θ) to the whole range of measurement. However, with further increasing thickness above 20 nm, the magnetization reversal mechanism deviated from the S-W model. It is well known that magnetization reversal by the S-W model was applied to the magnetically non-interacting grains. Any intergranular magnetic interaction led to a deviation from the ideal behavior.

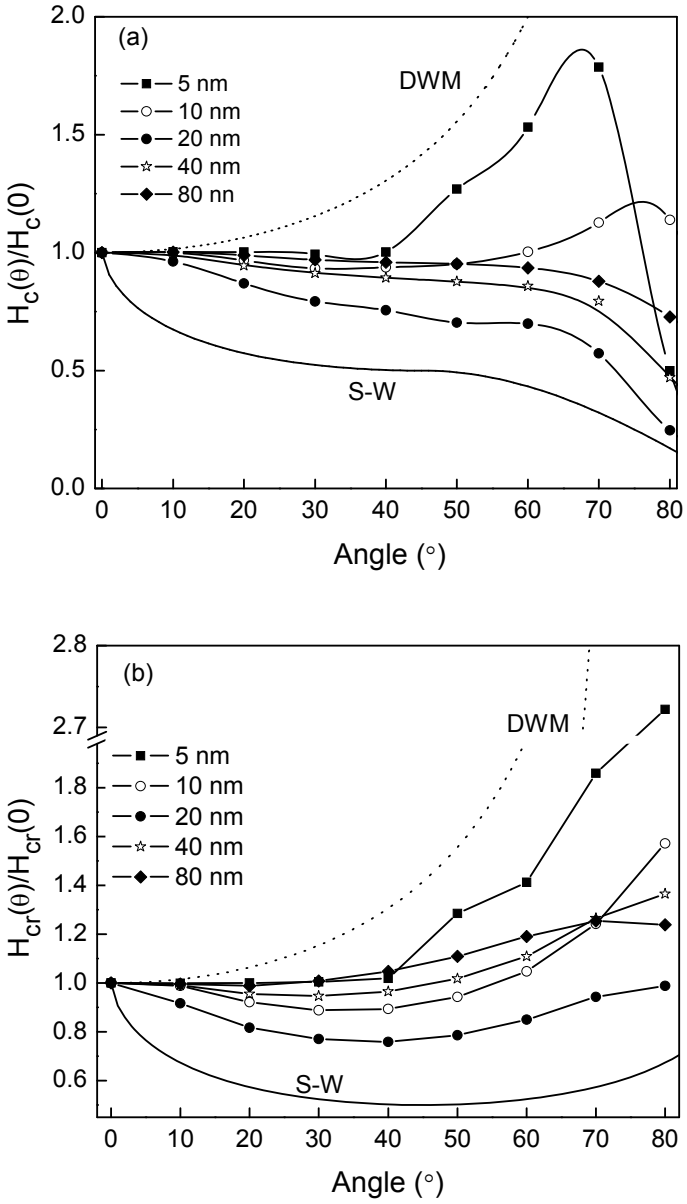

Figure 5.6: Angular dependence of (a) normalized coercivity and (b) normalized remanent coercivity of different thickness for $Co_{72}Pt_{28}$ films deposited on Ru(30 nm)/Pt(2 nm)/Ta(5 nm)/glass. Here θ is the angle between the film normal (easy axis) and applied field directions. The S-W model and the domain wall motion (DWM) model were plotted for comparison.

This indicated that $Co_{72}Pt_{28}$ film had strongly interacting grains at small thickness (5 nm) and weakly decoupled grains at intermediate thickness (~20 nm). The magnetic interaction was further increased with increasing the thickness above 20 nm. It is consistent with the grain isolation observed from the bright field plane-view TEM

images shown in Fig. 5.2(c). Figure 5.6(b) shows the normalized remanent coercivity as a function of angle (θ) for different $Co_{72}Pt_{28}$ film thickness with the S-W model defined by equation (2.7) and domain wall motion (assuming irreversible magnetization) defined by equation $H_{cr}(\theta)/H_{cr}(0) = 1/\cos(\theta)$. The 5 nm film clearly resembled more closely to the reversal behavior of domain wall motion. The curve of 20 nm film approached towards the S-W model. With further increasing thickness, deviation from the S-W model was observed.

5.2.3.3 Magnetic domain

In order to investigate the effects of intergranular magnetic interaction in $Co_{72}Pt_{28}$ films on magnetic domain size, some representative samples were imaged by MFM. Figures 5.7(a)-5.7(c) show the MFM images of AC demagnetized films of thickness 5 nm, 20 nm and 80 nm, respectively. The bright and dark contrast corresponding to increasing and decreasing vertical gradient of magnetic forces on the tip were observed, which represented the domain pattern. Figure 5.7(a) shows the network like morphology of domain size >1000 nm, which was attributed to a magnetically interacting grains in the initial layer. The network formation of domain rendered the domain wall movement easier, consequently magnetization reversal of magnetic grains preferred to follow domain wall motion behavior, as was observed in angular dependent measurement of H_c and H_{cr}. The magnetization reversal by domain wall motion could be responsible for very small coercivity at small thickness. With increasing thickness to 20 nm, the domain size drastically reduced to 250 nm and formed dot like pattern. This could be attributed to the isolated grains in the later stage of film growth as observed from the plane-view and cross-section TEM images in Fig

5.2(b) and Fig. 5.3(a) respectively. The observed domain pattern was consistent with the results reported by T. D. Lee et al.[109] With further increasing the thickness to 80 nm, the dot like pattern remained but its size increased to 350 nm (Fig. 5.7(c)). It could be associated with further increase in magnetic interaction compared to 20 nm thick film due to reduced physical grain isolation as observed from the TEM images in Fig. 5.2(c) and Fig. 5.3(b).

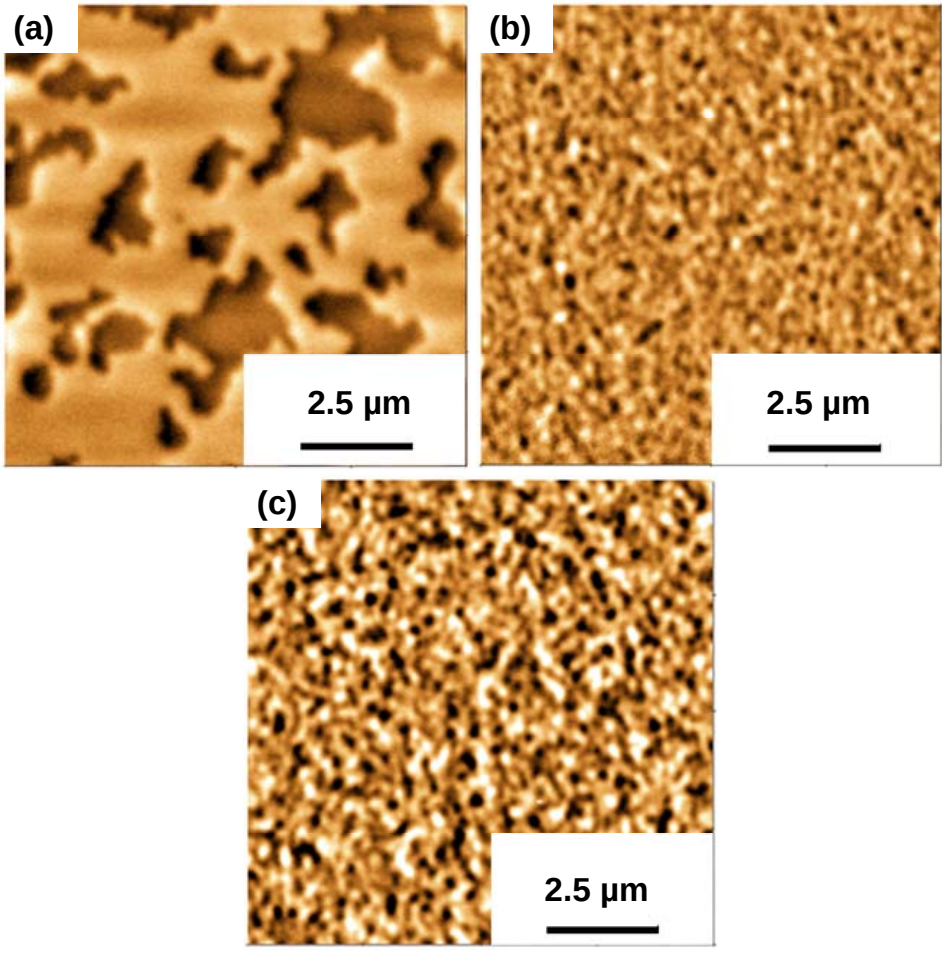

Figure 5.7: MFM images of (a) 5 nm, (b) 20 nm and (c) 80 nm $Co_{72}Pt_{28}$ thin films deposited on Ru(30 nm)/Pt(2 nm)/Ta(5 nm)/glass. All samples were AC demagnetized before measurement.

5.3 Summary

The origin of microstructural evolutions with increasing film thickness of $Co_{72}Pt_{28}$ films was investigated and magnetization reversal mechanisms were addressed on the basis of microstructure. It was observed that with increasing film thickness, the $Co_{72}Pt_{28}$ film changed from strongly interacting grains at small thickness to weakly decoupled grains at intermediate thickness. Due to strong interaction in the initial stage, the magnetization reversal followed the domain wall motion behavior. With further increasing thickness, the magnetization reversal behavior changed towards the S-W model due to magnetically isolated grain in the later stage of film growth. In order to minimize the surface energy, the film grew in a inverted frustum shape at large thickness and further increased the intergranular exchange interaction.

Chapter 6
Effects of interface roughness of Ta seedlayer on magnetocrystalline anisotropy of CoPt thin films

In magnetic recording media, layer engineering approach is used to achieve desired properties. In multilayer system, the interface roughness of underlayer plays very important role in determining the crystallographic structure of subsequent layer.[110,111] The magnetic properties of recording layer greatly depend on the structure and microstructure of underlayer. For example, in current CoCrPt media Ru/Ta is widely used as a underlayer materials, and quality of Ru (0002) texture determines the quality and magnetic properties of (0002) texture CoCrPt film. An extensive study has been done to understand the effects of Ru underlayer on the magnetic properties of recording layer. However, the effects of Ta seedlayer are yet to be understood. Sen et al[112] have reported that smoother surface of Ta seedlayer deposited at high deposition power increases coercivity, but reason of coercivity enhancement is currently not understood. In this chapter, the effects of interface roughness of Ta seedlayer on magnetic properties of $Co_{72}Pt_{28}$ were investigated.

6.1 Experimental methods

The schematic diagram of layer structure was kept the same as described in Fig. 3.2. Pt(2 nm)/$Co_{72}Pt_{28}$(20 nm)/Ru(30 nm)/Pt(2 nm)/Ta(5 nm)/glass films were deposited by magnetron sputtering. The deposition parameters of all layers except Ta seedlayer were kept the same as described in section 3.1. The deposition rate of Ta was 0.1 nm/sec at the deposition power of 50 W. Three different samples were fabricated in which Ta was deposited at 50 W, 100 W and 250 W, keeping all other

parameters the same. The samples with pre-coated Ta at 50 W, 100 W and 250 W were identified as sample A, B and C, respectively. Ta thickness was fixed at 5 nm. When deposition power of Ta was increased, the deposition time was reduced according to pre-determined linear relationship between the deposition rate and power.

6.2 Results and discussion

6.2.1 Surface morphology of Ta seedlayer

To understand the role of Ta seedlayer, the surface morphology of 5 nm Ta seedlayer deposited at 50 W, 100 W and 250 W was measured by AFM. The results are shown in Figs. 6.1(a)-6.1(c). Root mean square surface roughness (R_{rms}) of Ta deposited at 50 W, 100 W and 250 W were 1.2 nm, 0.8 nm and 0.5 nm, respectively. Figure 6.1(a) showed a large density of small islands, which were attributed to the high melting point (3020 °C) and large free surface energy of Ta seedlayer compared to the underlying glass substrate.[113] Increasing deposition power increased the number of atoms reaching the substrate. Due to the high melting point of materials, the atoms of the deposited islands were unlikely to rearrange themselves by surface diffusion due to insufficient time and temperature. Therefore, further incoming atoms preferred to fill in the voids between initially deposited islands, resulting in a smoother surface.

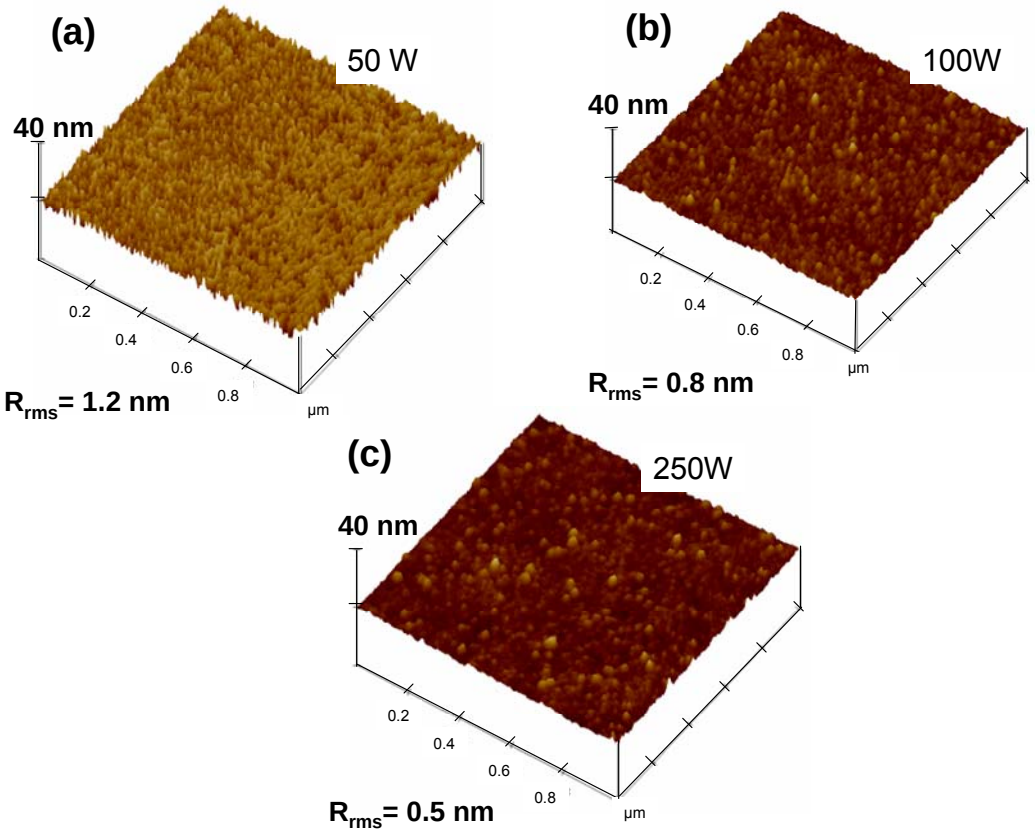

Figure 6.1: AFM images of Ta(5 nm)/glass. Ta was deposited at (a) 50 W, (b) 100 W and (c) 250 W. Scans size was 1 µm x 1 µm.

6.2.2. Crystallographic structure

Figure 6.2 shows the x-ray powder scans of sample A, B and C. All samples exhibited only one combined peak of Ru (0002) and $Co_{72}Pt_{28}$ (0002) due to their partial overlapping as discussed in section 3.2.1. A knee corresponding to $Co_{72}Pt_{28}$ (0002) peak could be seen on the right side of the main peak, which became more and more prominent with increasing deposition power indicating improvement in $Co_{72}Pt_{28}$ texture quality. The integrated intensity of Ru (0002)+$Co_{72}Pt_{28}$ (0002) peak increased, whereas the $\Delta\theta_{50}$ decreased from 8.3° to 7.1° (inset of Fig. 6.2), as Ta deposition power increased from 50 W to 250 W. This suggested that increasing deposition

power of Ta seedlayer improved the crystallinity as well as the c-axis distribution in the $Co_{72}Pt_{28}$/Ru layers. Due to the partial overlapping of Ru (0002) and $Co_{72}Pt_{28}$ (0002) peaks, the effects of Ta seedlayer on either layer could not be distinguished.

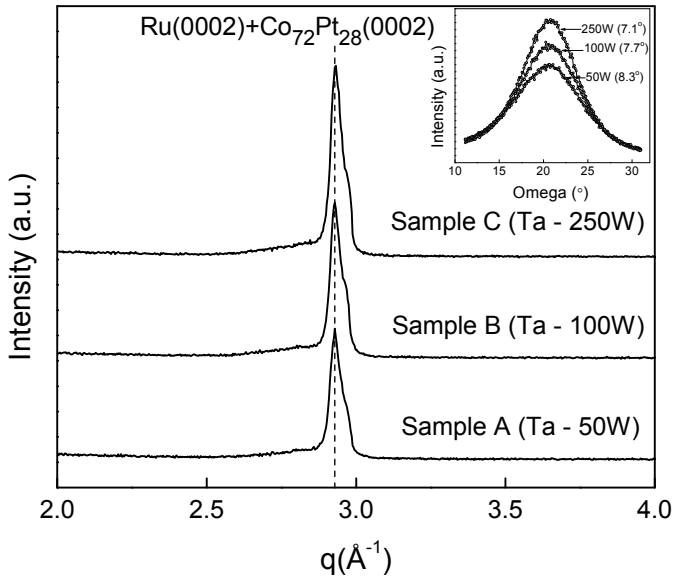

Figure 6.2: X-ray powder scans of Pt(2 nm)/$Co_{72}Pt_{28}$(20 nm)/Ru(30 nm)/Pt(2 nm)/Ta(5 nm)/glass, where Ta was deposited at 50 W (sample A), 100 W (sample B) and 250 W (sample C). Inset is the rocking curve of the respective sample.

In order to see the effects of Ta deposition power on Ru underlayer, another sets of samples Ru(30 nm)/Pt(2 nm)/Ta(5 nm)/glass were deposited without magnetic layer, while keeping all other parameters the same. Figure 6.3 shows the x-ray powder scans of samples without magnetic layer. It showed similar trend as observed in Fig. 6.2. The integrated intensity of the Ru (0002) peak also increased and the $\Delta\theta_{50}$ decreased from 7.4° to 6.6° with increasing Ta deposition power from 50 W to 250 W. The mosaic distribution of samples without magnetic layer was less than that of corresponding samples with the magnetic layer. This was attributed to the lack of overlapping of the Ru (0002) and $Co_{72}Pt_{28}$ (0002) peaks, as the $Co_{72}Pt_{28}$ peak also contributed to the peak broadening. The XRD data showed that the deposition power

of Ta seedlayer significantly improved the crystallinity and c-axis distribution for the $Co_{72}Pt_{28}$/Ru and Ru layers.

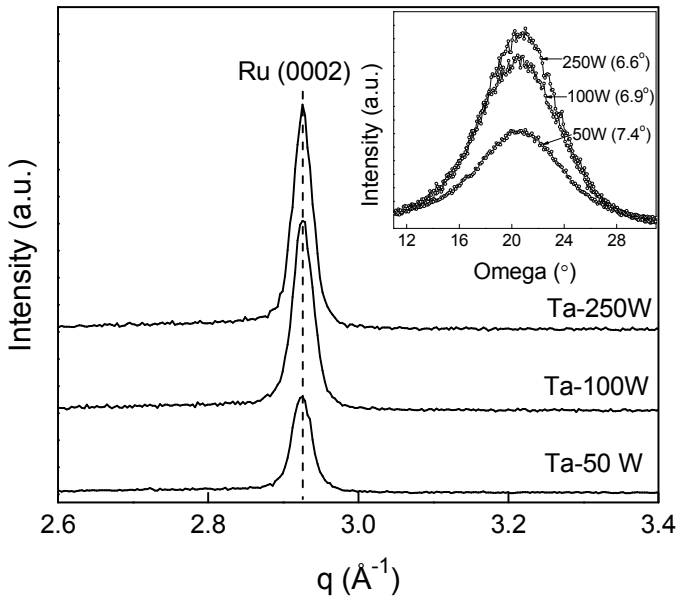

Figure 6.3: X-ray powder scans of Ru(30 nm)/Pt(2 nm)/Ta(5 nm)/glass, where Ta was deposited at 50 W, 100 W and 250 W. Inset is the rocking curve of respective samples.

6.2.3 Magnetic properties

6.2.3.1 Coercivity

Figures 6.4(a)-6.4(c) show the in-plane and out-of-plane hysteresis loops of samples A, B and C, respectively. It showed that all samples exhibited perpendicular anisotropy, and the out-of-plane coercivity, $H_{c\perp}$, increased with increasing the deposition power of Ta seedlayer, whereas the in-plane coercivity, $H_{c//}$, showed an opposite trend. As the deposition power of Ta seedlayer increased from 50 W to 250 W, $H_{c\perp}$ increased from 4.4 kOe to 5.5 kOe, but $H_{c//}$ decreased from 1.2 kOe to 0.8 kOe. The negative nucleation field in the out-of-plane measurement also increased

from 1.2 kOe to 2.8 kOe with increasing deposition power of the Ta seedlayer from 50 W to 250 W. The increased coercivity could be attributed to either a different magnetization reversal mechanism or increased K_u value, or due to their combined effect.

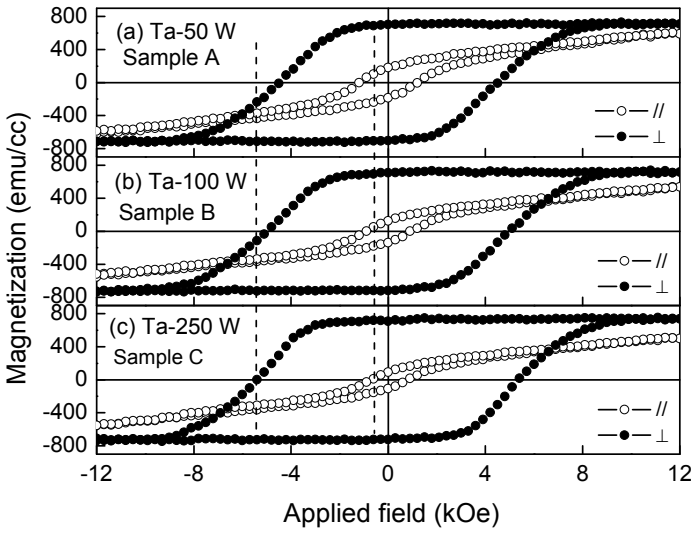

Figure 6.4: In-plane and out-of-plane hysteresis loops of Pt(2 nm)/$Co_{72}Pt_{28}$(20 nm)/Ru(30 nm)/Pt(2 nm)/Ta(5 nm)/glass, where Ta was deposited at (a) 50 W (sample A), (b) 100 W (sample B) and (c) 250 W (sample C).

6.2.3.2 Magnetization reversal mechanism

It is well accepted that coercivity of hard magnetic materials is an extrinsic property and mainly determined by magnetization reversal behavior and magnetic crystal anisotropy. In order to investigate the switching behavior, the angle-dependent coercivity was measured. Figure 6.5 shows the angular dependence of $H_c(\theta)/H_c(0)$ (where $H_c(0)$ is the coercivity for $\theta = 0^\circ$) as a function of applied magnetic field angle θ with respect to the film normal for samples A, B and C. The ideal S-W model and the domain wall motion model were also plotted for

comparison. The measured values of $H_c(\theta)/H_c(0)$ of the samples A, B and C showed deviation from both the S-W model as well as the domain wall motion model. However, our results showed that the switching behavior approached the S-W model when compared with the domain wall motion model. Comparison among the three samples indicated that the film grown on Ta pre-coated at 250W (sample C) showed a greater degree of magnetic interaction, as it deviated the most from the ideal S-W model.

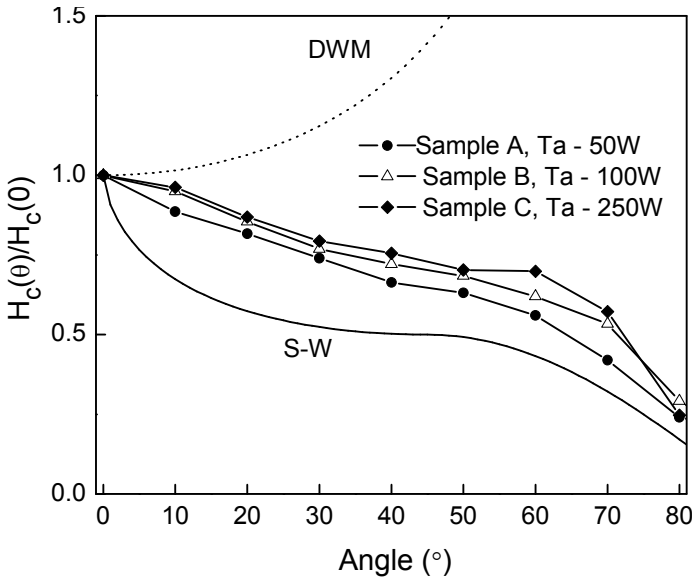

Figure 6.5: Angle dependent normalized coercivity of Pt(2 nm)/$Co_{72}Pt_{28}$(20 nm)/Ru(30 nm)/Pt(2 nm)/Ta(5 nm)/glass, where Ta was deposited at 50 W (sample A), 100 W (sample B) and 250 W (sample C). The S-W model and the domain wall motion (DWM) model were plotted for comparison.

The results were consistent with the results of shearing parameter, $\alpha = 4\pi(dM/dH)_{H=Hc(\perp)}$, which is a measure of inter-granular magnetic interaction, and unity for completely non-interacting grains. The shearing parameter was 3.3, 3.6 and 3.9 for samples A, B and C respectively. Ideally, the perpendicular

coercivity of sample C should be less than that of sample A because of cooperative switching due to large inter-granular exchange interaction in sample C. However, the coercivity of sample C was larger than that of sample A, which was contrary to the common assumption. This revealed that the high coercivity of sample C could be attributed to a large magnetic anisotropy of magnetic film, since coercivity, $H_c \propto 2K_u / M_s$, where, K_u is the magnetocrystalline anisotropy and M_s is the saturation magnetization of the magnetic layer.

6.2.3.3 Magnetocrystalline anisotropy

In the previous section it was analyzed that the increased coercivity with increasing the Ta deposition power was not ascribed to different magnetization reversal mechanism. In order to investigate the effects of seedlayer on the magnetocrystalline anisotropy, the magnetocrystalline anisotropy was measured with the torque magnetometer in applied fields of 12 kOe. However, the applied field was less than the anisotropy field, H_k (the field corresponding to the intersection point of in-plane and out-of-plane hysteresis loops). Due to insufficient field, the magnetization direction was not aligned along the field direction. As a result, clock-wise (CW) and counter clock-wise (CCW) torque curves were not superimposed in Fig 6.6 for sample C. In order to extract the information about magnetic anisotropy, the torque curves were first corrected and then Fourier analyzed. Figure 6.7 shows the experimental and corrected CCW curves of sample C. The total anisotropy, $K_{u,}$ (first order anisotropy constant ($K_{,1}$) plus second order anisotropy constant (K_2)) was determined according to following relation described in section 2.3.3.1.

$$K_u = K_{u(eff)} + 2\pi M_s^2 \qquad (5.1)$$

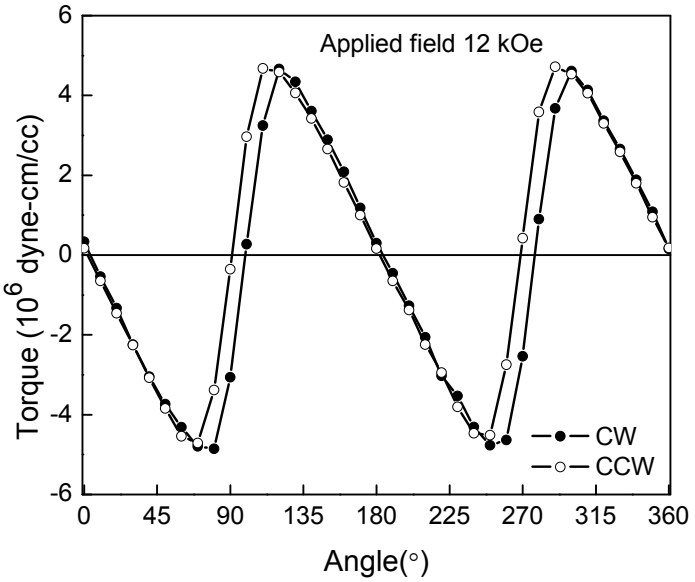

Figure 6.6: Torque curve of sample C in the applied field of 12 kOe. Solid symbol (●) and open circle (○) show clock-wise (CW) and counter clock-wise (CCW) measurements, respectively.

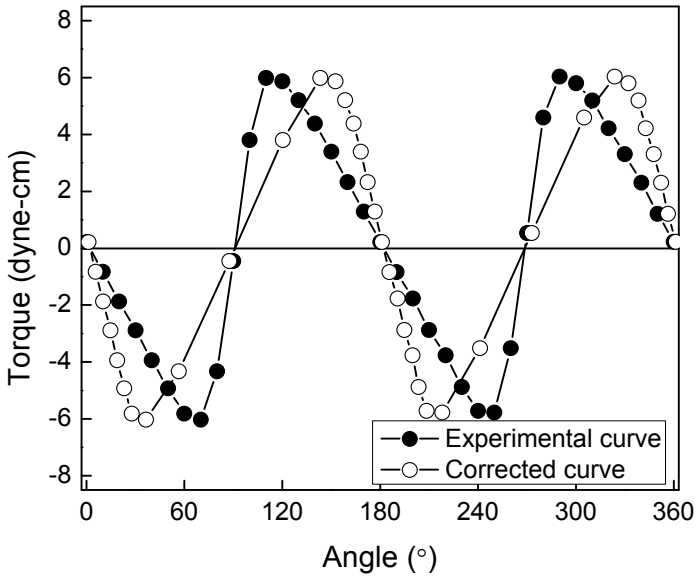

Figure 6.7: Experimental CCW curve and corrected CCW curve, of sample C in the applied field of 12 kOe,

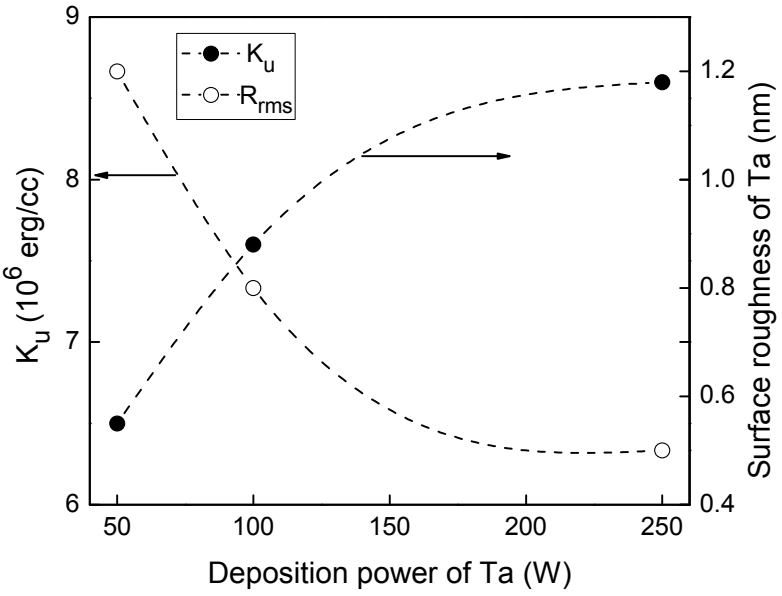

Figure 6.8: Variation of magnetocrystalline anisotropy, K_u, of Pt(2 nm)/$Co_{72}Pt_{28}$(20 nm)/Ru(30 nm)/Pt(2 nm)/Ta(5 nm)/glass, and root mean square surface roughness (R_{rms}) of Ta seedlayer versus Ta deposition power.

The self-energy due to the demagnetization was assumed to be same in all samples because no significant difference was observed in the saturation magnetization (determined from the out-of-plane hysteresis loops) and the grain size of samples A, B and C. Figure 6.8 shows the plot of the perpendicular magnetocrystalline anisotropy and the surface roughness versus deposition power of Ta seedlayer. The perpendicular magnetocrystalline anisotropy increased from 6.5 x 10^6 erg/cc to 8.6 x 10^6 erg/cc, and the surface roughness of Ta seedlayer decreased from 1.2 nm to 0.5 nm, as deposition power of Ta seedlayer increased from 50 W to 250 W. This indicated that magnetic anisotropy and Ta surface roughness had inverse relationship with increasing Ta deposition power. The magnetic anisotropy showed 32% enhancement with reducing the surface roughness of Ta from 1.2 nm to 0.5 nm in this study. The increased magnetocrystalline anisotropy was attributed to improved quality of the *hcp* $Co_{72}Pt_{28}$ (0002) texture[114] with reducing the Ta interface roughness. Assuming the cylindrical

grains of height of 20nm, and magnetic anisotropy 8.6×10^6 erg/cc, the thermally stable grain can be achieved down to 4.5 nm, which is sufficient to support the areal density of 1 Tbit/in$^{2.}$

6.3 Summary

The effects of interface roughness of Ta seedlayer on the structural and magnetic properties of $Co_{72}Pt_{28}$ films were investigated. The increased uniaxial perpendicular magnetocrystalline anisotropy (8.6×10^6 erg/cc), $H_{c\perp}$ (5.5 kOe) and nucleation field (-2.8 kOe) in the $Co_{72}Pt_{28}$ film sputter-deposited on relatively smooth surface of Ta seedlayer were achieved. This was attributed to improved quality of the *hcp* $Co_{72}Pt_{28}$ (0002) texture with reducing the Ta interface roughness.

Chapter 7
Effects of Ru underlayer on microstructure and magnetic properties of CoPt thin films

The key requirements of perpendicular recording media for Co-based alloy are growth of (0002) texture to have the easy axis of magnetization along the film normal direction, and small and magnetically isolated grains to achieve large *SNR*. The texture of magnetic layer in recording media is controlled by texture of suitable underlayer materials. For example, Cr (110) and Cr (200) underlayers induce $(10\bar{1}1)$ and $(10\bar{2}1)$ textures, respectively, in the Co-based media to align c-axis in the film plane or close to the film plane for longitudinal magnetic recording.[9-12] Though Cr (110) has the lowest surface energy, the growth of Cr (110) and Cr (200) textures depend on deposition parameters.[115] Currently, Ru is used as an underlayer in granular *hcp* CoCrPt-oxide perpendicular recording media,[116-118] since Ru and CoCrPt both are the *hcp* and lattice mismatch between the Ru (0002) and CoCrPt (0002) textured films is less than 8%. Therefore, the Ru (0002) texture can easily induce (0002) texture in CoCrPt. Oikawa et al.[119] have investigated the effects of Ru thickness on mosaic distribution and observed that mosaic distribution decreases with increasing the Ru thickness.

To achieve large SNR, the traditional method of controlling the grain size and intergranular exchange interaction is based on the Thornton diagram, wherein the growth of thin films favors columnar grains with voided region between grains under high Ar pressure and low temperature.[66] Park et al.[63,120] had attempted to optimize the deposition pressure and temperature of Ru underlayer. They reported that Ru developed $(10\bar{1}0)$ peak[120] when deposited at high temperature and increased mosaic

distribution when deposited at high deposition pressure,[63] which were undesirable for perpendicular magnetic recording. The grain size and intergranular exchange interaction in current CoCrPt-SiO_2 recording media is controlled by manipulating the SiO_2 compositions and/or adding the oxygen with Ar during the deposition of recording layer as an alternative of Thornton diagram approach. Higher percentage of SiO_2 reduces both the grain size (5-6 nm) and K_u value.[60,62] The reduced value of K_u shows adverse impact on increasing areal density. Zheng et al.[61] have investigated the effects of oxygen incorporation and reported that addition of oxygen improved the *SNR*. However, entrapped oxygen ions inside the grain deteriorate the magnetic properties. Dual-layer structure of Ru, in which bottom layer of Ru (Ru_b) was deposited at low Ar pressure to develop (0002) texture, and top layer Ru (Ru_t) deposited at high Ar pressure to reduce the grain size and intergranular exchange interaction, was developed.[63] Piramanayagam el al.[65] successfully achieved the grain size down to 5.5 nm using synthetic nucleation layer between the top and bottom Ru layers. However, the search of nucleation layer was largely based on trial-and-error. The performance of a dual-layer structure depends on relative thickness of Ru_t and Ru_b, and deposition pressure of Ru_t layer. Park et al.[63] reported that increasing deposition pressure of Ru_t increased the coercivity due to reduced intergranular exchange interaction.

Although the effects of Ru underlayer on microstructural and magnetic properties of CoCrPt-oxide media have been investigated, its effects on CoPt are yet to be understood. As a result, this chapter focused on investigation of the effects of thickness, deposition pressure and dual-layer structure of Ru underlayer on the crystallographic and microstructural evolution, and magnetic properties of $Co_{72}Pt_{28}$.

7.1 Experimental methods

The schematic diagram of layer structure was kept the same as described in Fig. 3.2. The deposition parameters were also the same as discussed in section 3.1, except for the Ru underlayer. To investigate the effects of thickness, deposition pressure and dual-layer structures of Ru on microstructure and magnetic properties of $Co_{72}Pt_{28}$, three sets of samples were fabricated by magnetron sputtering in Ar.

- In the first set, Pt(2 nm)/$Co_{72}Pt_{28}$ (20 nm)/Ru(x nm)/Pt(2 nm)/Ta(5 nm)/glass (where x = 0, 10, 20, 30, 50 and 70 nm) films were deposited to study the effects of thickness of Ru underlayer. The deposition pressure of Ru was 0.5 mTorr.
- In the second set, the thickness of Ru was fixed at 30 nm and deposition pressure was varied from 0.5, 5, 10 to 20 mTorr. All other parameters were kept the same as in the first set of sample.
- In the third set, the Ru underlayer was deposited in two steps. In the first step, 20 nm Ru (Ru_b) was deposited at 0.5 mTorr Ar pressure. In the second step, 5, 10, 15 and 20 nm Ru (Ru_t) were deposited at 10 mTorr Ar pressure, keeping all other parameters the same as set one.

In Chapter 3, it was found that due to partial overlapping, the Ru (0002) and $Co_{72}Pt_{28}$ (0002) peaks could not be resolved for 20 nm $Co_{72}Pt_{28}$. In order to investigate the effects of different parameters on Ru underlayer as mentioned from set one to set three, additional samples were fabricated without $Co_{72}Pt_{28}$ magnetic layer for structural characterization of Ru underlayer.

7.2 Results and discussion

7.2.1 Effects of Ru thickness

7.2.1.1 Crystallographic structure

Figure 7.1 shows the x-ray powder scans of Pt(2 nm)/$Co_{72}Pt_{28}$(20 nm)/Ru(x nm)/Pt(2 nm)/Ta(5 nm)/glass, where $0 \leq x \leq 70$ nm. A single peak combining Ru (0002) and $Co_{72}Pt_{28}$ (0002) was appeared. In the absence of Ru underlayer, a small $Co_{72}Pt_{28}$ (0002) peak was detected (Figure 7.2 shows enlarged view of this sample). Rocking curve of such peak was almost flat. It indicated that Ru underlayer was necessary to develop (0002) texture in $Co_{72}Pt_{28}$ film. The integrated intensity of combined peak increased with increasing Ru thickness. At 30 nm Ru, a knee corresponding to $Co_{72}Pt_{28}$ appeared on the right side of the peak, consistent with Fig. 3.3. The knee at 10 nm and 20 nm Ru was not significant. It could be due to a poor Ru texture. The texture quality of $Co_{72}Pt_{28}$ was determined by the texture quality of Ru underlayer, hence a poor Ru texture could deteriorate the texture quality of $Co_{72}Pt_{28}$ resulting of reduced intensity. However, at 50 nm and 70 nm Ru, the disappearance of knee could be attributed to the large intensity of Ru (0002) peak compared to the corresponding $Co_{72}Pt_{28}$ peak due to large Ru thickness.

In order to investigate the effects of Ru thickness on its crystallinity and mosaic distribution, separate sets of samples were prepared without magnetic layer keeping all other parameters the same. Figure 7.3 shows the x-ray powder scans of different thickness of Ru underlayer. All Ru films showed only (0002) preferred orientation irrespective of the Ru thickness. Figure 7.4 shows the $\Delta\theta_{50}$ and normalized integrated intensity of the Ru (0002) peak determined from the rocking curve measurement for different Ru thickness without magnetic layer. The integrated

intensity of different thickness was normalized using the data of 10 nm thick Ru film. The normalized integrated intensity was calculated according to the formula, $I_{norm} = [(I_x / I_{10})(10/x)]$, where I_x and I_{10} are the integrated intensity of x nm and 10 nm Ru films, respectively.

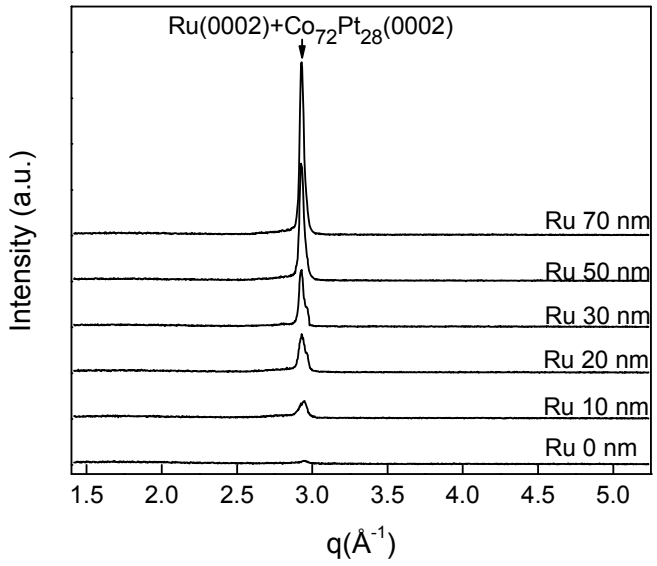

Figure 7.1: X-ray powder scans of Pt(2 nm)/$Co_{72}Pt_{28}$(20 nm)/Ru(x nm)/Pt(2 nm)/Ta(5 nm)/glass, where x = 0, 10, 20, 30, 50 and 70 nm.

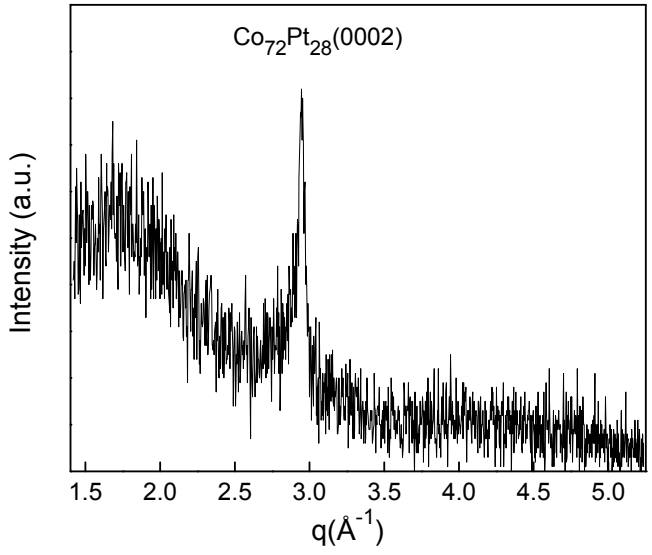

Figure 7.2: X-ray powder scans of Pt(2 nm)/$Co_{72}Pt_{28}$(20 nm)/Pt(2 nm)/Ta(5 nm)/glass.

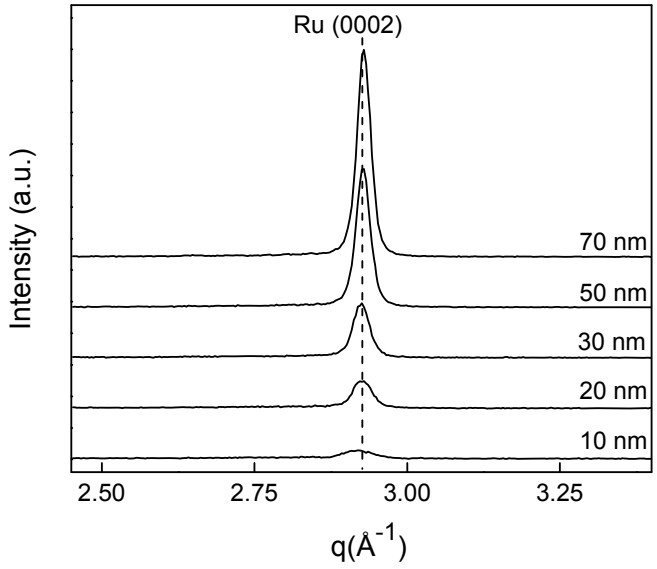

Figure 7.3: X-ray powder scans of Ru(x nm)/Pt(2 nm)/Ta(5 nm)/glass, where x = 10, 20, 30, 50 and 70 nm.

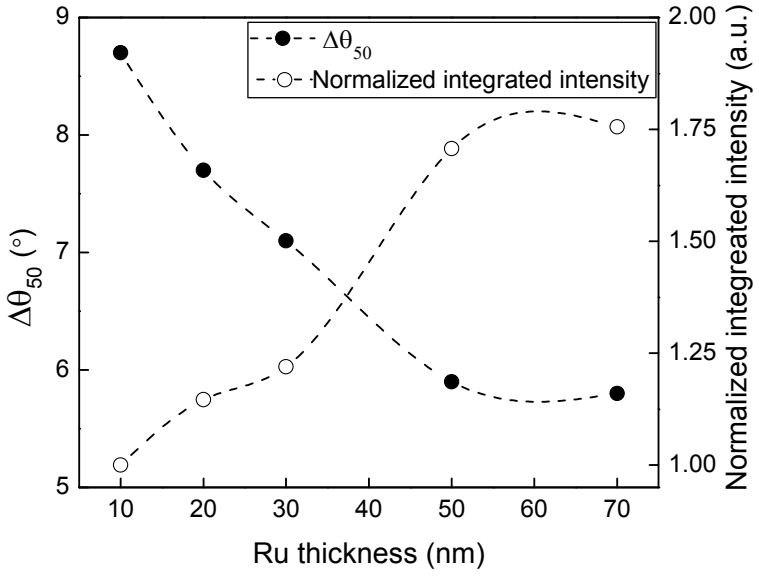

Figure 7.4: The $\Delta\theta_{50}$ and normalized integrated intensity of Ru (0002) peak (measured from the rocking curve) as a function of Ru underlayer thickness deposited on Pt(2 nm)/Ta(5 nm)/glass.

This showed that the $\Delta\theta_{50}$ monotonically decreased from 8.7° to 5.8° and normalized integrated intensity increased by 1.75 times with increasing Ru thickness from 10 nm

to 70 nm. This indicated that increasing Ru thickness improved the crystallinity and mosaic distribution in Ru film. This suggested that disappearance of the knee corresponding to $Co_{72}Pt_{28}$ (0002) at 10 nm and 20 nm Ru was associated with a poor Ru texture, whereas at 50 nm and 70 nm due to large intensity of Ru, as observed from Fig. 7.1.

7.2.1.2 Microstructure

Figures 7.5(a)-7.5(c) show the plane-view bright field TEM images of 20 nm $Co_{72}Pt_{28}$ film deposited on 10 nm, 30 nm and 70 nm Ru, respectively. It showed that the grain size of $Co_{72}Pt_{28}$ film deposited on 30 nm Ru was smaller and isolated by more voided boundaries (bright regions in the TEM images) compared to that deposited on 10 nm and 50 nm.

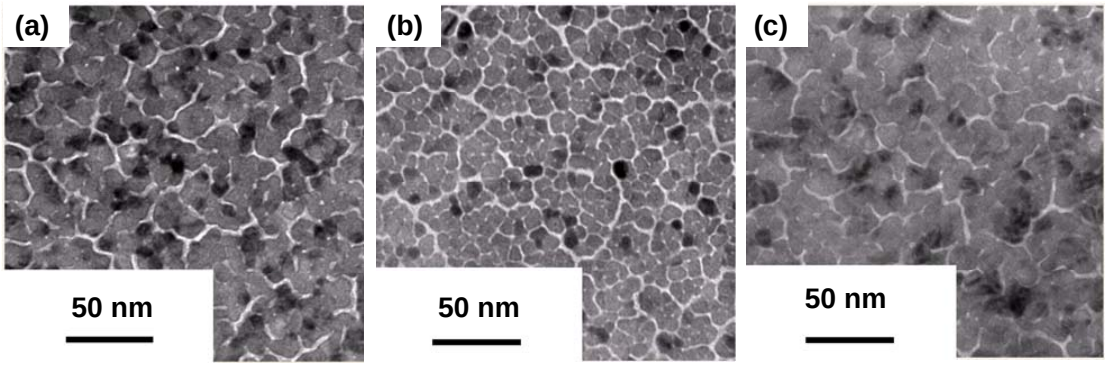

Figure 7.5: Plane-view TEM images of $Co_{72}Pt_{28}$(20 nm) deposited on different Ru underlayer thickness of (a) 10 nm, (b) 30 nm and (c) 50 nm.

7.2.1.3 Magnetic properties

Figures 7.6(a)-7.6(d) show the hysteresis loops of selected samples of $Co_{72}Pt_{28}$ film deposited on different Ru underlayer thickness. Figure 7.6(a) indicated that the

$Co_{72}Pt_{28}$ film showed in-plane easy axis of magnetization and small coercivity in the absence of Ru, which was undesirable for perpendicular magnetic recording. It was attributed to the absence of good (0002) texture in the $Co_{72}Pt_{28}$ film, as observed from the XRD data in Fig. 7.1. The easy axis of magnetization of $Co_{72}Pt_{28}$ films changed from the in-plane to out-of-plane direction with the presence of 10 nm Ru. Variations of $H_{c//}$, $H_{c\perp}$ and $S_{\perp}$ as a function of Ru thickness are shown in Fig. 7.7. It showed that the $H_{c//}$ slightly increased with increasing the Ru thickness, while $H_{c\perp}$ increased drastically to 5.5 kOe with increasing Ru thickness to 30 nm, and reduced a plateau thereafter. $S_{\perp}$ also increased with increasing the Ru thickness to 30 nm and decreased slightly with further increase of Ru thickness. The increase of $H_{c\perp}$ and $S_{\perp}$ of the $Co_{72}Pt_{28}$ films with the Ru thickness were attributed to a reduced mosaic distribution and improved crystallinity in the Ru underlayer. However, above 30 nm, the mosaic distribution and crystallinity improved, but $H_{c\perp}$ reached a plateau and $S_{\perp}$ was slightly deteriorated with increasing the Ru thickness above 30 nm. This behavior could be associated with reduced grain isolation in the $Co_{72}Pt_{28}$ film deposited on Ru underlayer thicker than 30 nm, as observed from the plane-view TEM image in Fig. 7.5(c) deposited on 50 nm Ru. The reduced grain isolation could influence the neighbor grains for early switching resulting in reduced value of $S_{\perp}$. This indicated that an optimum thickness of the Ru was required to achieve large $H_{c\perp}$ and $S_{\perp}$ for the $Co_{72}Pt_{28}$ films.

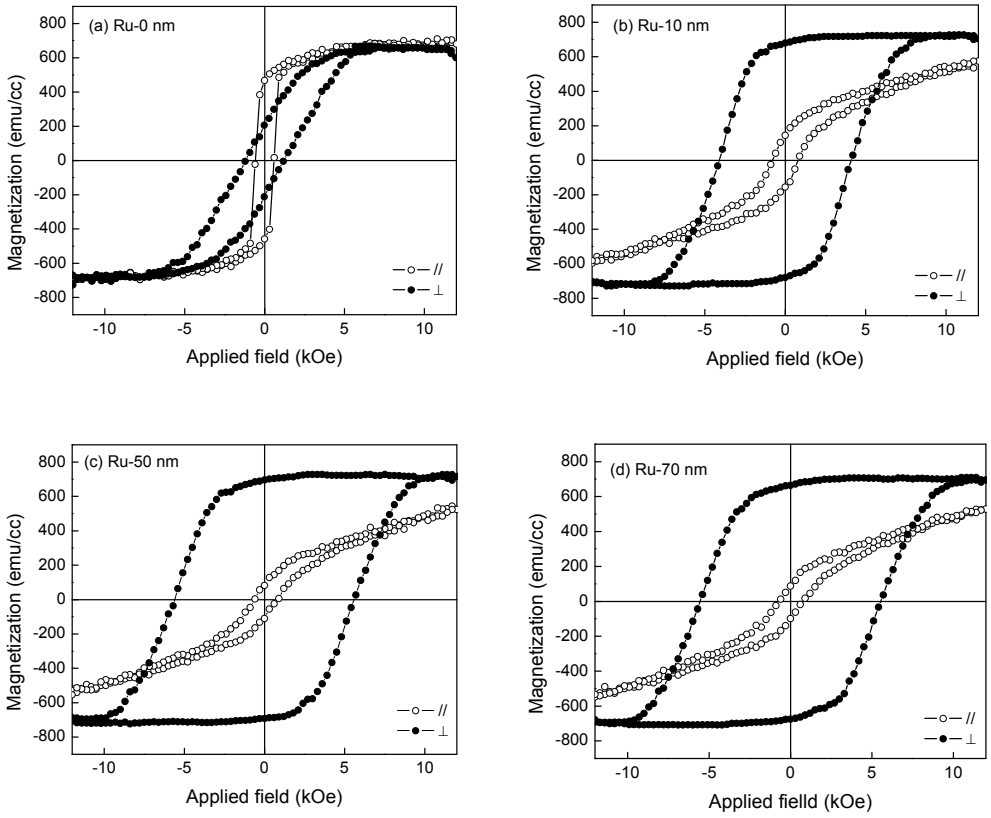

Figure 7.6: In-plane and out-of-plane hysteresis loops of $Co_{72}Pt_{28}$ (20 nm) film deposited on different Ru underlayer thickness of (a) 0 nm, (b) 10 nm, (c) 50 nm and (d) 70 nm.

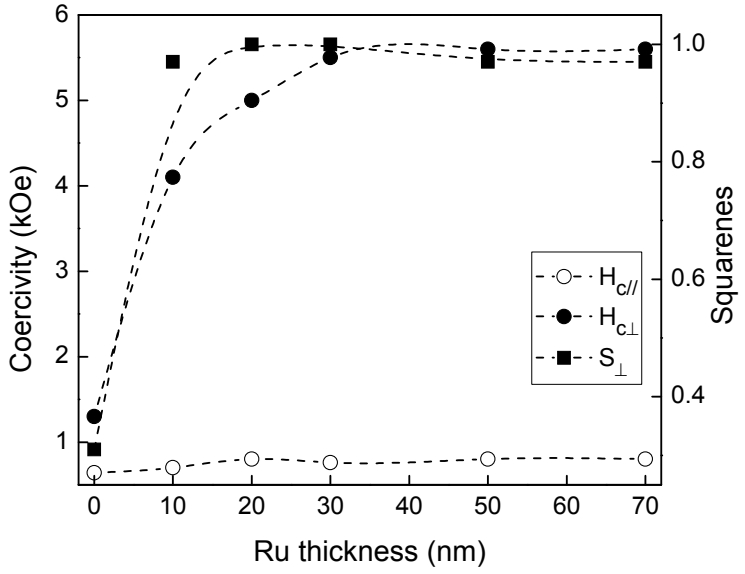

Figure 7.7: Variation of in-plane coercivity $(H_{c//})$, out-of-plane coercivity $(H_{c\perp})$ and out-of-plane magnetization squareness $(S_{\perp})$ as a function of Ru thickness.

7.2.2 Effects of deposition pressure of Ru underlayer

7.2.2.1 Crystallographic structure

In order to understand the role of Ar pressure during the Ru deposition, the x-ray powder scans of Ru(30 nm)/Pt(2 nm)/Ta(5 nm)/glass were performed where Ru was deposited at 0.5, 5, 10 and 20 mTorr Ar pressure. The results are shown in Fig. 7.8. At 0.5 mTorr, only Ru (0002) peak was observed. With increasing the Ru deposition pressure to 5 mTorr, the absolute intensity of Ru (0002) peak decreased abruptly, but the (0002) texture remained. However, when the deposition pressure further increased to 10 mTorr and 20 mTorr, an additional Ru $(10\bar{1}0)$ and Ru $(10\bar{1}1)$ peaks appeared, and the absolute intensities of these peaks were larger than that of the Ru (0002) peak. This indicated that increasing Ar pressure perturbed the Ru (0002) texture. Figure 7.9 illustrates the XRD spectra of 20 nm $Co_{72}Pt_{28}$ film deposited on Ru(30 nm)/Pt(2 nm)/Ta(5 nm)/glass, where Ru was deposited at different Ar pressures.

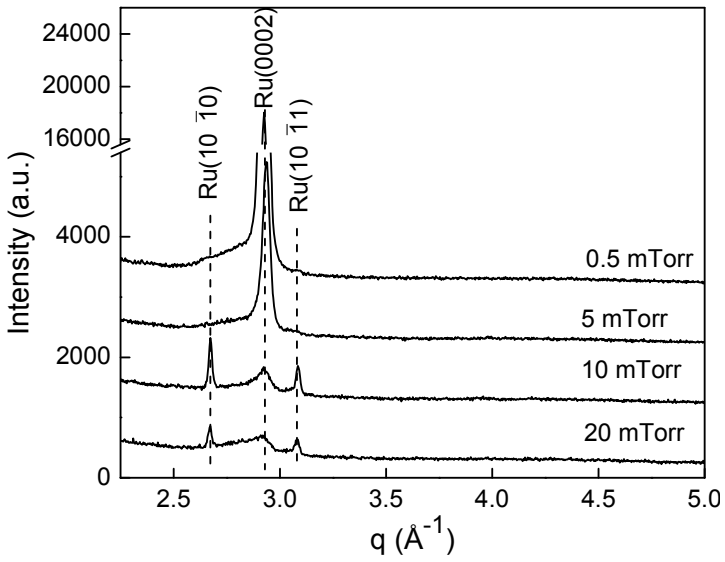

Figure 7.8: X-ray powder scans of Ru(30 nm)/Pt(2 nm)/Ta(5 nm)/glass, where Ru was deposited at 0.5, 5, 10 and 20 mTorr Ar pressure.

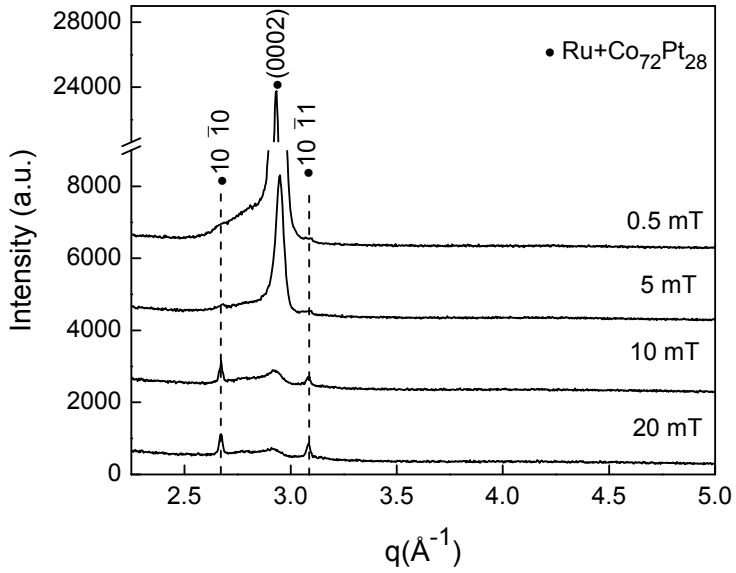

Figure 7.9: X-ray powder scans of Pt(2 nm)/$Co_{72}Pt_{28}$(20 nm)/Ru(30 nm)/Pt(2 nm)/Ta(5 nm)/glass, where Ru was deposited at 0.5, 5 10 and 20 mTorr Ar pressure.

Similar trends as Fig 7.8 were also observed for the film with magnetic layer. This indicated that magnetic layer followed the registry of Ru underlayer. The evolution of Ru $(10\bar{1}0)$ and Ru $(10\bar{1}1)$ peaks with increasing Ar pressure can be understood based on the influence of Ar pressure on the kinetic energy of Ru adatoms. The average kinetic energy of adatoms decreases with increasing Ar pressure due to collision between the sputtered atoms and the Ar atoms. As a result, at low Ar pressure, the kinetic energy of Ru adatoms should be high enough, and hence the lateral mobility would be large. Therefore, the Ru adatoms arriving at the substrate surface rearrange themselves and form a continuous film of lowest surface energy plane. Ru (0002) has lowest surface energy hence it is favorably grown at low Ar pressure. However, with increasing the Ar pressure, the kinetic energy of Ru adatoms decreases. The adatoms do not have sufficient energy to rearrange themselves to a favorable structure and develop faceted island shape as shown in Fig. 7.10. It indicated that the total area of

the sides of facted island was larger than that of the top surface. As a result, in order to minimize total surface energy, Ru (0002) facet was developed laterally, and the next lower surface energy planes such as $(10\bar{1}0)$ and $(10\bar{1}1)$ was developed perpendicularly. This was consistent with the model proposed by Feng et al.[115] for the evolution of different crystallographic texture of Cr films. Figure 7.8 showed that along with Ru $(10\bar{1}0)$ and $(10\bar{1}1)$ peaks, small (0002) peak detected at 10 mTorr and above Ar pressure. This could be attributed to the impingement of some islands before they acquired equilibrium faceted shape. Due to impingement, the area of top surface remained larger than the total area of the sides and favored the growth of (0002) texture.

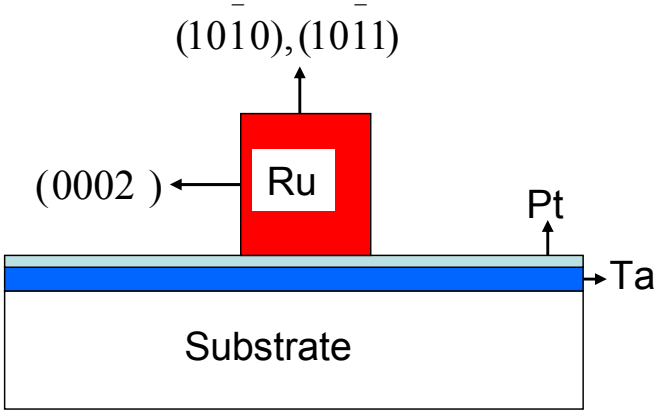

Figure 7.10: Schematic diagram of evolution of different crystallographic facets of Ru, deposited at high Ar pressure.

7.2.2.2 Microstructure

Figures 7.11(a)-7.11(c) show the bright field plane-view TEM images of $Co_{72}Pt_{28}$ film deposited on Ru underlayer grown at 0.5 mTorr, 5 mTorr and 10 mTorr Ar pressure, respectively. The average column width (grain diameter) decreased from

9.0±1.7 nm to 7.2±1.3 nm as Ar pressure increased from 0.5 mTorr to 5 mTorr. In addition to reduced grain diameter and grain size distribution, grain isolation also increased. However, the grain diameter further increased to approximately 15 nm at 10 mTorr Ar pressure, forming agglomerates of ~3-4 grains.

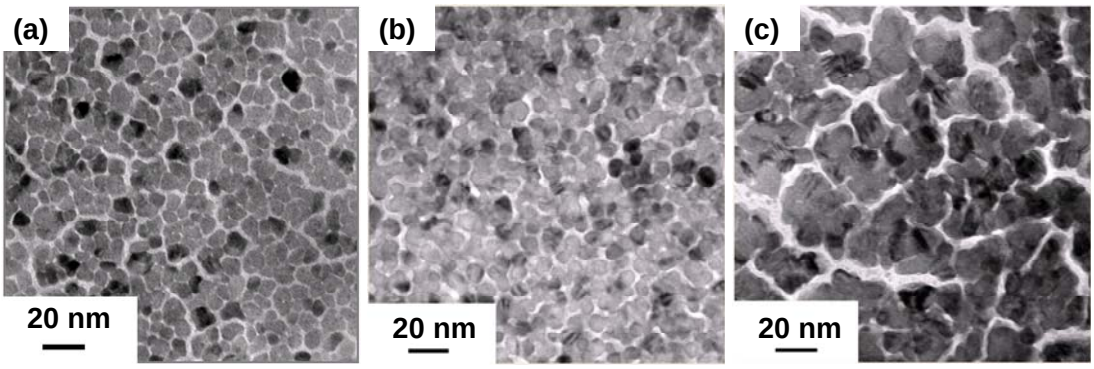

Figure 7.11: Bright field plane-view TEM images of $Co_{72}Pt_{28}$ film deposited on Ru underlayer grown at (a) 0.5 mTorr, (b) 5mTorr and (c) 10 mTorr.

7.2.2.3 Magnetic properties

Figures 7.12(a)-7.12(d) show the in-plane and out-of-plane hysteresis loops of Pt(2 nm)/$Co_{72}Pt_{28}$(20 nm)/Ru(30 nm)/Pt(2 nm)/Ta(5 nm)/glass films, where Ru was deposited at 0.5, 5, 10 and 20 mTorr Ar pressure, respectively. With increasing the deposition pressure of Ru underlayer from 0.5 mTorr to 5 mTorr, $H_{c\perp}$ increased from 5.5 kOe to 6.5 kOe and $H_{c//}$ increased from 1.0 kOe to 1.8 kOe. Perpendicular magnetic anisotropy was retained in this range of sputtering pressure. The shearing parameter of $Co_{72}Pt_{28}$ film was 2.5, when Ru was deposited at 0.5 mTorr Ar. It decreased to 2.2 as Ru deposition pressure increased to 5 mTorr. The reduced shearing parameter indicated the lateral exchange coupling decreased with the increase of the sputtering pressure.

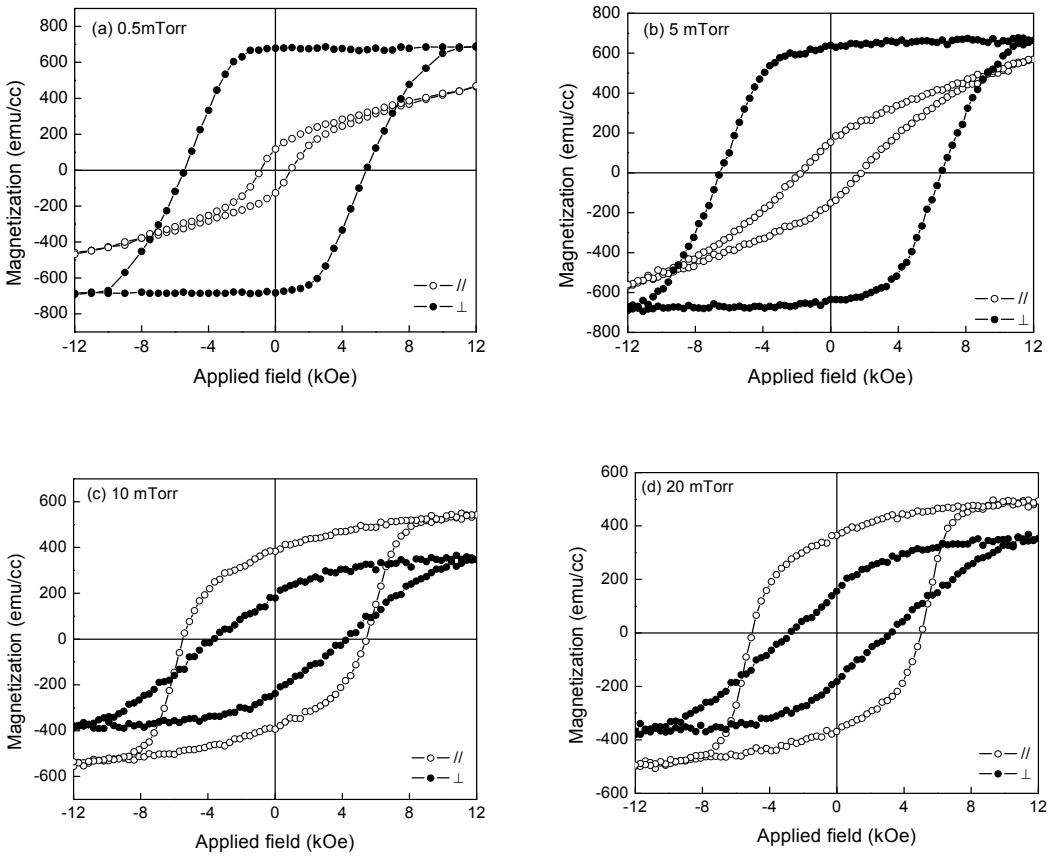

Figure 7.12: In-plane and out-of-plane hysteresis loops of Pt(2 nm)/$Co_{72}Pt_{28}$(20 nm)/Ru(30 nm)/Pt(2 nm)/Ta(5 nm)/glass, where Ru was deposited at (a) 0.5 mTorr, (b) 5 mTorr, (c) 10 mTorr and (d) 20 mTorr Ar pressure.

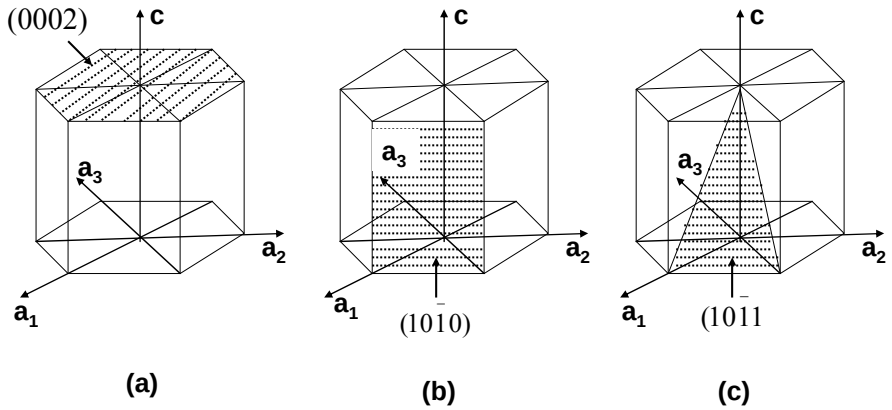

Figure 7.13: Schematic diagram of (a) (0002)**, (b)** $(10\bar{1}0)$ **and (c)** $(10\bar{1}1)$ **planes in *hcp* structure.**

The reduced shearing parameter was consistent with plane-view TEM images (Fig. 7.11). Grains in Fig. 7.11(a) where Ru was deposited at 0.5 mTorr Ar appeared less isolated than that where Ru was deposited at 5 mTorr Ar (Fig. 7.11(b)). This showed that the increased coercivity of $Co_{72}Pt_{28}$ may be attributed to a reduced exchange coupling between magnetic grains when Ru underlayer was deposited at 5 mTorr. With further increasing the deposition pressure to 10 mTorr and 20 mTorr, $H_{c\perp}$ reduced to 3.6 kOe and 2.8 kOe, respectively, whereas $H_{c//}$ increased to 5.5 kOe and 5.1 kOe, respectively. The easy axis of magnetization changed from the out-of-plane direction to the in-plane direction in this pressure range. The change in easy axis of magnetization was associated with emergence of different crystallographic structure at a large Ar pressure. The XRD results (Fig. 7.9) showed that the intensity of (0002) peak was drastically reduced, whereas additional $(10\bar{1}0)$ and $(10\bar{1}1)$ peak appeared for Ru and $Co_{72}Pt_{28}$ at 10 mTorr and 20 mTorr Ar. The evolution of $(10\bar{1}0)$ and $(10\bar{1}1)$ peaks in the x-ray powder scans indicated that these planes were grown in the film plane. In the x-ray powder scan, the planes parallel to the film surface contribute to the diffraction peak. Figure 7.13 shows a schematic diagram of the (0002), $(10\bar{1}0)$ and $(10\bar{1}1)$ crystallographic planes of *hcp* structure. It indicates that when a (0002) plane is in the film plane, the c-axis lies along the film normal. However, when $(10\bar{1}0)$ and $(10\bar{1}1)$ planes are in the film plane, the c-axis lies in the film plane and close to the film plane (at 29º from the film plane), respectively. This indicated that the in-plane easy axis of magnetization of the $Co_{72}Pt_{28}$ film was attributed to the

emergence of $(10\bar{1}0)$ and $(10\bar{1}1)$ planes in the film plane. This analysis suggested that the Ru deposition pressure largely influenced the evolution of crystallographic structure and magnetic properties of $Co_{72}Pt_{28}$ films.

7.2.3 Effects of Ru top layer thickness in dual-layer structure of Ru underlayer

Figure 7.14 shows layers structure with Ru dual-layer underlayer. The Ru_b (20 nm) and Ru_t (10 nm) layers were deposited at 0.5 mTorr and 10 mTorr Ar, respectively. The thickness and deposition parameters of other layers were kept the same as described in section 3.1.

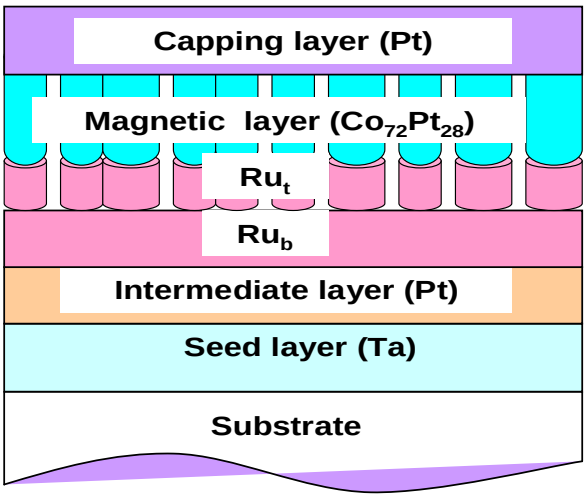

Figure 7.14: Schematic diagram of layers structure with dual-layer Ru underlayer.

7.2.3.1 Crystallographic structure

X-ray powder scans of Ru_t(x nm)(x = 0, 5, 10, 15 and 20) /Ru_b(20 nm)/Pt(2 nm)/Ta(5 nm)/glass are shown in Fig. 7.15. It showed that with increasing the Ru_t layer thickness, the intensity of Ru (0002) peak slightly increased up to 10 nm and decreased with further increasing above 10 nm. The variation of $\Delta\theta_{50}$ with Ru_t thickness, deduced from the rocking curve, is shown in the inset of Fig. 7.15. It showed that $\Delta\theta_{50}$ monotonically increased with increasing Ru_t thickness indicating increased mosaic distribution. The deterioration in intensity with increasing the Ru_t layer thickness was attributed to increased mosaic distribution.[121] This demonstrated that increasing Ru_t thickness did not contribute significantly to improve its crystallinity but noticeably deteriorated mosaic distribution. Figure 7.16 shows the x-ray powder scans of Pt(2 nm)/$Co_{72}Pt_{28}$(20 nm)/Ru_t(x nm)(x = 0, 5, 10, 15 and 20 nm) /Ru_b(20 nm)/Pt(2 nm)/Ta(5 nm)/glass. It also showed that combined Ru (0002) and $Co_{72}Pt_{28}$ (0002) peaks exhibited similar behavior as observed in Fig. 7.15.

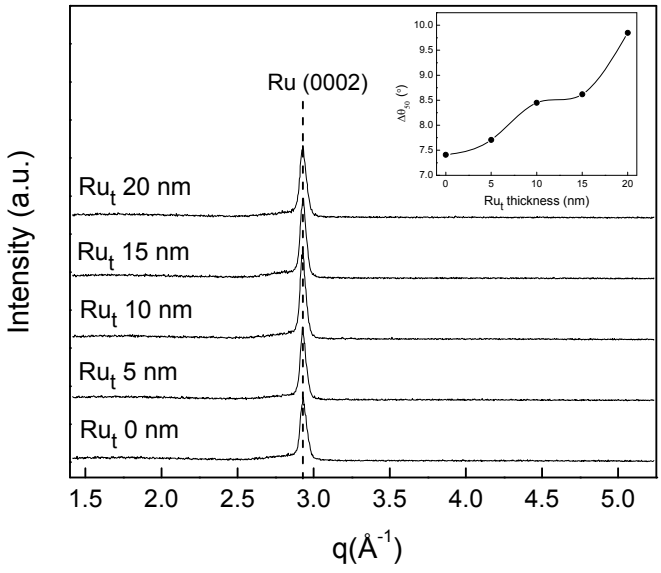

Figure 7.15: X-ray powder scans of Ru_t(x nm) (x = 0, 5, 10, 15 and)/Ru_b(20 nm)/Pt(2 nm)/Ta(5 nm)/glass. Inset shows $\Delta\theta_{50}$ with increasing Ru_t thickness.

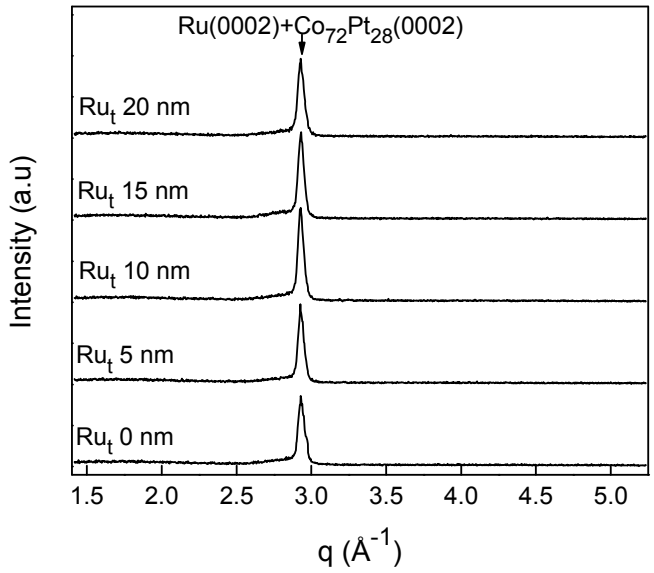

Figure 7.16: X-ray powder scans of Pt(2 nm)/$Co_{72}Pt_{28}$(20 nm)/Ru_t(x nm) (x = 0, 5, 10, 15 and 20)/Ru_b(20 nm)/Pt(2 nm)/Ta(5 nm)/glass.

7.2.3.2 Microstructure

Figures 7.17(a), 7.17(c) and 7.17(e) show the bright field plane-view TEM images, and Figs. 7.17(b), 7.17(d) and 7.17(f) bright field cross-section TEM images for $Co_{72}Pt_{28}$ film deposited on 5 nm, 10 nm and 20 nm Ru_t thickness, respectively. The average columnar width of $Co_{72}Pt_{28}$ for Ru_t thickness of 5 nm, 10 nm and 20 nm, were 7.9±1.2 nm, 7.0±1.1nm and 11.8±1.7 nm, respectively, as determined from the plane-view TEM images. It indicated that grain size initially decreased with increasing the Ru_t thickness, and increased above certain critical thickness. A comparative study of plane-view TEM images illustrated that a maximum voided area (bright contrast) was observed for Fig. 7.17(c) indicating that the grain isolation was least for the $Co_{72}Pt_{28}$ film deposited on 10 nm Ru_t thickness as compared to the film on 5 nm and 20 nm Ru_t thickness.

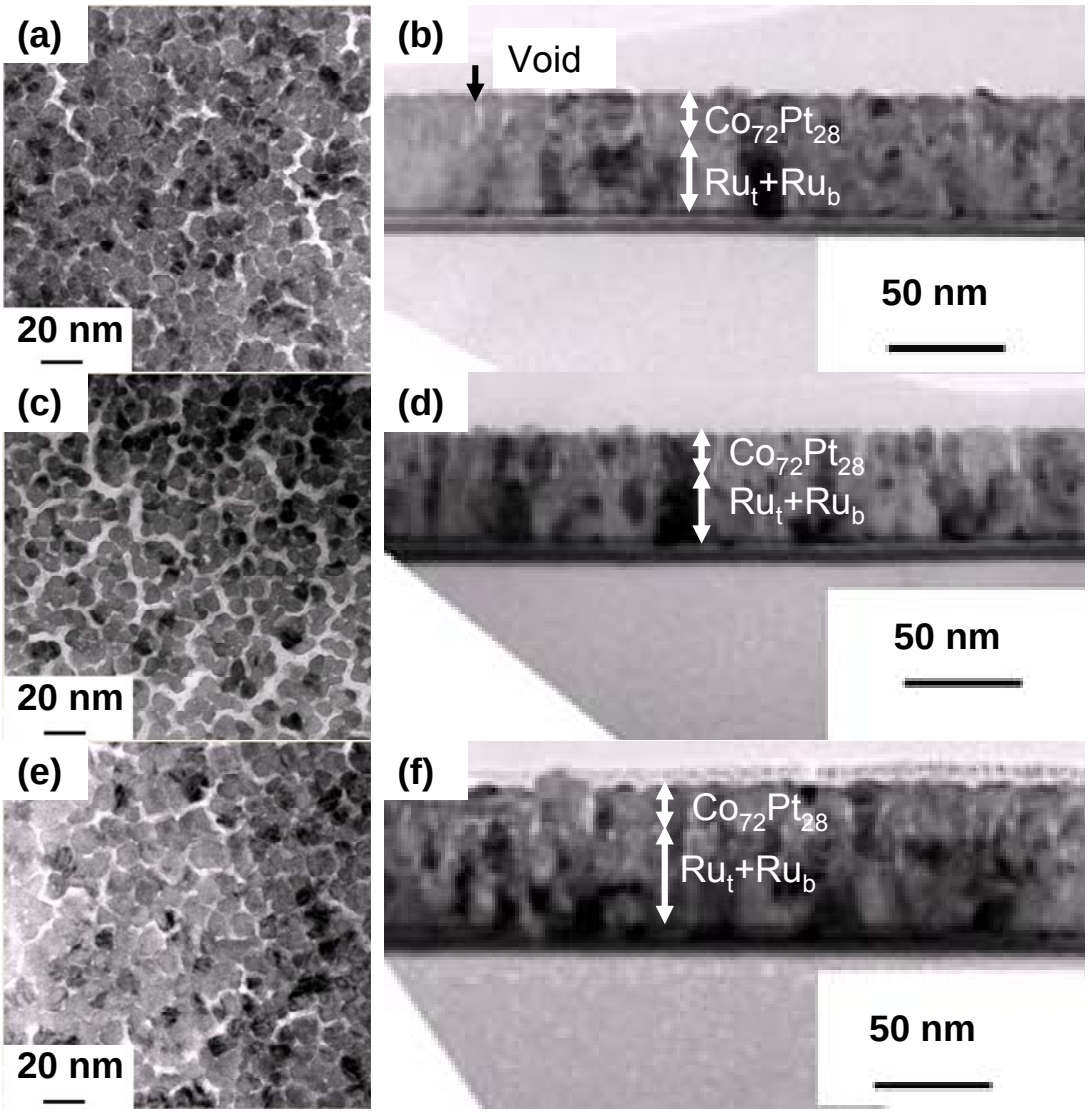

Figure 7.17: Plane-view [(a), (c) and (e)] and cross-section [(b), (d) and (f)] bright field TEM images of $Co_{72}Pt_{28}$ (20 nm) deposited on dual-layer Ru for Ru_t layer thickness 5 nm, 10 nm and 20 nm, respectively.

Similar behavior was also observed from cross-section images. The grain size of film deposited at 20 nm Ru_t was larger than that deposited at 5 nm and 10 nm Ru_t. Figure 7.17(f) showed that the column width of $Co_{72}Pt_{28}$ increased with increasing thickness and acquired inverted frustum shape resulting in decreased grain isolation. The increased column width in the upper part could be attributed to a large grain size as appeared in the plane-view TEM image in Fig. 7.17(e). The evolution of such type of

microstructure can be understood on the basis of energy minimization. The x-ray powder scans results in Fig. 7.16 indicated that $Co_{72}Pt_{28}$ (0002) hetero-epitaxially grown on the Ru (0002), indicating (0002) plane lied in the film plane. Since, (0002) plane in the *hcp* $Co_{72}Pt_{28}$ film corresponds to a lowest surface energy plane. As a result, with increasing thickness, $Co_{72}Pt_{28}$ column diameter could increase in order to increase the surface area of (0002) plane to minimize the surface energy resulting in decreased grain isolation in the later stage of film growth. This phenomenon was discussed in detail in section 5.2.2.

7.2.3.3 Magnetic properties

Figures 7.18(a)-7.18(d) show the in-plane and out-of-plane hysteresis loops for $Co_{72}Pt_{28}$, film deposited on dual-layer Ru underlayer for Ru_t thickness of 5 nm, 10 nm, 15 nm and 20 nm, respectively. Figure 7.19 shows the variation of $H_{c//}$, $H_{c\perp}$ and shearing parameter (α) as a function of Ru_t thickness, which were deduced from hysteresis loops. It showed that increasing the Ru_t thickness from 5 nm to 20 nm, $H_{c//}$ and $H_{c\perp}$ increased monotonically from 0.6 kOe to 1.8 kOe and 5 kOe to 7.2 kOe, respectively. The out-of-plane squareness remained close to unity in all samples. The shearing parameter decreased significantly with increasing Ru_t thickness to 15 nm indicating reduced intergranular magnetic interaction. However, with further increasing the Ru_t layer thickness to 20 nm, shearing parameter slightly increased resulting in increased intergranular magnetic interaction.

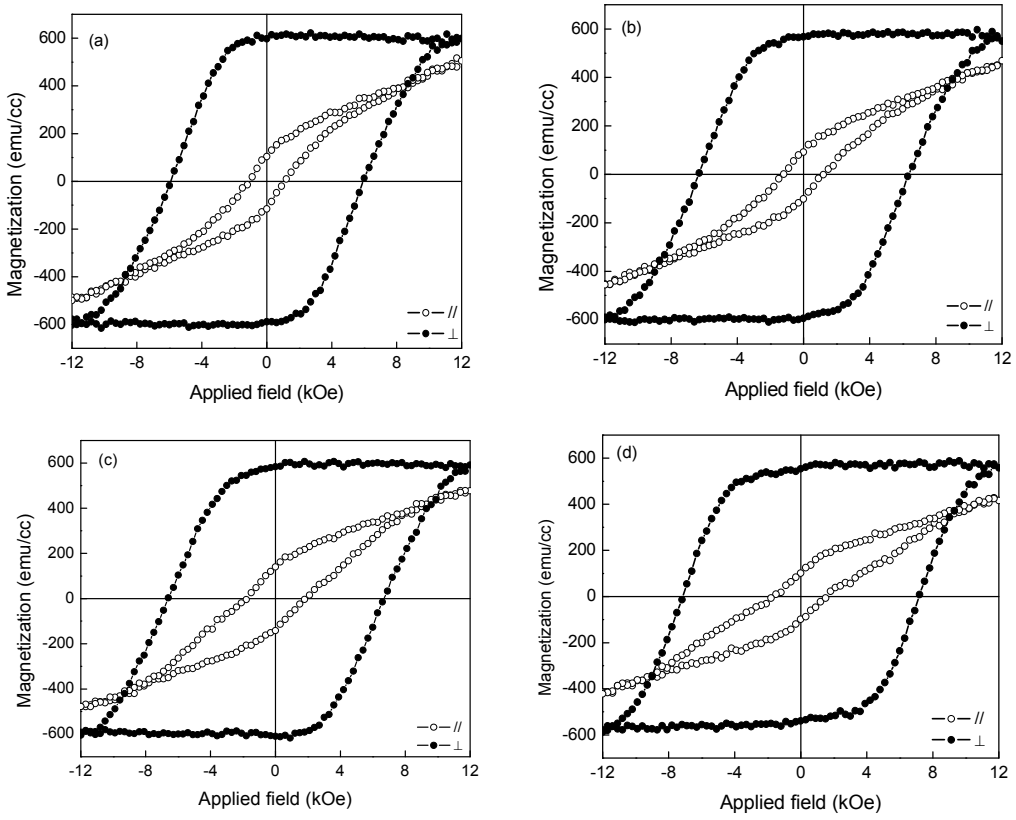

Figure 7.18: In-plane and out-of-plane hysteresis loops of Pt(2 nm)/$Co_{72}Pt_{28}$(20 nm)/Ru_t(x-nm)/Ru_b(20 nm)/Pt(2 nm)/Ta(5 nm)/glass, where x = (a) 5 nm, (b) 10 nm, (c) 15 nm and (d) 20 nm.

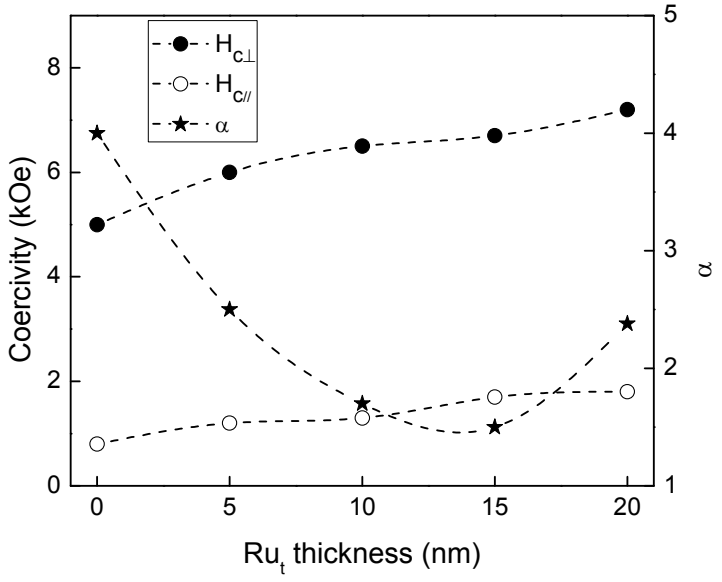

Figure 7.19: Variation of in-plane coercivity and out-of-plane coercivity, and shearing parameter (α) with Ru_t thickness in Pt(2 nm)/$Co_{72}Pt_{28}$(20 nm)/Ru_t(x-nm)/Ru_b(20 nm)/Pt(2 nm)/Ta(5 nm)/glass, where $0 \leq x \leq 20$.

Increased shearing parameter for 20 nm Ru_t was consistent with a reduced grain isolation as observed from the plane-view and cross-section TEM images in Fig. 7.17(e) and 7.17(f), respectively. Despite the reduced crystallinity and increased mosaic distribution with increasing Ru_t thickness as observed from the XRD, $H_{c\perp}$ and $H_{c//}$ increased. In order to explain increased coercivity with Ru_t thickness, a correlation between coercivity and intergranular exchange interaction was made. It indicated that increased coercivity was attributed to reduced intergranular magnetic interaction up to 15 nm Ru_t thickness. However, coercivity increased at 20 nm Ru_t thickness despite the increased intergranular exchange interaction. It is well known that coercivity is an extrinsic property that depends on intergranular exchange interaction, different magnetization reversal mechanism and magnetocrystalline anisotropy of material. In order to investigate the magnetization reversal mechanism, initial magnetization curves of all samples were measured. All samples were AC demagnetized before measurement. Figure 7.20 shows the normalized initial magnetization curves. The field axis was normalized with respective coercivity to exclude the effects of magnetocrystalline anisotropy. It showed that the shape of initial magnetization curves of all samples were convex towards the field axis. In all curves, the increase in magnetization with magnetic field was initially slow and increased abruptly above critical field, indicating that magnetization was reversed by coherent rotation. In order to further investigate the cause of increased coercivity for 20 nm Ru_t, magnetic anisotropy for different samples were measured from the difference in area between the in-plane and out-of-plane hysteresis loops as discussed in section 2.3.3.2. It was observed that magnetic anisotropy marginally increased by 11% with increasing the Ru_t layer thickness from 5 to 20 nm. This indicated that

increased coercivity could be attributed to a increased magnetic anisotropy for 20 nm Ru_t thickness.

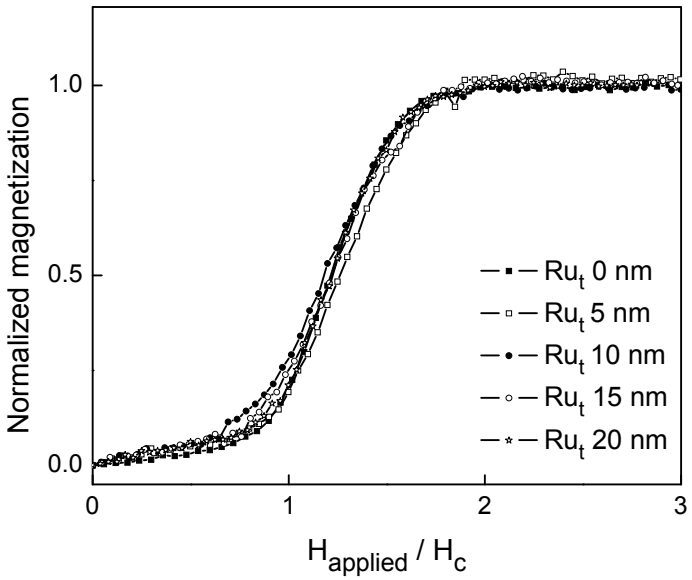

Figure 7.20: Initial magnetization curve of Pt(2 nm)/$Co_{72}Pt_{28}$(20 nm)/Ru_t(x-nm)/Ru_b(20 nm)/Pt(2 nm)/Ta(5 nm)/glass, where $0 \leq x \leq 20$.

Table 7.1: Qualitative comparison of microstructure and magnetic properties of three samples of $Co_{72}Pt_{28}$, where 30 nm Ru was deposited at 0.5 mTorr (single layer, low pressure), 10 mTorr (single layer, high pressure) and Ru_t(10 nm at 10 mTorr)/Ru_b(20 nm at 0.5 mTorr) (dual-layer).

Properties	Single layer (Low pressure)	Single layer (High pressure)	Dual-layer
FWHM	Small	Large	Medium
Texture	(0002)	No texture	(0002)
Grain size	Medium	Large	Small
Magnetic interaction	Medium	Large	Small
Easy axis	Out-of-plane	In-plane	Out-of-plane

7.3 Summary

The effects of Ru underlayer on microstructure and magnetic properties of $Co_{72}Pt_{28}$ film were investigated. Both the microstructure and magnetic properties of $Co_{72}Pt_{28}$ film depended on the Ru thickness. It was observed that the grain size, crystallographic texture and easy axis of $Co_{72}Pt_{28}$ films deposited on Ru underlayer could be controlled by deposition pressure of Ru underlayer. A comparative study of microstructure and magnetic properties of $Co_{72}Pt_{28}$ film deposited on single layer (deposited at low and high Ar pressure) and dual-layer Ru underlayer were summarized in Table 1. A single Ru layer deposited at high Ar pressure was not effective for perpendicular magnetic recording, since it destroyed the (0002) texture of the Ru and $Co_{72}Pt_{28}$, exhibited large mosaic distribution, grain size, intergranular magnetic interaction, and in-plane easy axis of magnetization. A single layer of Ru, deposited at low Ar pressure, had a small mosaic distribution of (0002) reflection compared to the dual-layer structure. Despite large mosaic distribution of Ru dual-layer compared to the Ru single layer deposited at low Ar pressure, the dual-layer structure exhibited some advantage over the single layer, such as small grain size and reduced intergranular magnetic interaction. The coercivity of $Co_{72}Pt_{28}$ increased with increasing the Ru_t thickness due to reduced intergranular exchange interactions and increased magnetic anisotropy.

Chapter 8
Conclusion and Future Work

The primary objective of this thesis was to fabricate the media material with high K_u and small grain size. This chapter had summarized the work presented in this thesis, highlighting the main results. The future works related to this thesis are also discussed in brief.

8.1 Conclusion

In this thesis *hcp* CoPt media was fabricated at room temperature. For $Co_{72}Pt_{28}$ films, they had highest K_u compared to films with different compositions in this study. The $Co_{72}Pt_{28}$ media also showed large coercivity, large nucleation field and high thermal stability factor. In order to study the origin of high K_u in the $Co_{72}Pt_{28}$ film, the phase miscibility, growth induced structural anisotropy and strain was investigated in the CoPt films by polarized EXAFS. It was observed that Pt showed complete miscibility with Co and occupied the Co position in the Co lattice. No evidence of compositional heterogeneities in the in-plane and out-of-plane directions was detected for $Co_{72}Pt_{28}$. However, direct evidence of structural heterogeneities was observed for $Co_{90}Pt_{10}$ and $Co_{57}Pt_{43}$ films. For such compositions, Co was surrounded by more Pt in the film plane compared to the film normal direction. The average interatomic distance in the in-plane polarization geometry was larger than that of the out-of-plane polarization geometry for $Co_{90}Pt_{10}$ and $Co_{57}Pt_{43}$, however, such distances were approximately the same for $Co_{72}Pt_{28}$. As a result, in-plane tensile strain induced in the $Co_{90}Pt_{10}$ and $Co_{57}Pt_{43}$ films. An absence of in-plane tensile strain was observed for

$Co_{72}Pt_{28}$, which favored the growth of *hcp* stacking. The large magnetic anisotropy in the $Co_{72}Pt_{28}$ film could be attributed to the improved *hcp* stacking.

In order to achieve a large SNR and perpendicular magnetic anisotropy in the $Co_{72}Pt_{28}$ film, layer engineering approach was used. Increasing $Co_{72}Pt_{28}$ film thickness changed the magnetization reversal mechanism from the domain wall motion at small thickness to the S-W model at intermediate thickness, due to reduced intergranular exchange interaction. With further increasing the $Co_{72}Pt_{28}$ film thickness, magnetization reversal again started to deviate away from the S-W model due to increased intergranualar exchange interaction. It was found that the smoother surface of Ta seedlayer improved the crystallinity and the c-axis dispersion of Ru/CoPt layers resulting in enhanced magnetic anisotropy to ~9 x 10^6 ergs/cc. Such a high value of magnetic anisotropy could help increase the areal density to 1 Tbit/in^2 using $Co_{72}Pt_{28}$ media, above the theoretical limit of current CoCrPt perpendicular recording media. It was also observed that small Ar pressure favored (0002) texture with a narrow c-axis distribution for Ru underlayer, which promoted the development of (0002) texture of $Co_{72}Pt_{28}$ film. The film had the magnetic easy axis along the film normal direction. However, increasing Ar pressure perturbed the Ru (0002) texture and changed the easy axis of magnetization from the out-of-plane to in-plane direction, which was undesirable for perpendicular magnetic recording. The dual-layer structure of the Ru underlayer, where the bottom layer Ru was deposited at low Ar pressure and top layer Ru at high Ar pressure, was considered as an effective way to reduce the grain size and intergranular exchange interaction to achieve favorable environment for large *SNR*.

8.2 Future Work

In this study, the magnetocrystalline anisotropy up to ~9 x 10^6 erg/cc was achieved, which was sufficient to reduce the thermally stable grain size down to 4.5 nm, and able to increase the areal density up to 1 Tbit/in^2. However, in this study the minimum grain size in recording layer was achieved down to 7.0 nm, which was deposited on dual-layer Ru underlayer. This indicates that there is still sufficient space to further reduce the grain size of $Co_{72}Pt_{28}$ film either by adding nonmagnetic materials in recording layer or controlling the microstructure of under layer. This high anisotropy media is also useful to investigate the switching behavior of ECC media.

Bibliography

1. Magnetic Recording: The First 100 Years, edited by Eric D. Daniel, C. Denis Mee and Mark H. Clark, IEEE Press New Yark (1999).
2. A. Moser, K. Takano, D. T. Margulies, M. Albrecht, Y. Sonobe, Y. Ikeda, S. Sun and E. E. Fullerton, J. Phys. D: Appl. Phys. **35**, R157 (2002).
3. H. Coufal, L. Dhar and C. D. Mee, MRS Bulletin **31**, 374 (2006).
4. R. Dittrich, G. Hu, T. Schrefl, T. Thomson, D. Suess, B. D. Terris and J. Fidler, J. Appl. Phys. **97**, 10J705 (2005).
5. Introduction to magnetic Materials by B. D. Cullity, 2nd edition, Addison-Wesley Publishing Company (1972).
6. S. H. Charp, P. L. Lu and Y. He, IEEE Trans. Magn. **33**, 978 (1997).
7. A. Moser, K. Takano, D. T. Margulies, M. Albrecht, Y. Sonobe, Y. Ikeda, S. H. Sun and E. E. Fullerton, J. Phys. D: Appl. Phys. **35**, R(157) (2002).
8. K. E. Johnson, J. Appl. Phys. **87**, 5365 (2000).
9. L. L. Lee, D. E. Laughlin and D. N. Lambeth, IEEE Trans. Magn. **34**, 1561 (1998).
10. S. Yoshimura, D. D. Djayaprawira, M. Mikami, Y. Takakuwa and M. Takahashi, IEEE Trans. Magn. **38**, 1958 (2002).
11. Y. Xu, J. P. Wang, Z. S. Shan, H. Jiang and C. T. Chong, J. Appl. Phys**. 88**, 7234 (2000).
12. Y. Hsu, J. M. Sivertsen and J. H. Judy, IEEE Trans. Magn. **26**, 1599 (1990).
13. I. R. McFaden, E. E. Fullerton and M. J. Care, MRS Bulletin **31**, 379 (2006).
14. Magnetic Storage systems beyond 2000, edited by George C. Hadjipanayis, Kluwer Academic Publishers, The Neatherlands (2001).
15. S. Iwasaki and K. Takemura, IEEE Trans. Magn. **11**, 1173 (1975).

16. R. Wood, Y. Sonobe, Zhen Jin and B. Wilson, J. Magn. Magn. Mater. **235,** 1 (2001).

17. Advanced Magnetic Nanostructure, edited by D. Sellmyer and R. Skomski, Springer NY (2006).

18. K. Ouchi, IEICE Trans. Electron. **E84-C**, 1121 (2001).

19. Y. Kubota, D. Weller, M. L. Wu, X. Wu, G. Ju, D. Karns and J. Yu, J. Magn. Magn. Mater. **242-245**, 297 (2002)

20. K. Ouchi and S. Iwasaki, IEEE Trans. Magn. **23**, 2443 (1987).

21. X. W. Wu, H. Zhou, R. J. M. van de Veerdonk, G. Ju, B. Lu and D. Weller, Appl. Phys. Lett. **81**, 2409 (2002).

22. J. Ariake, N. Honda, K. Ouchi, and S. Iwasaki IEEE Trans. Magn. **36**, 2411 (2000).

23. D. E. Laughlin, S. Kumar, Y. Peng and A. G. Roy, IEEE Trans. Magn. **41**, 719 (2005).

24. T. Shimatsu, H. Uwazumi, H. Muraoka and Y. Nakamura, IEEE Trans. Magn. **38**, 1973 (2002).

25. J. Ariake, T. Chiba and N. Honda, IEEE Trans. Magn. **41**, 3142 (2005).

26. R. Sbiaa and S. N. Piramanayagam, Recent Patents on Nanotechnology **1**, 29 (2007).

27. W. Peng, R. H. Victora and J. H. Judy, IEEE Trans. Magn. **37**, 1577 (2001).

28. W. B. Zeper, F. J. A. M. Greidanus and P.F. Carcia, IEEE Trans. Magn. **25**, 3764 (1989).

29. P. F. Carcia, A.D. Meinhalt, and A. Suna, Appl. Phys. Lett. **47**, 178 (1985).

30. F. J. den Broeder, H. C. Donkersloot, H. J. G. Draaisma, and W. J. M. de Jonge, J. Appl. Phys. **61**, 4317 (1987).

31. K. Barmak, J. Kim, L. H. Lewis, K. R. Koffey, M. F. Toney, A. J. Kellock and J. U. Thiele, J. Appl. Phys. **98**, 33904 (2005).

32. Y. Z. Zhou, J. S. Chen, G. M. Chow and J. P. Wang, J. Appl. Phys. **95**, 7495 (2004).

33. J. S. Chen, B.C. Lim, J. F. Hu, Y. K. Lim, B. Liu and G. M. Chow, Appl. Phys. Lett. **90**, 42508 (2007).

34. H. J. Richer and S. D. Harkness IV, MRS Bulletin **31**, 384 (2006).

35. T. Shima, K. Takanashi, Y. K. Takahashi and K. Hono, Appl. Phys. Lett. **85**, 2571 (2004).

36. J. J. M. Ruigrok, R. Coehoorn, S. R. Cumpson and H. W. Kesteren, J. Appl. Phys**. 87,** 5398 (2000).

37. M. Alex, A. Tselikov, T. McDaniel, N. Deeman, T. Valet and D. Chen, IEEE Trans. Magn. **37**, 1244 (2001).

38. S. Y. Chou, M. Wei, P. R. Krauss and P. B. Fischer, J. Appl. Phys. **76**, 6673 (1994).

39. S. Y. Chou, P. R. Krauss and P. J. Renstrom, J. Vac. Sci. Technol. B **14**, 4129 (1996).

40. C. A. Ross, Annu. Rev. Mater. Res. **31**, 203 (2001).

41. B. D. Terris and T. Thomson, J. Phys. D: Appl. Phys. **38**, R199 (2005).

42. D. N. Lambeth, E. M. T. Velu, G. H. Bellesis, L. L. Lee and D. E. Laughlin, J. Appl. Phys. **79**, 4496 (1996).

43. R. H. Victora and X. Shen, IEEE Trans. Magn. **41**, 537 (2005).

44. J. U Theile, S. Maat, J. L. Robertson and E. E. Fullerton, IEEE Trans. Magn. **40**, 2537 (2004).

45. M. Alex, A. Tselikov, T. McDaniel, N. Deeman, T. Valet and D. Chen, IEEE

Tarns. Magn. **37**, 1244 (2001).

46. S. Sun, C. B. Murry, D. Weller, L. Folk and A. Moser, Science **287**, 1989 (2000).

47. H. J. Richer, IEEE Trans. Magn. **29**, 2258 (1993).

48. J. P. Wang, W. Shen and J. Bai, IEEE Trans, Magn. **41**, 3181 (2005).

49. J. P. Wang, W. K. Shen, J. M. Bai, R. H. Victora, J. H. Judy and W. L. Song, Appl. Phys. Lett. **86**, 142504 (2005).

50. M. Kapoor, X. Sen and R. H. Victora, J. Appl. Phys. **99**, 8Q902 (2006).

51. T. Oikawa, M. Nakamura, H. Uwazumi, T. Shimatsu, H. Muraoka and Y. Nakamura, IEEE Trans. Magn. **38**, 1976 (2002).

52. M. Zheng, B. R. Acharya, G. Choe, J. N. Zhou, Z. D. Yang, E. N. Abarra and K. E. Johnson, IEEE Trans. Magn. **40**, 2498 (2004).

53. H. Uwazumi, K. Enomoto, Y. Sakai, S. Takenoiri, T. Oikawa and S. Watanabe, IEEE Trans. Magn. **39**, 1914 (2003).

54. H. S. Jung, U. Kwon, M. Kuo, E. M. T. Velu, S. S. Malhotra, W. Jiang and G. Bertero, IEEE Trans. Magn. **43**, 615 (2007).

55. T. Chen, G. B. Charlan and T. Yamashita, J. Appl. Phys. **57**, 5103 (1983).

56. T. Shimatsu, H. Sato, T. Oikawa, Y. Inaba, O. Kitakami, S. Okamoto, H. Aoi, H. Muraoka and Y. Nakamura, IEEE Trans. Magn. **41**, 566 (2005).

57. T. Shimatsu, H. Uwazumi, Y. Sakai, A. Otsuki, I. Watanabe, H. Muraoka, and N. Nakamura, IEEE Trans. Magn. **37**, 1567 (2001).

58. H. Sato, T. Shimatsu, Y. Kitakami, S. Okamoto, H. Aoi, Muraoka and Y. Nakamura, IEEE Trans. Magn. **43**, 2106 (2007).

59. B. Liu, D. Weller, A. Sunder, G. Ju, X. Wu, R. Brockie, T. Nolan, C. Brucker and R. Ranjan, J. Appl. Phys. **93**, 6751 (2003).

60. Y. Inaba, T. Shimatsu, T. Oikawa, H. Sato, H. Aoi, H. Muraoka and Y. Nakamura, IEEE Trans. Magn. **40**, 2486 (2004).

61. M. Zheng, B. R. Acharya, G. Choe, J. N. Zhou, Z. D. Yang, E. N. Abarra and K. E. Johnson, IEEE Trans. Magn. **40**, 2498 (2004).

62. E. Girt, S. Wu, B. Lu, G. Ju, T. Nolan, S. Harkness, B. Valcu, A. Dobin, J. D. Risner, M. Munteanu, R. Thangaraj, C. H. Chang, T. Tran, X. Wu, O. Mryasov, D. Weller, and S. Hwang, J. Appl. Phys. **99**, 8E715 (2006).

63. S. H. Park, S. O. Kim, T. D. Lee, H. S. Oh, Y. S. Kim, N. Y. Park and D. H. Hong, J. Appl. Phys. **99**, 8E701 (2006).

64. J. Z. Shi, S. N. Piramanayagam, C. H. Mah, H. B. Zhao, J. M. Zhao, Y. S. Kay and C. K. Pock, Appl. Phys. Lett. **87**, 222503 (2005).

65. S. N. Piramanayagam and K. Srinivasan, Appl. Phys. Lett. **91**, 142508 (2007).

66. J. A. Thornton, J. Vac. Sci. Technol. A **4**, 3059 (1986).

67. G. M. Chow, C. J. Sun, E. W. Soo, J. P. Wang, H. H. Lee, D. Y. Noh, T. S. Cho, J. H. Je and Y. K. Hwu, Appl. Phys. Lett. **80**, 1607 (2002).

68. G. M. Chow, W. C. Goh, Y. K. Hwu, T. S. Cho, J. H. Je, H. H. Lee, H. C. Kang, D. Y. Noh, C. K. Lin and W. D. Chang, Appl. Phys. Lett. **75**, 2503 (1999).

69. Neutron and X-ray Spectroscopy, edited by F. Hippert, E. Geissler, J. L. Hodeau, E. L. Berna and J. R. Regnard, Springer, The Netherland (2006).

70. Application of synchrotron radiation to materials analysis, edited by H. Saisho and Y. Gohashi, Elsevier, Amsterdam (1996).

71. X-Ray Absorption, Principle, Applications, Technique of EXAFS, SEXAFS and XANES, edited by D. C. Koningsberger and R. Prins, John Wiley & Sons (1988).

72. P. A. Lee, P. H. Citrin, P. Eisenberger and B. M. Kincaid, Rev. Mod. Phys. **53**, 769 (1981).

73. J. J. Rehr and R. C. Albers, Rev. Mod. Phys. **72**, 621 (2000).

74. V. G. Harris, K. D. Aylesworth, B. N. Das, W. T. Elam and N. C. Koon, Phys. Rev. Lett. **69**, 1939 (1992).

75. J. O. Cross, M. Newville, F. Hellman, P. W. Rooney, A. L. Shapiro and V. G. Harris, J. Synchrotron Rad. **8**, 880 (2001).

76. T. A. Tyson, S. D. Conradson, R. F. C. Farrow and B. A. Jones, Phys. Rev. B **54**, R3702 (1996).

77. C. Meneghini, M. Maret, V. Parasote, M. C. Cadeville, J. L. Hazemenn, R. Cortes, and S. Colonna, Eur. Phy. J. B **7**, 347 (1999).

78. M. Jaouen, J. Pacaud and C. Jaouen, Phys. Rev. B **64**, 144106 (2001).

79. Thin Film Phenomena by K. L. Chopra, McGraw-Hill book Company (1969).

80. Thin Film deposition by Donald L. Smith, McGraw-Hill book Company (2001).

81. Principle of Physical Vapor Deposition of Thin Films by K. S. Sree Harsha, ELSEVIER Ltd (2006).

82. Encyclopedia of Materials Characterization: Surfaces, Interfaces, Thin Films, edited by C. R. Brundle, C. A. Evans Jr. and S. Wilson, Butterworth-Heinemann Stoneham MA (1992).

83. Principles and Applications of High Energy Ion Microbeams, edited by F. Watt and G. W. Grime, Adom Hilger Bristol (1987).

84. Physics of Ferromagnetism by S. Chikazumi, Oxford University Press (1996).

85. Modern Magnetic Materials-Principles and Applications by R. C. O'Handley, John Wiley & Sons, Inc. (1999).

86. M. P. Sharrock, J. Appl. Phys. **76**, 6413 (1994).

87. J. Burd, M. Huq and E. W. Lee, J. Magn. Magn. Mater. **5**, 135 (1977).

88. J. Worst, J. C. Lodder and T. Weilinga, Thin Solid Films **101**, 75 (1983)

89. P. Grutter, D. Rugar and H.J. Mamin, Ultramicroscopy **47**, 393 (1992).

90. Scanning Force Microscopy with Application to Electric Magnetic and Atomic Forces by D. Sarid, Oxford University Press (1994).

91. Elements of X-ray Diffraction by B. D. Cullity and S. R. Stock, Prentice–Hall Inc. (2001).

92. X-Ray Diffraction by B. E. Warren, Addison-Wesley Publishing Company (1969).

93. A textbook of Materials science by D. B. Williams and C. B. Carter, Springer (2004).

94. G. Binnig and H. Rohrer, IBM J. Res. Dev. **30**, 279 (2000).

95. K. K. Mani Pandey, J. S. Chen and G. M. Chow, J. Appl. Phys. **100**, 54909 (2006).

96. B. Lu, J. Zou, D. N. Lambeth and D. E. Laughlin, IEEE Trans. Magn. **36**, 2357 (2000).

97. Binary Alloy Phase Diagrams, 2nd ed., edited by T. B. Massalski, Vol. 2, p. 1226 ASM International, Materials Park, OH, (1990).

98. G. R. Harp, D. Weller, T. A. Rabedeau, R. F. C. Farrow and M.F. Toney, Phys. Rev. Lett. **71**, 2493 (1993).

99. P. W. Rooney, A. L. Shapiro, M. Q. Tran and F. Hellman, Phys. Rev. Lett. **75**, 1843 (1995).

100. T. Shimatsu, Y. Okazaki, H. Sato, O. Kitakami, S. Okamoto, H. Aoi, H. Muraoka and Y. Nakamura, IEEE Trans. Magn. **43**, 2995 (2007).

101. E. A. Stern, M. Newville, B. Ravel, Y. Yacoby and D. Haskel, Physica B **209**, 117

(1995).

102. J. J. Rehr, R. C. Albers and S. I. Zabinsky, Phys. Rev. Lett. **69**, 3397 (1992).

103. M. S. Nashner, A. I. Frenkel, D. Somerville, C. W. Hills, J. R. Shapley and R. G. Nuzzo, J. Am. Chem. Soc. **120**, 8093 (1998).

104. N. Marsot, R. Belkhou, H. Magnan, P. L. Fevre, C. Guillot and D. Chandesris, Phys. Rev. B **59**, 3135 (1999).

105. Introduction to the Theory of Ferromagnetism by A. Aharoni, Oxford University Press (2000).

106. H. S. Jung, M. Kuo, S. S. Malhotra and G. Bertero, Appl. Phys. Lett. **91**, 212502 (2007).

107. X. W. Wu, R. J. M. van de Veerdonk, B. Lu and D. Weller, J. Magn. Magn. Mater. **303**, e261 (2006).

108. S. Saito, D. Hasegawa, F. Hoshi, D. D. Djayaprawira and M. Takahasi, Appl. Phys. Lett. **80**, 811 (2002).

109. T. D. Lee, M. S. Hwang and K. J. Lee, J. Magn. Magn. Mater, **235**, 297 (2001).

110. C. J. Sun, G. M. Chow, J. P. Wang, E. W. Soo and J. H. Je, J. Appl. Phys. **93**, 8725 (2003).

111. T. Onoue, T. Asahi, K. Kuramochi, J. Kawaji, T. Osaka, J. Ariake, K. Ouchi, G. Safran and N. Yaguchi, J. Appl. Phys. **92**, 4545 (2002).

112. W. K. Sen, A. Das, M. Racine, R. Cheng, J. Judy and J. P. Wang, IEEE Trans. Magn. **42**, 2381 (2006).

113. S. Yoshimura, D. D. Djayaprawira, M. Mikami, Y. Takakuwa and M. Takahashi, IEEE Trans. Magn. **38**, 1958 (2002).

114. J. Kanak, M. Czapkiewicz, T. Stobiecki, M. Kachel, I. Sveklo, A. Maziewski and

S. van Dijken, Phys. Stat. Sol. (a), **204**, 3950 (2007).

115. Y. C. Feng, D. E. Laughlin and D. N. Lambeth, J. Appl. Phys. **76**, 7311 (1994).

116. R. Mukai, T. Uzumaki and A. Tanaka, J. Appl. Phys. **97**, 10N119 (2005).

117. H. Sato, T. Shimatsu, Y. Okazaki, O. Kitakami, S. Okamoto, H. Aoi, H. Uraoka and Y. Nakamura, IEEE Trans. Magn. **43**, 2106 (2007).

118. S. N. Piramanayagam, H. B. Zhao, J. H. Shi and C. H. Mah, Appl. Phys. Lett. **88**, 92506 (2006).

119. S. Oikawa, A. Takeo, T. Hikosaka and Y. Tanaka, IEEE Trans. Magn. **36**, 2393 (2000).

120. J. W. Park, Y. K. Kim, T. H. Lee, H. S. Oh and B. K. Lee, Phys. Status Solidi A **201,** 1763 (2004).

121 A. G. Roy and D. E. Laughlin, J. Appl. Phys. **91**, 8076 (2002).

Appendix A

The schematic of *hcp* structure is shown as follows.

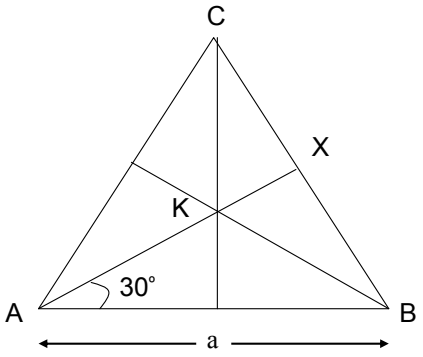

Figure: A1

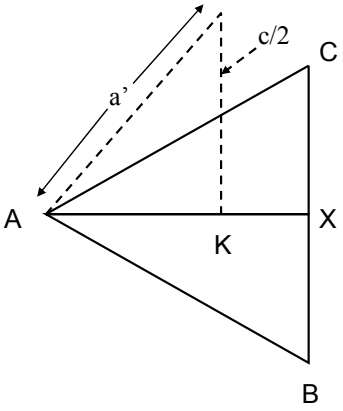

Figure: A2

From Fig. A1,

$$\frac{AX}{AB} = \frac{AX}{a} = \cos 30^0$$

$$AX = a\cos 30^0 = a\left[\frac{\sqrt{3}}{2}\right]$$

$$AK = \frac{2}{3}a\left[\frac{\sqrt{3}}{2}\right] = \frac{a}{\sqrt{3}}$$

From Fig A2,

$$\frac{c}{2} = \sqrt{(a')^2 - (AK)^2}$$

$$\frac{c}{2} = \sqrt{(a')^2 - \left(\frac{a}{\sqrt{3}}\right)^2} \qquad \text{(A.1)}$$

In equation (A.1), *a* is the average interatomic distance measured from the in-plane measurement and *a'* the average interatomic distance measured from the out-of-plane

measurement. The average interatomic distance in the in-plane (a) and out-of-plane (a') measurement was determined from equation

$$a = \left[\left[(R_{Co-Co})(\%N_{Co-Co}) + (R_{Co-Pt})(\%N_{Co-Pt})\right]/100\right]_{in-plane} \quad \text{(A.2)}$$

$$a' = \left[\left[(R_{Co-Co})(\%N_{Co-Co}) + (R_{Co-Pt})(\%N_{Co-Pt})\right]/100\right]_{out-of-plane} \quad \text{(A.3)}$$

Using the parameters given in Table A1, the value of a, a' can be calculated using equations (A.2) and (A.3), respectively. Thereafter using equation (A.1), the value of c can be calculated. The calculated value of a, a', c and c/a has been summarized in Table A2.

Table A1: Fitting results of nearest neighbor's distance and % of coordination number measured at Co-K edge in the in-plane and out-of-plane geometries (based on Table 4.2).

Sample	In-plane				Out-of-plane			
	R_{Co-Co}	$\%N_{Co-Co}$	R_{Co-Pt}	$\%N_{Co-Pt}$	R_{Co-Co}	$\%N_{Co-Co}$	R_{Co-Pt}	$\%N_{Co-Pt}$
$Co_{90}Pt_{10}$	2.532	90.2	2.590	9.8	2.508	93.6	2.579	6.4
$Co_{72}Pt_{28}$	2.556	72.2	2.604	27.8	2.547	73.0	2.607	27.8
$Co_{57}Pt_{43}$	2.598	50.5	2.631	49.5	2.581	59.5	2.631	40.5

Table A2: The calculated value of a, a', c and c/a.

Samples	a	a'	c	c/a
$Co_{90}Pt_{10}$	2.530	2.513	-	-
$Co_{72}Pt_{28}$	2.569	2.563	4.181	1.627
$Co_{57}Pt_{43}$	2.614	2.601	-	-

Note: In Table A2, the c and c/a are not calculated for $Co_{90}Pt_{10}$ and $Co_{57}Pt_{42}$ due to the mixture of the *fcc* and *hcp* phases.